Spectroscopic and Photophysical Properties of the Trioxatriangulenium Carbocation and its Interactions with Supramolecular Systems

Reynisson, Johannes

Publication date:
2000

Document Version
Publisher's PDF, also known as Version of record

Spectroscopic and Photophysical Properties of the Trioxatriangulenium Carbocation and its Interactions with Supramolecular Systems

Jóhannes Reynisson

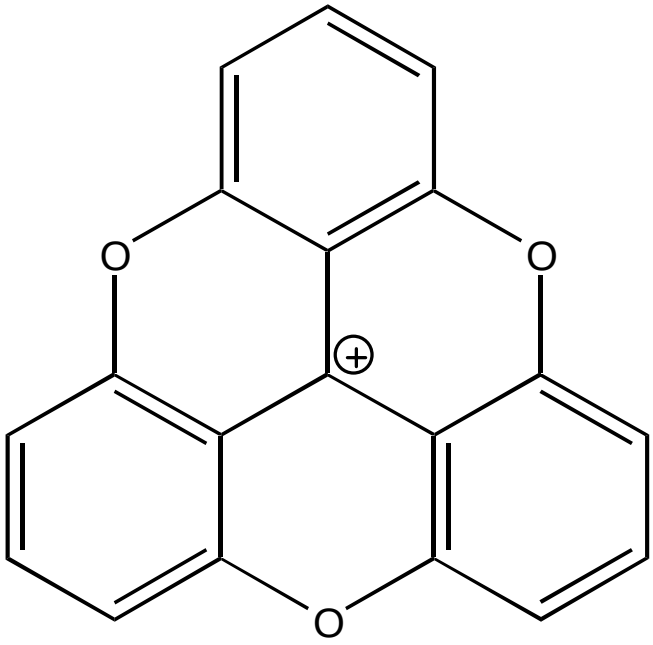

Risø National Laboratory, Roskilde, Denmark
June 2000

Abstract

Trioxatriangulenium ($TOTA^+$, 4,8,12-trioxa-4,8,12,12*c*-tetrahydro-dibenzo[*cd,mn*]-pyrenylium) is a closed shell carbocation which is stable in its crystalline form and in polar solvents at ambient temperatures.

Raman and infrared (IR) spectra of $TOTA^+$ are reported. In a theoretical effort, *ab initio* and density function theory (DFT) methods are used to determine the vibrational spectra and the optimised geometry of $TOTA^+$. The theoretical results are compared with the experimentally obtained vibrational spectra and with the previously reported X-ray crystal structure. It is concluded that DFT calculations based on the nonlocal exchange-correlation functionals (UB-LYP) yield the most accurate description of the vibrational spectra and the geometry of $TOTA^+$. As a result of the calculations it appears that the positive charge in the $TOTA^+$ carbocation is substantially delocalised.

The physical and chemical properties of the excited singlet and triplet states of $TOTA^+$ are investigated. A strong fluorescence is observed at 520 nm, which is readily quenched by 10 aromatics. The quenching rate increases with decreasing oxidation potential of the aromatic molecules signifying a charge transfer mechanism, which falls within the normal region of the Marcus theory. The Stern-Volmer plots derived from steady state quenching measurements all curve upwards indicating partial static quenching due to complex formation between the ground state of $TOTA^+$ and the electron donor. The charge transfer complexes are also observed directly by means of electron absorption spectroscopy. The $TOTA^+$ triplet – triplet absorption and phosphorescence spectra are reported.

The interaction between $TOTA^+$ and the DNA double helix is investigated. The mode of binding is determined as intercalation, i.e. the discus shaped carbocation is wedged between the base pairs. Various techniques are employed in order to determine the binding mode such as viscosity, melting point and circular dichroism experiments. According to the viscosity measurements extraordinary small lengthening of the DNA fragments (1.3 Å) is observed when intercalation takes place. $TOTA^+$ is a photonuclease, the scission taking place at a GG step in the DNA string.

DNO dimers substituted with pyrene as photophysical probes are synthesised. The excimer formation and ground state associations are investigated by means of fluorescence and absorption spectroscopic techniques. A significant difference is observed of the photophysical parameters between the different derivatives, which reflects the structural properties of the DNOs.

Thesis submitted in partial fulfilment of the requirements for the degree of Ph.D.

University of Copenhagen, Department of Chemistry

Condensed Matter Physics and Chemistry Department, Risø National Laboratory

Risø – R-1191 (EN)
ISBN 87 – 550 – 2712 - 1
ISBN 87 – 550 – 2714 – 8 (Internet)
ISSN 0106 - 2840

Preface

The work presented in this thesis was carried out at the Condensed Matter Physics and Chemistry Department, Risø National Laboratory, between May 1997 and June 1999 and at the Georgia Technical Institute, between July 1999 and December 1999.

The work presented here would not have been possible without my supervisor Dr. Robert Wilbrandt. I'm grateful to him for giving me the opportunity to work in his laboratory at Risø. I would also like to thank Dr. Niels Harrit for his interest and very important contribution to my projects. I want to thank Dr. Rolf Berg for his crucial part in the DNO project. Finally, I'm very thankful for the chance to work in the dynamic environment of Dr. Gary B. Schuster's laboratory.

There are many other friends and fellow students that have been involved in these studies and have helped me in my work. A one big collective THANKS to them all!!!

The financial assistance of the Danish National Research Academy is gratefully acknowledged.

Copenhagen June 2000 Jóhannes Reynisson

Table of contents

Chapter 1

Introduction

1.1 Triphenylmethane dyes

Carbocations can be found everywhere around us, from interstellar space to ones glass of red wine. The colour of red wine, as that of many flowers, fruits and leaves is due, in part, to carbocations.[1] In order to outperform nature, man synthesised a new type of pigments based on the triphenylmethane cation. This class of compounds was among the first of the synthetic dyes to be developed and still finds applications in many fields.[2] These dyes are renowned for their outstanding intensity of colour and their brilliant shades of red, blue and green. The trityl cation and Basic Green 1 dye are depicted in figure 1.1.

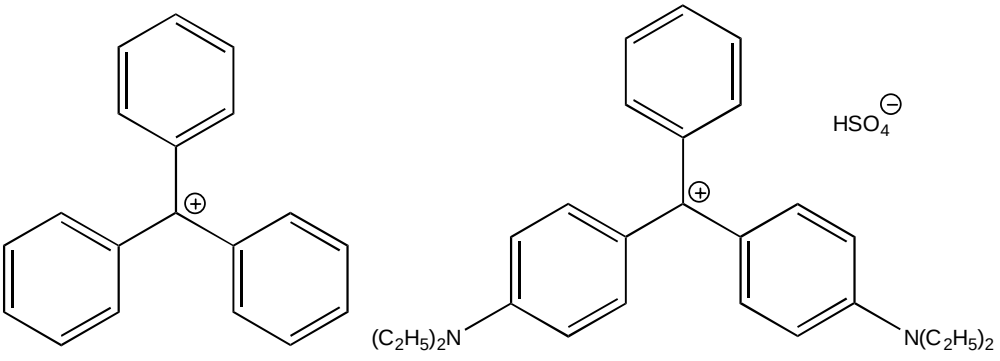

Trityl cation Basic Green 1

Figure 1.1. The chemical structures of the trityl cation and the Basic Green 1 dye and its counter ion.

Triphenylmethane dyes have been extensively employed in the medical and related biological sciences. They exhibit antibacterial properties [3;4] and are used for the disinfection of post – operative wounds.[5] Also dyes of this class are frequently used to assay proteins [6-8] and others are utilised in cytology and histology to stain tissue.[9]

In addition, triphenylmethane dyes are employed as colorants in the photographical,[10] food[11] and cosmetic[11] industries.

1.2 The trioxatriangulenium carbocation

The topic of this thesis is a carbocation, which is a member of the triphenylmethane dye family. Its trivial name is trioxatriangulenium and has the acronym $TOTA^+$. The systematic name is 4,8,12-trioxa-4,8,12,12*c*-tetrahydrodibenzo[*cd*,*mn*]pyrenylium and its chemical structure and counter ion are depicted in figure 1.2.

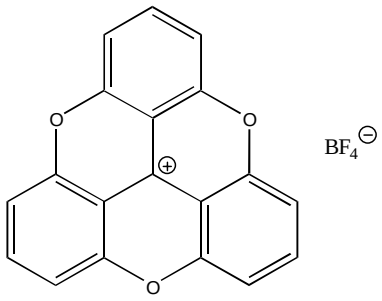

Figure 1.2. The chemical structure of $TOTA^+$ and its counter ion.

$TOTA^+$ was first synthesised by Martin and Smith [12]some forty years ago in Urbana Illinois, USA. Few of $TOTA^+$'s chemical properties have been explored and a small number of publications have appeared in the literature. $TOTA^+$'s one-electron reduction has been investigated by Memcová et al.[13;14] in acetonitrile. They observed that $TOTA^+$ has some unique properties compared to other triphenylmethane dyes, i.e., the neutral radical dimerises very fast, which they attribute to $TOTA^+$'s planar structure. This dimerisation has been further studied with electron spin resonance techniques. [15;16] $TOTA^+$ has also been reduced by chromous ion and was found to be less reactive compared to other carbocations with similar structures.[17] The stability of

$TOTA^+$ has also been investigated by means of electrochemical reduction in sulfuric acid.[18] $TOTA^+$ has also appeared in a paper where steric effects of substituted phenyl groups on triphenylmethane dye molecules are investigated[19] and in a publication where absorption bands are predicted by simple HMO calculations.[20]
Protonation of $TOTA^+$ in CF_3SO_3D has been investigated with ^{1}H-NMR spectroscopy where deuterium is observed to be incorporated at the corner site on $TOTA^+$(see figure 2.1, atom d).[21;22]

Recently, two important papers have been published on $TOTA^+$ and its substituted derivatives where the structures are investigated by means of x-ray crystallography and new synthetic strategies are explored.[23;24] It was found that $TOTA^+$ possesses a planar and rigid structure.

It is noteworthy that $TOTA^+$ is reluctant to nucleophilic attack compared to the structurally related xanthyl (X^+) and 9-phenyl xanthyl (PX^+) closed shell carbocations, as reflected by their pK_{R+} values, being 9.05, [12] -0.84 [25]and 1.0,[26] respectively.

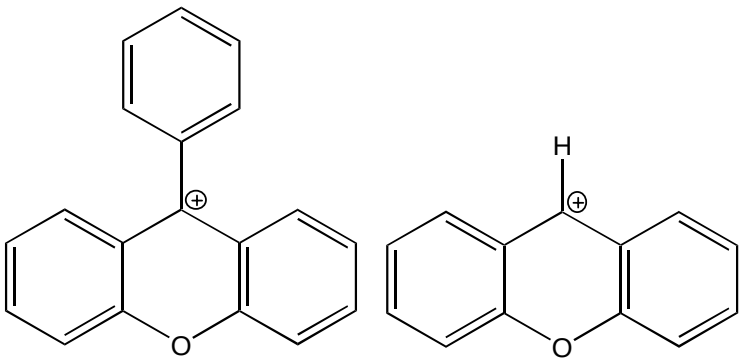

Figure 1.3. 9-phenyl xanthylium (PX^+) and xantyl (X^+).

It is interesting that $TOTA^+$ has not been studied more extensively because it exhibits some unique characteristics seldom encountered for organic molecules. Its more interesting qualities are:

i) $TOTA^+$ is a carbocation

ii) $TOTA^+$ is a planar and has a high symmetry (D_{3h})

iii) $TOTA^+$ is stable

iv) $TOTA^+$ is a electron acceptor due to its cationic nature

v) $TOTA^+$ exhibits absorption bands in the visible spectral region

vi) TOTA fluoresces with a high quantum yield

These attributes make $TOTA^+$ an excellent candidate for the study of bimolecular electron transfer and charge transfer interactions as well as interactions with supramolecular systems like DNA and proteins.

Armed with this knowledge my graduate work spawned four subprojects utilising these exceptional properties of $TOTA^+$:

i) Vibrational Spectroscopic and Quantum Chemical Studies of $TOTA^+$

ii) The Photophysics of $TOTA^+$ and the Electron Transfer Quenching of its Fluorescence

iii) Studies of the $TOTA^+$-DNA Complex and its Photocleavage Properties

iv) Structural Properties of DNO Investigated with Pyrene Excimer Formation

On the following pages brief introductions of the individual subprojects are given together with a brief summary of the mot important results.

1.3 Vibrational Spectroscopic and Quantum Chemical Studies of $TOTA^+$

Unlike the triphenylmethane dyes, most carbocations have short lifetimes as intermediates in S_N1 reactions and their properties have been extensively investigated.[27-29] Such short lived species are often difficult to observe experimentally. Highly acid media, often at cryogenic temperatures have to be employed to stabilise the carbocations or pump – probe techniques can be employed. Techniques such as x-ray crystallography, which allows one to determine the structure, is often not applicable since no crystals can be obtained. Therefore comparatively few detailed geometries of carbocations are available experimentally.[30-32] One of the first reported crystal structures of a carbocation was that of the trityl cation, which was solved more than 30 years ago.[33]

The introduction of accurate theoretical methods and efficient computers has made detailed information about structures and energies of these often highly reactive species possible.[30;31] Experimental data in combination with the results obtained by quantum chemical calculations offers new insights into the complex carbocation chemistry.

Infrared (IR) and Raman spectroscopies are important methods to elucidate geometries and related properties of molecules. Recently, interest in vibrational spectroscopy of carbocations in conjunction with theoretical calculations has increased along with new experimental techniques. For example, FT-IR on samples isolated in solid SbF_5 matrix has led to numerous publications. [34-38]

Vibrational spectroscopy has also been used to some extent to investigate the properties of triphenylmethane dyes. [39;40] Furthermore, in a recent combined X-ray,

Raman and theoretical study, the structure of the trichlorocyclopropenium carbocation was investigated in detail.[41]

Calculations have been used in several ways in the study of carbocations, especially where experiments are difficult, costly and time consuming. It has been found that rather high level *ab initio* calculations (second order Møller – Plesset perturbation treatment using the 6-31G(d) basis set) are needed in order to obtain reliable results, which are in close agreement with those of experimental data. [30;31;42] Since the introduction of the density functional theory (DFT) much evidence has accumulated of its reliability for the computation of molecular structures, vibrational frequencies and energies of chemical reactions [43-46] including calculations on carbocations. [38] The DFT methods are computationally less demanding than the conventional *ab initio* correlation techniques. [43]

Due to $TOTA^+$'s stability it is experimentally accessible and no major problems were encountered acquiring its IR and Raman spectra. As mentioned earlier the x-ray structure has been reported in the literature.[23] By running theoretical calculations it was possible to evaluate different theoretical approaches, i.e., which method yields results most akin to the experimental ones. It is concluded that DFT calculations based on the nonlocal exchange-correlation functionals (UB-LYP) yields the most accurate description of the vibrational spectra and the geometry of $TOTA^+$. As a result of the calculations, it appears that the positive charge in the $TOTA^+$ carbocation is substantially delocalised.

The work carried out in this subproject has appeared in *Journal of Molecular Structure*, 520 (2000) 63-73.

1.4 The Photophysics of $TOTA^+$ and the Electron Transfer Quenching of its Fluorescence

In view of the fact that ground state reactivity is generally augmented in the excited state as a result of enhanced exothermicity upon electronic excitation, it is of interest to explore the properties and interactions of singlet and triplet states of carbocations. In particular, the triphenylmethane dyes have been extensively studied,[2] but several reports on other carbocations have appeared as well. [47-50] Hence, the role of carbocations as electron acceptors in fluorescence quenching [51-57] and ground state charge transfer complexation [58-61] is well established.

Early studies in carbocation photochemistry focused primarily on photoproduct determination following irradiation of cations thermally generated in acidic media.[62-64] Two broad classes of carbocations photoreactions have been noted. [62] In very strongly acidic media such as FSO_3H, the typical reaction is photoisomerisation. In less strongly acidic media, the predominant reaction is electron transfer to give radical intermediates which undergo coupling reactions to form dimeric materials or substitution products.

Generally, the lifetime of the excited state of di- and triphenylmethane dyes is in the picosecond time range in non-viscous solution due to efficient internal conversion coupled to torsional movements of the phenylgroups.[2] When this movement is hindered either by a rigid medium or by binding to natural or synthetic polymers, the fluorescence efficiency and S_1 lifetime are increased.[2] Strong fluorescence is also observed when the rotation is hindered by oxygen bridging as in the closed shell carbocations xanthyl (X^+) and 9-phenylxanthyl (PX^+) (see figure 1.3 and 3.1) [65] and it is generally acknowledged that molecular rigidity is a necessary requirement for efficient fluorescence.

$TOTA^+$ is structurally related to the xanthyl carbocations (see figure 3.1). The photophysical properties and bimolecular electron transfer from aromatic donors to the excited singlet state has been thoroughly investigated for the xanthyl carbocations.[55-57;66] It seemed pertinent to investigate these properties for $TOTA^+$ in order to gain further understanding of these phenomena. The unique properties of $TOTA^+$ made these investigations relatively straightforward. Its stability circumvented complicated techniques in order to generate cationic species. The absorption bands in the visible and near ultra violet made it possible to excite $TOTA^+$ exclusively and not the electronic donors. Also the intrinsic cationic nature of $TOTA^+$ makes it a relatively good electron acceptor.

A strong fluorescence for $TOTA^+$ is observed at 520 nm (τ_{fl} = 14.6 ns, ϕ_{fl} = 0.53 in argon purged acetonitrile), which is readily quenched by ten aromatics. The quenching rate increases with decreasing oxidation potential of the aromatic molecules signifying a charge transfer mechanism, which falls within the normal region of the Marcus theory.[67;68] The Stern-Volmer plots derived from steady state quenching measurements all curve upwards indicating partial static quenching due to complex formation between the ground state of TOTA and the electron donor.[69] The charge transfer complexes are also observed directly by means of electron absorption spectroscopy.

This work is being prepared for publication in *Chemical Physics and Physical chemistry*.

1.5 Studies of the $TOTA^+$-DNA Complex and its Photocleavage Properties

A large number of drugs, particularly those with planar structures, bind to DNA and consequently interfere with its role as a template in replication and transcription. Many drugs form a strong, but reversible, non-covalent complex with DNA by intercalating between adjacent base pairs. These drugs are powerful probes of nucleic acid structure and function, and a number of them are clinically useful chemotherapeutic agents. It has been suggested that this process is responsible for the mutagenicity exhibited by some triphenyl methane dye derivatives, which interferes with DNA replication by causing deletions or insertions of base pairs.[70] The process of intercalation is considered so crucial that the possible formation of an intercalated complex has been proposed for practically every drug known to bind to DNA.[71] It is expedient, therefore, when investigating the mode of binding of dyes/drugs at the molecular level to determine whether or not intercalation occurs.

On the basis of a study of the interaction of proflavine, and chromophores with similar structures (see figure 1.4), with DNA *in vitro*, it was proposed that compounds possessing planar aromatic rings could bind to DNA by intercalation. [72]

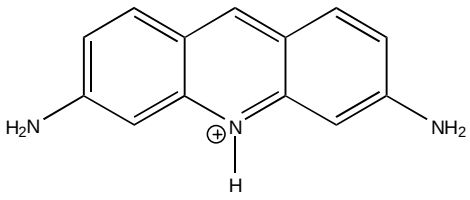

Proflavine

Figure 1.4. The structural formula of proflavine.

This involves the sandwiching of a dye molecule between adjacent base pairs (see figure 1.5), where it is held by van der Waals, stacking and electrostatic forces. As a

consequence, the chromophore of the intercalated dye is constrained to lie parallel to the base pairs above and below it, i.e., more or less perpendicular to the helix axis.

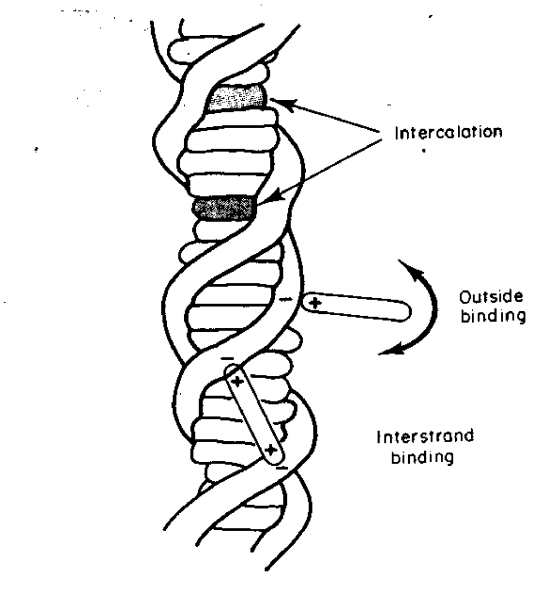

Figure 1.5. A schematic representation of binding modes involved in drug-DNA interactions.

This is ultimately the feature distinguishing intercalation from other modes involving binding to the outside of the helix. The effects on the helix are a local untwisting of the sugar – phosphate backbone and an elongation of the macromolecule. Binding to the major and the minor grooves is also a important DNA – ligand interaction.
In order to be diagnostic for intercalation, a physico-chemical technique must be able to resolve whether or not the bound dyes is parallel to the DNA base pairs.

Intrinsic water solubility is a great asset when organic molecules are studied. A whole range of medicinal utilisations of the molecule is possible, e.g., like close interactions with DNA. If the water solubility is low, ionic groups have to be tagged to a drug in order to make it water soluble thereby risking the loss of the intended biological function.

A potentially negative aspect of a high symmetry of a small organic molecule intended for medicinal purposes, like of $TOTA^+$, is unspecific binding.

The mechanism of migration of charge through the DNA double helix has been under intense investigation for the last few years.[73-75] Recently, a new mechanism was proposed called phonon-assisted polaron like hopping.[76] This idea postulates that the charge distorts the structure of the helix (polaron) and the perturbed region migrates *via* hopping, generated by the thermal motions of DNA in solution (phonon).

The mode of binding was determined as intercalation. Various techniques were employed in order to determine the binding mode such as viscosity, melting point (T_m) and circular dichroism experiments. The results from the viscosity measurements indicate a distorted region where intercalation takes place but crystallographic data is needed for confirmation. Steps are being taken to obtain such x-ray data.

The idea behind this project was to intercalate $TOTA^+$ between the base pairs and thus creating an artificial polaron (the distorted region). The positive charge and high symmetry make $TOTA^+$ and excellent candidate for such an undertaking.

The sequence affinity was also investigated, which show strong affinity towards GC base pairs.

$TOTA^+$ functions as a photonuclease when irradiated at 350 nm and scission takes place at a GG step on a DNA string.

This work is being prepared for submission but to which journal remains to be determined when the results of the DNA – $TOTA^+$ crystal structure are clear.

1.6 Structural Properties of DNO Investigated with Pyrene Excimer Formation

It is a well-known fact that triphenylmethane dyes bind to protein substrates. [2] The biological sciences are taking advantage of the spectral changes accompanying dye – protein binding to assay proteins. A popular protein assay developed by Bradford [6] utilises such spectral changes for the triphenylmethane dye acid blue 90. An assessment of the technique [77] reveals that under assay conditions the dye binds with the protein provided it has a certain macromolecular form and reactive amino acid residues. In particular, interactions occur mainly with arginine and the other basic amino acid residues. Only a slight response is reported of the aromatic amino acids. Binding was attributed to van der Waals forces and hydrophobic interactions.

The objective of this subproject was to probe the structural properties of an oligopeptide (DNO, diamino acid-N^{α}-substituted oligopeptide), substituted with pyrene moieties. It was hoped that the high symmetry of pyrene and $TOTA^{+}$ would lead to extensive interaction, which could be easily monitored. It was envisaged that a sandwich type supramolecular conglomeration would form, $TOTA^{+}$ acting as the salami and the pyrenes as the pieces of bread. The oligopeptide was to hold the whole thing together.

Pyrene absorption and emission is a well documented method used to investigate the properties of macromolecules.[78] DNO oligomer dimers substituted with pyrene as photophysical probes were synthesised. The excimer formation and ground state associations were investigated by means of fluorescence and absorption spectroscopic techniques. A significant difference was observed of the photophysical parameters between the different derivatives, which reflect the structural properties of the DNOs, i.e., a secondary structure of the DNO backbones.

Unfortunately, I was not successful determining the interactions of the $TOTA^+$- DNO complex due to extensive overlap of the absorption and emission spectra of $TOTA^+$ and the pyrene derivatives. Also the low solubility of the DNOs inhibited conclusive results to be reached and further investigations were abandoned.

The results of this of this work have been submitted to the *Journal of Peptide Science* and were accepted for publication in June 2000.

1.7 Reference List

1) Vogel, P. *Carbocation Chemistry*; Elsevier: Amsterdam, 1985;

2) Duxbury, D.F. *Chem.Rev.* **1993**, *93*, 381-433.

3) Green, S.; Longmire, V.; Barton, L.L. *Microbio.Lett.* **1979**, *11*, 111-116.

4) Goldacre, R.J.; Phillips, J.N. *J.Chem.Soc.* **1949**, *3*, 1724-1732.

5) Namiki, N.; Yokoyama, H.; Moriya, K.; Sakakura, M.; Takashima, T.; Yuasa, H.; Kanaya, Y. *Chem.Pharm.Bull.* **1986**, *34*, 922-926.

6) Bradford, M.M. *Anal.Biochem.* **1976**, *72*, 248-254.

7) Compton, S.J.; Jones, C.G. *Anal.Biochem.* **1985**, *151*, 369-374.

8) Krauspe, R.; Scheer, A. *Anal.Biochem.* **1986**, *153*, 242-250.

9) Michaelis, L. *J.Phys.Colloid Chem.* **1950**, *54*, 1-17.

10) Otha, N. *J.Imaging Sci.* **1986**, *30*, 9

11) Richardson, M.L.; Waggot, A. *Ecotoxicol.Environ.Saf.* **1981**, *5*, 424-436.

12) Martin, J.C.; Smith, R.G. *J.Am.Chem.Soc.* **1964**, *86*, 2252-2256.

13) Nemcová, I.; Nemec, I. *J.Electroanal.Chem.* **1971**, *30*, 506-510.

14) Nemcová, I.; Nemec, I. *Chem.zvesti.* **1972**, *26*, 115-125.

15) Sabacky, M.J.; Johnson, C.S.; Smith, R.G.; Gutowsky, H.S.; Martin, J.C. *J.Am.Chem.Soc.* **1967**, *89*, 2054-2058.

16) Müller, E.; Moosmayer, A.; Rieker, A.; Scheffler, K. *Tetrahedron.* **1967**, *39*, 3877-3880.

17) Bowie, W.T.; Feldman, M. *J.Am.Chem.Soc.* **1977**, *99*, 4721-4726.

18) Feldman, M.; Flythe, W.C. *J.Am.Chem.Soc.* **1978**, *43*, 2596-2600.

19) Kessler, H.; Moosmayer, A.; Rieker, A. *Tetrahedron.* **1969**, *25*, 287-293.

20) Nemcová, I.; Malat, M.; Zahradnik, R. *Collect.Czech.Chem.Commun.* **1969**, *34*, 2880-2894.

21) Smith, R.J.; Pagni, R.M. *J.Am.Chem.Soc.* **1979**, *101*, 4769-4770.

22) Smith, R.J.; Miller, T.M.; Pagni, R.M. *J.Org.Chem.* **1982**, *47*, 4181-4188.

23) Krebs, F.C.; Laursen, B.W.; Johansen, I.; Boubekeur, K.; Bechgaard, K.; Jacobsen, C.S.F.A.; Thorup, N. *Act.Cryst.B.* **1998**, *55*, 410-423.

24) Faldt, A.; Krebs, F.C.; Thorup, N. *J.Chem.Soc., Perkin Trans.2* **1997**, 2219-2227.

25) Bethell, D.; Gold, V. *Carbonium Ions, An Introduction*; Academic Press: London, 1967; pp 77

26) Wan, P.; Yates, K.; Boyd, M.K. *J.Org.Chem.* **1985**, *50*, 2881-2886.

27) Olah, G.A.; Schleyer, P.v.R. *Carbonium Ions*; Wiley & Sons, Inc.: New York, 1970;

28) Olah, G.A.; Prakash, G.K.S.; Willams, R.E.; Field, L.D.; Wade, K. *Hydrocarbon Chemistry*; Interscience: New York, 1987;

29) Prakash, G.K.S.; Schleyer, P.v.R. *Stable Carbocation Chemistry*; Wiley & Sons, Inc.: New York, 1997;

30) Saunders, M.; Jimenez-Vazques, H.A. *Chem.Rev.* **1991**, *91*, 375-397.

31) Buzek, P.; Schleyer, P.v.R.; Sieber, S. *Chemie in unseren Zeit* **1992**, *26*, 116-128.

32) Laube, T. *Acc.Chem.Res* **1995**, *28*, 399-405.

33) Mesquita, A.H.G.D.; MacGillavry, C.H.; Eriks, K. *Act.Cryst.* **1965**, *18*, 437-443.

34) Schleyer, P.v.R.; Maerker, C. *Pure & Appl.Chem.* **1995**, *67*, 755-760.

35) Koch, W.; Schleyer, P.v.R.; Buzek, P.; Liu.B. *Croat.Chem.Acta.* **1992**, *65*, 655-672.

36) Vancik, H.; Mihalic, Z.; Kidemet, D. *Croat.Chem.Acta.* **1996**, *69*, 1511-1520.

37) Vancik, H. *Pure & Appl.Chem.* **1995**, *67*, 761-767.

38) Vancik, H.; Novak, I.; Kidemet, D. *J.Phys.Chem.* **1997**, *101*, 1523-1525.

39) Weston, R.E.; Tsukamoto, A.; Lichtin, N.N. *Spectrochim.Acta* **1966**, *22*, 433-453.

40) Aleksandrov, I.V.; Bobovich, Y.S.; Vartanyan, A.T.; Sidorov, A.N. *Opt.Spectrosc.* **1977**, *42*, 35-38.

41) Clark, G.R.; Taylor, M.J.; Steele, D. *J.Chem.Soc.Faraday Trans.* **1993**, *89*, 3597-3601.

42) Reindl, B.; Clark, T.; Schleyer, P.v.R. *J.Comp.Chem.* **1996**, *17*, 1406-1430.

43) Wong, M.W. *Chem.Phys.Lett.* **1996**, *256*, 391-399.

44) Ziegler, T. *Chem.Rev.* **1991**, *91*, 651-667.

45) Seminario, J.M.; Politzer, P. *Modern Density Functional Theory: a Tool for Chemistry*; Elsevier: Amsterdam, 1995;

46) Scott, A.P.; Radom, L. *J.Phys.Chem.* **1996**, *100*, 16502-16513.

47) Shukla, D.; Wan, P. *J.Photochem.Photobio.A.* **1993**, *76*, 47-53.

48) Clifton, M.F.; Fenick, D.J.; Gasper, S.M.; Falvey, D.E.; Boyd, M.K. *J.Org.Chem.* **1994**, *59*, 8023-8029.

49) Cozens, F.L.; Garcia, H.; Scaiano, J.C. *Langmuir* **1994**, *10*, 2246-2249.

50) Mo, Y.R.; Jiao, H.J.; Ling, Z.Y.; Schleyer, P.V. *Chem.Phys.Lett.* **1998**, *289*, 383-390.

51) Johnston, L.J.; Lobaugh, J.; Wintgens, V. *J.Phys.Chem.* **1989**, *93*, 7370-7374.

52) Johnston, L.J.; Kanigan, T. *J.Am.Chem.Soc.* **1990**, *112*, 1271-1273.

53) Johnston, L.J.; Wong, D.F. *J.Phys.Chem.* **1993**, *97*, 1589-1595.

54) Johnston, L.J.; Wong, D.F. *Can.J.Chem.* **1992**, *70*, 280-282.

55) Samanta, A.; Gopidas, K.R.; Das, P.K. *J.Phys.Chem.* **1993**, *97*, 1583-1588.

56) Samanta, A.; Gopidas, K.R.; Das, P.K. *Chem.Phys.Lett.* **1990**, *167*, 165-169.

57) Azarani, A.; Berinstain, A.B.; Johnston, L.J.; Kazanis, S. *J.Photochem.Photobiol.A.* **1991**, *57*, 175-189.

58) Takahashi, Y.; Sankararaman, S.; Kochi, K. *J.Am.Chem.Soc.* **1989**, *111*, 2954-2697.

59) Feldman, M.; Winstein, S. *J.Am.Chem.Soc.* **1961**, *83*, 3338-3339.

60) Feldman, M.; Graves, B.G. *J.Phys.Chem.* **1966**, *70*, 955-956.

61) Dauben, H.J.; Wilson, J.D. *Chem.Commun.* **1968**, 1629-1630.

62) Childs, R.F.; Shaw, G.B. *Org.Photochem.* **1991**, *11*, 111

63) Childs, R.F. *Rev.Chem.Intermed.* **1980**, *3*, 285-314.

64) Cabell-Whiting, P.W.; Hogeveen, H. *Adv.Phys.Org.Chem.* **1973**, *10*, 129-153.

65) Boyd, M.K. *Organic Photochemistry*; Ramamurthy, V., Schanze, K.S., Eds.; Marcel Dekker: New York, 1997; pp 147-186.

66) Bedleck, J.M.; Valentino, M.R.; Boyd, M.K. *J.Photochem.Photobio.A:Chem.* **1996**, *94*, 7-13.

67) Marcus.R.A. *J.Chem.Phys.* **1965**, *43*, 679-683.

68) Marcus.R.A.; Sutin, N. *Biochimica et Biophysica Acta* **1985**, *811*, 265-322.

69) Lakowicz, J.R. *Principles of Fluorescence Spectroscopy*; Plenum Press: New York, 1983; pp 7-7.

70) Bradley, D.F.; Lifson, S. *Molecular Associations In Biology*; Academic Press: New York, 1968; pp 261

71) Dougherty, G.; Pilbrow, J.R. *Int.J.Biochem.* **1984**, *16*, 1179-1192.

72) Lerman, L.S. *J.Mol.Biol.* **1961**, *3*, 18-30.

73) Wan, C.; Fiebig, T.; O'Kelley, S.; Treadway, C.R.; Barton, J.K.; Zewail, A.H. *Proc.Nat.Acad.Sci.USA* **1999**, *96*, 6014-6022.

74) Murphy, C.J.; Arkin, M.R.; Jenkis, Y.; Ghatlia, N.D.; Bossmann, S.H.; Turro, N.J.; Barton, J.K. *Science* **1993**, *262*, 1025-1029.

75) Ly, D.; Kan, Y.; Armitage, B.; Schuster, G.B. *J.Am.Chem.Soc.* **1996**, *118*, 8747-8748.

76) Henderson, P.T.; Jones, D.; Hampikian, G.; Kan, Y.; Schuster, G.B. *Proc.Nat.Acad.Sci.USA* **1999**, *96*, 8353-8358.

77) Neuhoff, V.; Stanism, R.; Eibl, H. *Electrophoresis* **1985**, *6*, 427-448.

78) Winnik, F.M. *Chem.Rev.* **1993**, *93*, 587-614.

Chapter 2

Vibrational Spectroscopic and Quantum Chemical Studies of TOTA

2.1 Introduction

As previously noted, TOTA is stabile in its crystalline form and some polar solvents. Most carbocatioinic species are far to short lived to be investigated with conventional steady state instrumentation or let alone crystals to be grown. This intrinsic property of carbocations made the stable TOTA carbocation an ideal subject in order to compare experimental results with quantum chemical calculations. Recently, its X-ray geometrical structure was published[1] but no vibrational investigations of TOTA have been reported in the literature.

In the present chapter, experimentally obtained Raman and IR spectra of TOTA are analysed with the help of theoretical *ab initio* and DFT calculations. Furthermore, the theoretically optimised structures are compared to the known X-ray crystal structure of TOTA.

2.2 Experimental

Trioxatriangulenium tetrafluoroborate (TOTA, 4,8,12-trioxa-4,8,12,12*c*-tetrahydrodibenzo[*cd, mn*]pyrene tetrafluoroborate) was synthesized according to the procedure published by Faldt *et al.* [2]

The infrared spectrum of TOTA was measured on a Perkin-Elmer FT-IR 1760X instrument in a KBr pellet.

The FT-Raman spectrum was measured on a Bruker IFS-65 Raman spectrometer from a solid sample using an excitation wavelength of 1064 nm (Nd-YAG, 300 mW). The Raman spectrum, recorded with an excitation wavelength of 782 nm, was acquired from a solid sample by means of a Renishaw Raman microscope with a diode laser as a light source.

In order to obtain a pre-resonance Raman spectrum, spectra from a concentrated solution of TOTA in methanol (ca. 10^{-3} M) were recorded with pulsed excitation from an optical parametric oscillator (Continuum, Sunlite, OPO), 3.0 mJ at 680 nm. The OPO was pumped with a Nd-YAG laser at 355 nm (Continuum, Powerlite, PL9010). The detector employed was a liquid nitrogen cooled CCD (Charged Coupled Device) (Princeton Instruments, Inc. LN/CCD-1100-PB/VISAR/1). A single monochromator with a grating of 1200 grooves/mm, Jobin Yvon T64000) was utilised to analyse the scattered light. Spinning optical cells made out of quartz were employed. The dimensions of the cells were 3.0 cm in diameter and 1.3 cm in height. The solvent (HPLC-quality) was used as received. Absorption spectra were recorded on a Perkin-Elmer Lambda 5 Spectrophotometer.

2.3 Quantum Chemical Calculations

Ab initio and density functional theory (DFT) calculations were carried out using the *Gaussian 98* program[3] employing restricted closed shell wave function. The geometry of TOTA was optimised in D_{3h} point group. Vibrational frequencies were calculated at the optimised geometry using analytical derivative techniques. The *ab initio* calculations were carried out using restricted Hartree-Fock (RHF) and Møller-Plesset second order perturbation (MP2) methods.[4] The DFT calculations were carried out using the non-local BLYP functional [5-7] and B3LYP[7] hybrid methods. The standard 6-31G(d) [8] basis set was used.

2.4 Results

2.4.1 Geometry

Figure 2.1 depicts the numbering of bonds and angles of TOTA and tables 2.1 and 2.2 list the geometrical parameters of TOTA carbocation obtained by the *ab initio* and DFT theoretical calculations.

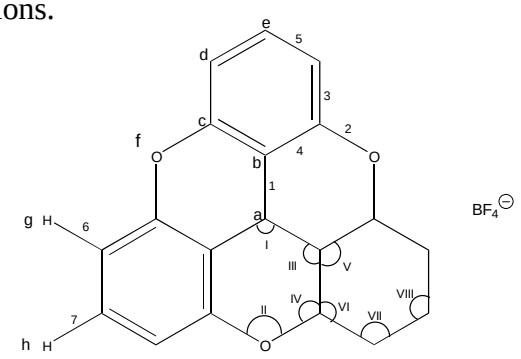

Figure 2.1. Trioxatriangulene and its counter ion.
Numbering of bonds, angles and atoms of TOTA.

Table 2.1. Calculated and experimental bond lengths of TOTA (in Ångstrøm).

Bonds	RHF	BLYP	MP2	B3LYP	X-Ray [a]	ΔRHF	ΔBLYP	ΔMP2	ΔB3LYP
1	1.392	1.408	1.414	1.398	1.392	0.000	0.016	0.022	0.006
2	1.350	1.388	1.416	1.371	1.376	0.026	0.012	0.040	0.005
3	1.375	1.397	1.400	1.387	1.378	0.003	0.019	0.022	0.009
4	1.401	1.424	1.427	1.413	1.403	0.002	0.021	0.024	0.010
5	1.394	1.413	1.419	1.403	1.400	0.006	0.013	0.019	0.003
6	1.107	1.091	1.089	1.084	0.931	0.176	0.160	0.158	0.153
7	1.107	1.093	1.089	1.086	0.952	0.155	0.141	0.137	0.134
					rms[b]:	0.012	0.017	0.026	0.007

[a] Taken from reference [1]
[b] Bonds 6 and 7 not included

Table 2.2. Calculated and experimental bond angles of TOTA (in degrees).

Angles	RHF	BLYP	MP2	B3LYP	X-Ray [a]	ΔRHF	ΔBLYP	ΔMP2	ΔB3LYP
I	120.0	120.0	120.0	120.0	120.0	0.0	0.0	0.0	0.0
II	122.4	120.8	120.0	121.3	120.5	1.9	0.3	0.5	0.8
III	119.1	119.5	120.1	119.3	119.6	0.5	0.1	0.5	0.3
IV	119.7	120.1	119.9	120.0	120.2	0.5	0.1	0.3	0.2
V	121.9	121.0	119.9	121.3	120.9	1.0	0.1	1.0	0.4
VI	119.4	119.7	120.5	119.5	119.9	0.5	0.2	0.6	0.4
VII	117.7	118.0	118.1	118.0	117.8	0.1	0.2	0.3	0.2
VIII	124.1	123.5	122.9	123.6	123.8	0.3	0.3	0.9	0.2
					rms:	0.8	0.2	0.6	0.4

[a] Taken from reference [1]

The crystal structure of TOTA has been reported and its parameters are shown in tables 2.1 and 2.2 for comparison [1]. The counter ion used for the given crystal structure is tetrafluoroborate (BF_4^-).[1] The crystal structure shows that the molecular framework of TOTA exhibits complete planarity of quasi D_{3h} symmetry.[1] The *ab initio* and DFT theoretical calculations predict D_{3h} symmetry. The deviations from the crystal structure of the theoretical calculations are shown in tables 2.1 and 2.2 as Δ. The total root mean square error (rms) was calculated for the deviations according to the equation:

$$rms = \sqrt{\frac{\sum_{i}^{N}\left(\lambda\omega_i^{th} - \omega_i^{\exp}\right)^2}{N}}$$

N is the number of parameters used, λ is a scaling factor and ω_i^{th} and ω_i^{exp} are the theoretical and experimental bond lengths, angles and frequencies.

The rms values for the theoretical methods are given in tables 2.1, 2.2 and 2.4. The hydrogen bond lengths are not included in the rms values in table 1. For the bond lengths B3LYP and RHF methods show the best results. The RHF calculation predicted bond 1 accurately but bond 2 is 0.026 Å off. This indicates that the low rms value for the RHF method is not due to its accuracy. On the other hand B3LYP shows an overall more accurate prediction and therefore should be considered more reliable. MP2 and BLYP both overcompensate for the electron correlation and give systematically longer bonds than the experimental results. The bond lengths of the hydrogen atoms of TOTA are predicted too long for all the theoretical methods when compared to the X-ray crystal structure. Hydrogen atoms have a poor response to X-ray diffraction because they have only one scattering electron. The accuracy of the

hydrogen bond lengths is therefore lower than for the other bonds and they should be treated more carefully.

The rms values for the angles are given in table 2.2. The angles are expected to reflect better how the different methods perform: if the bond length error is systematic, the error for the angles should cancel. The *ab initio* methods do not predict the angles as accurately as the DFT methods.

2.4.2 Charge distribution

The total atomic charges (Mulliken charges) and the results of natural bond orbital (NBO) analysis are shown in table 2.3.

Table 2.3. The total atomic (Mulliken) and natural bond order (NBO) charges derived from the theoretical calculations.

	Mulliken charges				NBO[a]		
Atom	RHF	MP2	BLYP	B3LYP	RHF	BLYP	B3LYP
a	0.26	0.21	0.18	0.19	0.24	0.09	0.12
b	-0.02	-0.02	0.07	0.02	-0.25	-0.14	-0.16
c	0.50	0.50	0.30	0.34	0.47	0.36	0.38
d	-0.27	-0.22	-0.15	-0.17	-0.32	-0.26	-0.27
e	-0.14	-0.14	-0.10	-0.12	-0.09	-0.16	-0.15
f	-0.73	-0.81	-0.50	-0.55	-0.54	-0.41	-0.44
g	0.28	0.28	0.17	0.20	0.28	0.27	0.27
h	0.28	0.27	0.17	0.20	0.27	0.27	0.28

[a] NBO: Natural Bond Orbitals

The electron distribution can be evaluated from the theoretical results and compared to the resonance structures of TOTA shown in figure 2.2 (see next page). All methods agree qualitatively in localising most of the positive charge in position c and, to a lesser extent, in position a (see figure 2.1). Hence, the charge seems substantially delocalised in the molecule. The second resonance structure in figure 2.2 bears most of the positive charge followed by the first. The third and fourth resonance structures show negative charges according to the theoretical calculations

(see table 2.3), the third one due to the electrophilic nature of the oxygen atoms and the fourth one because the hydrogen atoms seem to contribute some of their charge, stabilising the carbocation.

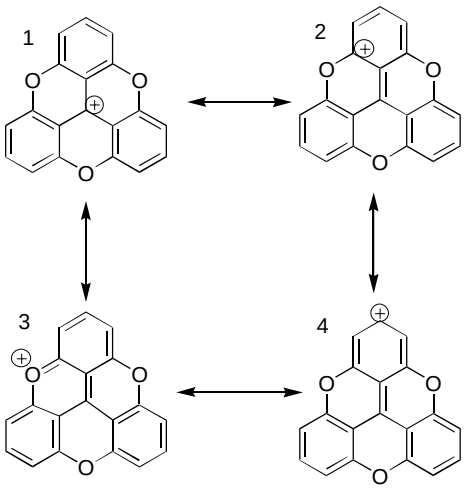

Figure 2.2. The main resonance structures of TOTA.

2.4.3 Vibrational spectra

A molecule or ion containing *n* atoms has 3*n*-6 normal modes of vibration. TOTA containing 31 atoms thus has 87 normal modes of vibration. TOTA transforms according to D_{3h} symmetry and therefore has six irreducible representations. Out of 87 normal modes of vibration 10A'$_1$ and 9E" are Raman active, 7A"$_2$ are IR active and 20E' are Raman and IR active. 9A'$_2$ and 3A"$_1$ are vibrationally inactive. A'$_1$, A'$_2$ and E' represent the in plane vibrational modes and A"$_1$, A"$_2$ and E" represent the out of plane vibrational modes.

The results from the theoretical calculations and experimental spectra are shown in table 2.4 (see next page). The experimental FT-IR, FT-Raman and the theoretical B3LYP spectra are shown in figures 2.3 and 2.4. Raman spectra obtained with different excitation wavelengths are compared in figure 2.5.

Table 2.4. See table IV in special file

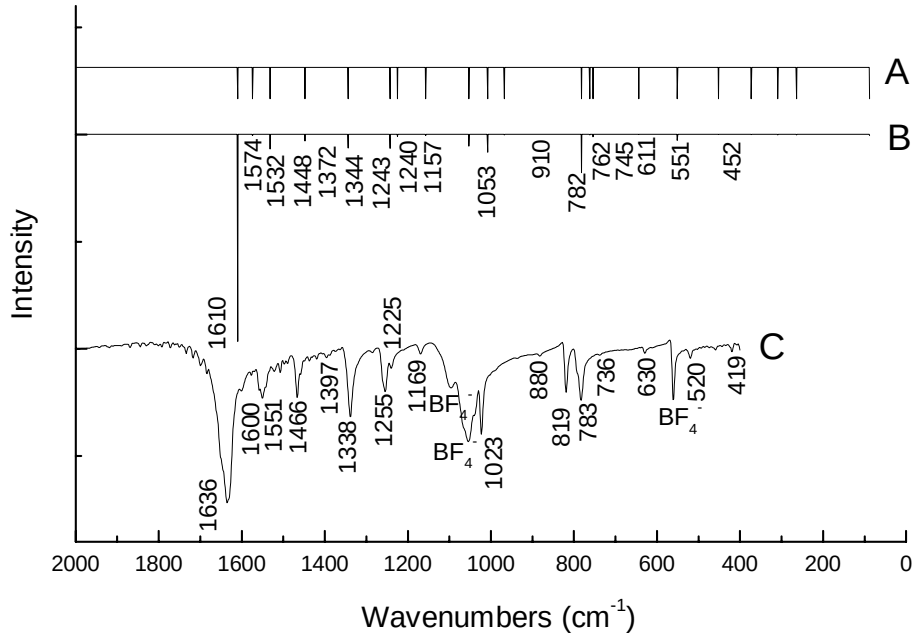

Figure 2.3. Observed and calculated IR spectra.
A: all IR active modes.
B: Calculated B3LYP/6-31G(d) spectrum.
C: Experimental FT-IR spectrum.

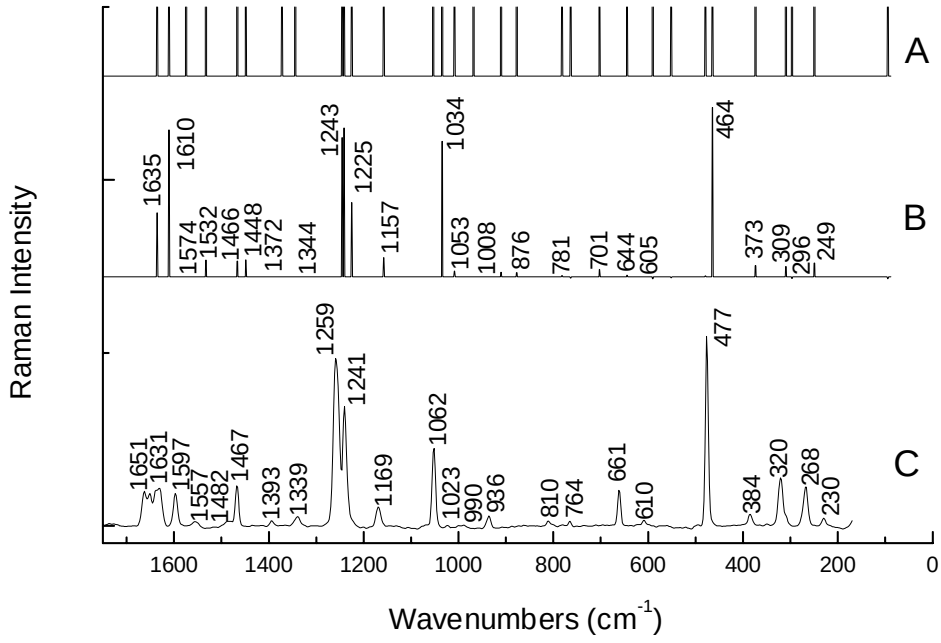

Figure 2.4. Observed and calcualted Raman spectra.
A: All Raman active modes.
B: Calculated B3LYP/6-31G(d) Raman spectrum.
C: Observed FT-Raman spectrum
from a powder sample, λ_{exc}=1.064 μm

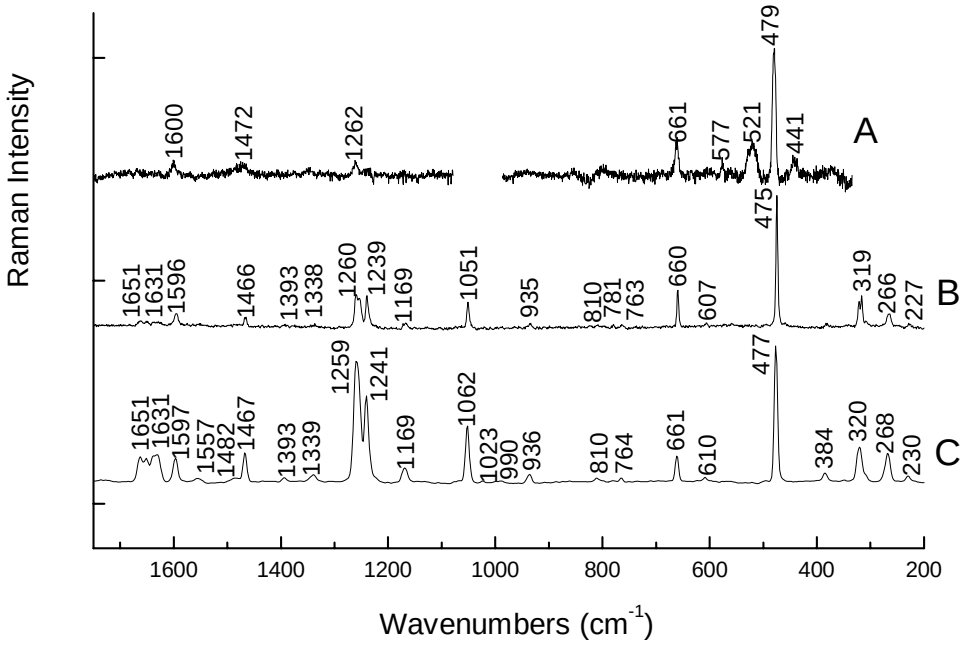

Figure 2.5. Raman spectra obtained with different excitation wavelengths.
A: λ_{exc}=680 nm (solution in methanol)
B: λ_{exc} =782 nm (powder)
C: λ_{exc} =1064 nm (FT-Raman, powder)

Tetrafluoroborate ion is the counter ion for TOTA. The peaks at 561, 1053, and 1095 cm^{-1} in the FT-IR spectrum (figure 2.3) are due to the vibrational absorption of the counter ion,[9] while[10] the reported Raman active frequencies of the tetrafluoroborate ion are too weak to be observed in the TOTA Raman spectra.[11;12] No imaginary frequencies were produced for the RHF and DFT calculations under D_{3h} symmetry, which indicates that real minima were reached on the potential energy surfaces in both cases.

Frequency calculations for MP2 were not possible since the computer facilities available were not able to cope with the heavy computational demand required for such theoretical calculations.

2.5 Discussion

2.5.1 Geometry

The bond lengths are computed reasonably well with all theoretical methods. B3LYP calculates the most accurate bond lengths compared to the crystal structure. This method contains Becke's three-parameter exchange functional that predicts the resonance effect of the TOTA carbocation well. On the whole RHF comes close to the crystal structure when bond lengths are considered but fails to predict the bond length of the oxygen bridge (bond 2, figure 2.1). This indicates that the RHF method fails to reproduce adequately the resonance effect generated by the oxygen bridges because electrons of opposite spin remain uncorrelated in the HF theory.[13] MP2 and BLYP overestimate the bond lengths for TOTA. The electron correlation factors seem to overdo the electron repulsive interactions explaining the longer bond lengths compared to the crystal structure.

The DFT methods predict the angles more accurately than the *ab initio* methods. The bond length deviations for the DFT methods are more systematic implying that the angles are more precise. BLYP does better than B3LYP, which indicates that BLYP bond predictions have a more systematic error than B3LYP. The *ab initio* methods deviate from the crystal structure mainly due to the poor prediction of bond 2 (see figure 2.1).

The term accurate structure[14] has been suggested to designate geometries known in detail, that is within error limits of a degree or two in angles and ca. 0.02 Å in bond lengths. When the crystal structure of TOTA is compared to the theoretically obtained structures and the crystal structure is taken as accurate then the theoretical predictions for the angles are within the limits of two degrees for all the structures. The B3LYP method achieves the criteria for an accurate structure concerning the

bond lengths. The BLYP method predicts bond 4 and the RHF method bond 2 too long as compared to the crystal structure (see figure 2.1). All the bonds are calculated more than 0.02 Å too long for the MP2 method.

The hydrogen bond lengths do not fulfil the condition as accurate for any of the theoretical methods compared to the crystal structure. However, the spatial position of the hydrogen atoms compared to the framework of the TOTA carbocation is less accurately determined experimentally due to hydrogen's poor response to X-ray diffraction but the difference between the crystal structure and the theoretical results are to great to be ignored. It is possible that the theoretical methods overplay the role of the hydrogen atoms stabilising the carbocation by contributing some of their electron density to the framework of TOTA.

2.5.2 Charge distribution

The total atomic charges and the NBO analysis give an estimate of the electron distribution in TOTA. It is apparent from these calculations that most of the positive charge of TOTA resides on the c atoms (see table 2.3) and the hydrogen atoms. The hydrogen bonds are found shorter for the crystal structure than predicted by the theoretical methods and therefore it is questionable to assume that the hydrogen atoms bear as much positive charge as predicted by the theoretical methods. Other techniques are better suited to validate the stabilisation effect of the hydrogen atoms. An interesting option to investigate the properties of the hydrogen atoms is the IGLO method (individual gauge for localised molecular orbitals)[15] that allows the calculation of magnetic susceptibilities and chemical shifts of organic molecules, which can be compared to ^{1}H-NMR spectra.

2.5.3 Vibrational Spectra

Molecular frequencies depend on the second derivative of the energy with respect to the nuclear coordinates. The calculated frequencies are given in table 2.4 along with calculated intensities. Table 2.4 also contains the experimentally measured frequencies and their assignments. Seventeen vibrational modes were observed in the FT-IR spectrum (excluding the hydrogen vibrations). Six of these were easily assigned to the B3LYP calculated vibrational modes being 1610, 1532, 1448, 1344, 1243 and 1053 cm^{-1} which are all of the E' symmetry. Assignments of the calculated (B3LYP) modes at 1574, 1225, 1157, 762 and 551 cm^{-1} of the E' symmetry and at 782 cm^{-1} of A_2" symmetry were less obvious than the six vibrational modes mentioned above but satisfactory. The remaining observed vibrational modes were assigned to those at 1397 and 910 cm^{-1} of E' symmetry and those at 745, 611 and 452 cm^{-1} of A_2" symmetry. All assigned modes are thus of either E' or A_2" symmetry types. Of these, all the intense observed bands are of E' symmetry. Twenty-seven vibrational modes were observed for the Raman spectra. Unambiguous assignments were made to the calculated (B3LYP) modes at 1610, 1243(1241), 1225, 1157 and 551 cm^{-1} of E' symmetry and those at 1635, 1034 and 464 cm^{-1} of A_1' symmetry. The observed peak at 1259 cm^{-1} (excitation at 1064 nm) is assigned to two calculated B3LYP (1243, 1241 cm^{-1}) modes since both are predicted to have relatively strong intensity. The somewhat larger bandwidth of this observed band is and additional indication of two overlapping bands. Satisfactory assignments were made to the calculated bands at 1574, 1448, 1053, 644, 373 and 309 cm^{-1} of E' symmetry and 701 cm^{-1} of A1' symmetry. The rest of the observed vibrational modes were assigned to calculated bands at 1532, 1372, 1344 and 1008 cm^{-1} of E' symmetry, 876, 781, 605, 479, 296 and 249 cm^{-1} of E" symmetry and 1466 and 591 cm^{-1} of A_1'

symmetry. Similarly to the assignment of the IR spectrum, the predominant symmetry is E' but some of the certain assignments involve A_1' modes as well. Qualitatively very satisfactory overall agreement between the experimental and calculated spectra is observed. The vibrational mode of the Raman band at 464 cm^{-1} (figure 4B) and the IR peak at 1610 cm^{-1} (figure 3B) are shown in figure 2.6. Those are the vibrations, which cause the strongest bands in the IR and Raman spectra.

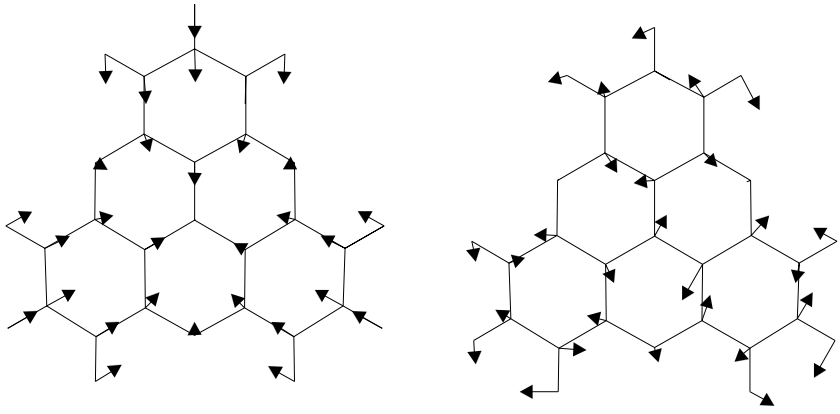

464 cm^{-1} (Raman) 1610 cm^{-1} (IR)

Fig. 2.6. Geometrical displacements for the two strong IR and Raman modes.

The displacement of this Raman band corresponds essentially to a totally symmetric stretching vibration of the whole core of the molecule, with elongation of all bonds. It is interesting to note that this band is the one being mostly enhanced when approaching resonance conditions with the first electronic absorption band (476 nm) of TOTA. This is illustrated in figure 2.6, implying that this electronic transition mainly involves a symmetrical core expansion of the whole molecule.

From table 4 it is apparent that the different theoretical methods yield rather similar results, which again correlates well with experimental data. The rms values obtained for the different theoretical methods (see table 2.4) when compared to the

experimental obtained frequencies demonstrate that the B3LYP method is the most reliable of the methods used.

2.6 Conclusion

In conclusion, qualitatively very satisfactory agreement between experimental and calculated vibrational spectra is observed and the X-ray crystal structure is well reproduced, by the theoretical methods. Of the theoretical methods used, the B3LYP method produces the most accurate vibrational spectra and geometry of TOTA. Substantial delocalisation of the positive charge is predicted by calculations.

2.7 Reference List

1) Krebs, F.C.; Laursen, B.W.; Johansen, I.; Boubekeur, K.; Bechgaard, K.; Jacobsen, C.S.F.A.; Thorup, N. *Act.Cryst.B.* **1998**, *55*, 410-423.

2) Faldt, A.; Krebs, F.C.; Thorup, N. *J.Chem.Soc., Perkin Trans.2* **1997**, 2219-2227.

3) M.J.Frisch, G.W.Trucks, H.B.Schlegel, G.E.Scuseria, M.A.Robb, J.R.Cheeseman, V.G.Zakrzewski, J.A.Montgomery, R.E.Stratmann, J.C.Burant, S.Dapprich, J.M.Millam, A.D.Daniels, K.N.Kudin, M.C.Strain, O.Farkas, J.Tomasi, V.Barone, M.Cossi, R.Cammi, B.Mennucci, C.Pomelli, C.Adamo, S.Clifford, J.Ochterski, G.A.Petersson, P.Y.Ayala, Q.Cui, K.Morokuma, D.K.Malick, A.D.Rabuck, K.Raghavachari, J.B.Foresman, J.Cioslowski, J.V.Ortiz, B.B.Stefanov, G.Liu, A.Liashenko, P.Piskorz, I.Komaromi, R.Gomperts, R.L.Martin, D.J.Fox, T.Keith, M.A.Al-Laham, C.Y.Peng, A.Nanayakkara, C.Gonzalez, M.Challacombe, P.M.W.Gill, B.Johnson, W.Chen, M.W.Wong, J.L.Andres, M.Head-Gordon, E.S.Replogle, and J.A.Pople. Gaussian 98. (A.3). 1998. Pittsburg PA, Gaussian Inc.

4) Møller, C.; Plesset, M. *Phys.Rev.* **1934**, *46*, 618-622.

5) Becke, A.D. *Phys.Rev.B* **1993**, *98*, 5648-5652.

6) Becke, A.D. *Phys.Rev.A.* **1988**, *38*, 3098-3100.

7) Lee, C.; Yang, W.; Parr, R.G. *Phys.Rev.B.* **1988**, *37*, 785-789.

8) Hariharan, P.C.; Pople, J.A. *Theor.Chim.Acta* **1973**, *28*, 213-222.

9) Sharp, D.W.A.; Sheppard, N. *J.Chem.Soc.* **1957**, 674-682.

10) Weston, R.E.; Tsukamoto, A.; Lichtin, N.N. *Spectrochim.Acta* **1966**, *22*, 433-453.

11) Goubeau, V.J.; Bues, W. *Z.Anorg.Allgem.Chem.* **1952**, *268*, 221-228.

12) Greenwood, N.N. *J.Chem.Soc.* **1959**, 3811-3815.

13) Foresman, J.B.; Frisch, *Æ.Exploring Chemistry with Electronic Structure Methods*; Gaussian Inc.: Pittsburg, 1996;

14) Domeniciano, A.; Hargittai, I.*Accurate Molecular Structures-Their Determination and Importance*; Oxford University Press: Oxford, 1992;

15) Kutzelnigg, W. *Isr.J.Chem.* **1980**, *19*, 193-200.

16) Scott, A.P.; Radom, L. *J.Phys.Chem.* **1996**, *100*, 16502-16513.

17) Wong, M.W. *Chem.Phys.Lett.* **1996**, *256*, 391-399.

Chapter 3

The Photophysics of $TOTA^+$ and the Electron Transfer Quenching of its Fluorescence

3.1 Introduction

While the excited states of aromatic carbocations, like the triphenylmethane dyes[1], have been extensively studied, the excited states of $TOTA^+$ have not yet been explored. This chapter presents the initial investigations of the physical properties of the lowest excited singlet (S_1) and triplet (T_1) states of $TOTA^+$. The singlet state displays a fluorescence lifetime τ_{fl} = 14.6 ns in argon purged acetonitrile, which is sufficiently long to permit bimolecular electron-transfer. This process is investigated for ten aromatic electron donors and found to occur within the normal region of the Marcus theory. Ground state charge transfer complexation between $TOTA^+$ and the π-donors is demonstrated. The triplet lifetime is τ_T = 23.2 μs in argon purged acetonitrile and the transient absorption spectrum of the triplet is measured. The results are compared with the photophysical properites of the xanthylium (X^+) and 9-phenyl xanthylium (PX^+) carbocations. Their chemical structures are depicted in figure 3.1 along with $TOTA^+$.

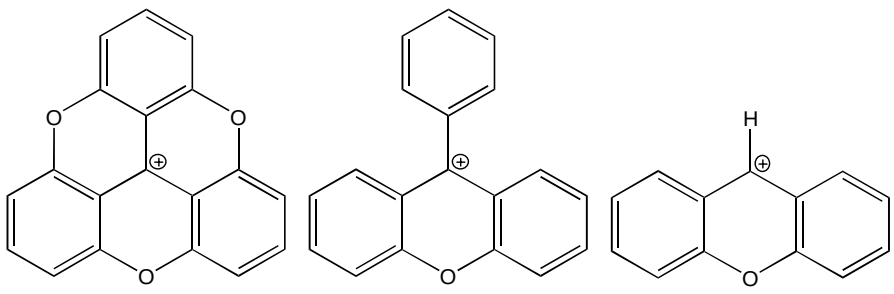

Figure 3.1. Trioxatriangulenium ($TOTA^+$), 9-phenyl xanthylium (PX^+) and xantyl (X^+).

3.2 Experimental

Trioxatriangulenium (4,8,12-trioxadibenzo[*cd*,*mn*]pyrenylium) was synthesised according to the procedure published by Faldt *et al*.[2] Acetonitrile (Labscan, Analytical Science) and other reagents were used as received. The water used as solvent was triply distilled.

The absorption spectra were measured on a Perkin-Elmer Lambda 5 UV/VIS spectrophotometer with 1 nm resolution in 1×1 cm optical quartz cells.

Ground state complex formation was investigated by the means of 1×1 cm optical quartz cells (Helma – 238 – Q), which have two identical chambers in tandem with the light beam. An absorption spectrum was run with the solutions in separate chambers. Then the solutions were mixed and another spectrum was obtained. Saturated or very highly concentrated solutions of $TOTA^+$ and the π-donors in acetonitrile were employed.

Steady state fluorescence emission spectra were obtained on an FS900 Edinburgh Analytical Instruments emission spectrometer with 1.8 nm resolution. For emission quantum yields, Lucifer Yellow CH in water ($\phi_{fl} = 0.21$)[3;4] was used as a reference. Fluorescence lifetimes were measured on a time-correlated single-photon-counting (SPC) apparatus (FL900, Edinburgh Analytical Instruments) equipped with a Hamamatsu R1527 photomultiplier and a nitrogen filled nanosecond flash lamp. The nitrogen lines at 337 nm and 407 nm were used for excitation and emission was detected at 520 nm. All samples were purged with argon prior to measurements. A ludox dispersion was used to obtain the instrument response function. Fluorescence decay curve analysis was performed by de convolution of the instrument response function with an assumed decay law. The decay parameters were determined by a

least-squares fitting routine, the quality of which was evaluated by the reduced χ^2 values, as well as by the randomness of the weighted residuals.

Both steady state and time-resolved fluorescence experiments were performed in the normal 90° configuration with a standard 1×1 cm optical quartz cell. The concentration of $TOTA^+$ was ~1×10^{-5} M for all the fluorescence experiments. All the experiments mentioned above were performed at room temperature.

In the laser flash photolysis experiments a quartz cuvette of the proportions: 25 mm long, 9 mm wide and 20 mm tall was used. It was connected to the solution reservoir by an airtight glass tubing. The solutions were purged with argon prior to irradiation for at least 20 min. Solutions of $TOTA^+$ were prepared in acetonitrile and triply distilled water with $A_{308} = 0.600$ ($[TOTA^+] = 1\times10^{-4}$ M). 20 μL of 48% wt. tetrafluoroboric acid solution in water (Aldrich) was added to the $TOTA^+$ solutions (100 mL).

A Lambda Physik EMG102 xenon-chloride laser was used to irradiate the samples, with excitation wavelength at $\lambda = 308$ nm. The laser pulse had duration of ca. 10 ns and an energy output of approximately 0.8 J/pulse.

The monitoring system consisted of a xenon lamp (VIX-150 UV) and a lamp pulser (custom built). The xenon lamp generated a continuum of light from 200 nm to 900 nm and was pulsed for ca. 4 ms, temporarily increasing the current, to generate intense monitoring light. UniBlitz (model D122) shutters controlled the passage of monitoring light through the sample and the excitation beam from the laser. The detection system consisted of a monochromator (2035 McPherson, 0.35-meter scanning monochromator) and a photomultiplier (PHM 1P28). A Stanford DG353 four channel digital delay/pulse generator was used to trigger the laser and the xenon lamp. The analog signal from the photomultiplier was sent to a LeCroy 940 dual 350

MHz oscilloscope where it was digitised and sent to a PC where the data was processed in a custom made program.

The phosphorescence spectrum of $TOTA^+$ was recorded at 77K on a LS 50B Perkin-Elmer luminescence spectrometer using the phosphorescence accessory. $TOTA^+$ was dissolved in ethanol to a concentration of 1.3×10^{-4} M and measured in a 2 mm quartz tube submerged in liquid nitrogen.

3.3 Results

3.3.1 Absorption and fluorescence parameters

$TOTA^+$ tetrafluoroborate is an organic salt, which is stable as a solid and when dissolved in acetonitrile and water. Figure 3.2 shows the absorption and fluorescence emission spectra of $TOTA^+$ dissolved in acetonitrile.

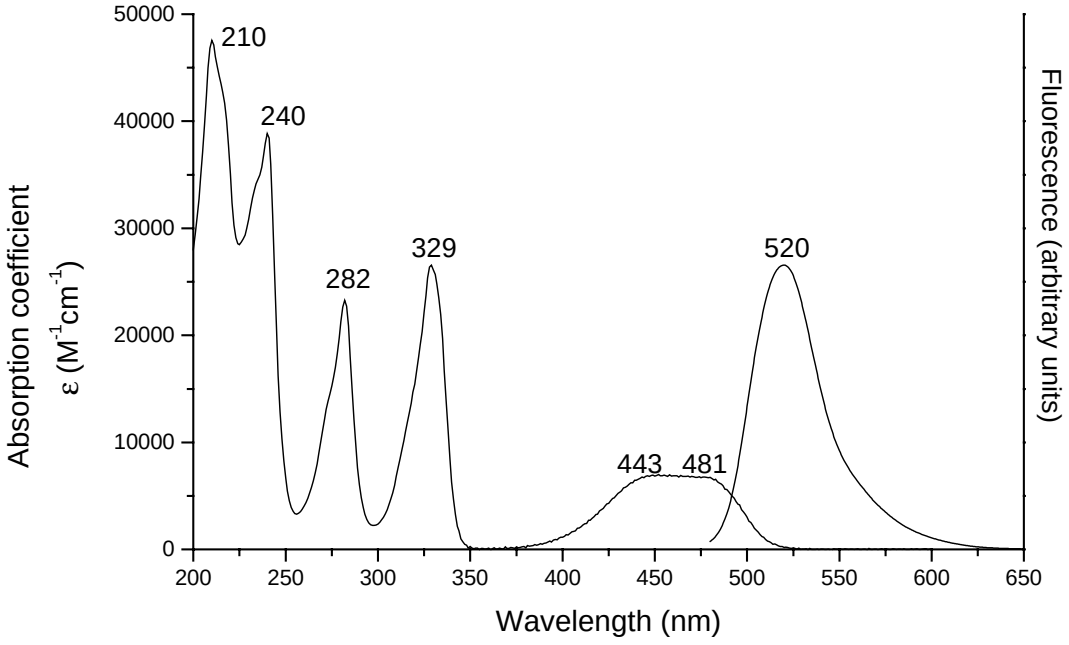

Figure 3.2. Absorption and uncorrected fluorescence spectra of $TOTA^+$ in acetonitrile.

A broad absorption band is observed at 400-500 nm, which can be attributed to two close lying transitions. The fluorescence emission spectrum has a maximum at 520 nm. It is broad and devoid of vibrational structure. The mirror image rule was applied to the corrected absorption and fluorescence spectra in order to elucidate the two transition bands. [5;6] The results are depicted in figure 3.3 (see next page). The modified absorption bands (ε(υ')/υ') are given as a full line. The modified/normalised fluorescence intensity (F(υ')/(υ')^3 (dashed line)) gives

maximum at υ'_{max} = 19157 cm^{-1} (522 nm). The two curves intersect at υ_o = 20000 cm^{-1} giving the mirror image (dotted line) with a maximum at υ'_{max} = 20771 cm^{-1} (481 nm). When the fluorescence mirror image is subtracted from the total absorption it discloses the second absorption band (dot-dashed line) with a maximum at υ'_{max} = 22523 cm^{-1} (443 nm). The intersection between the normalised fluorescence and the absorption spectra reveals the energy of the lowest excited singlet state as $E(S_1)$ = 20000 cm^{-1} = 239 kJ/mol.

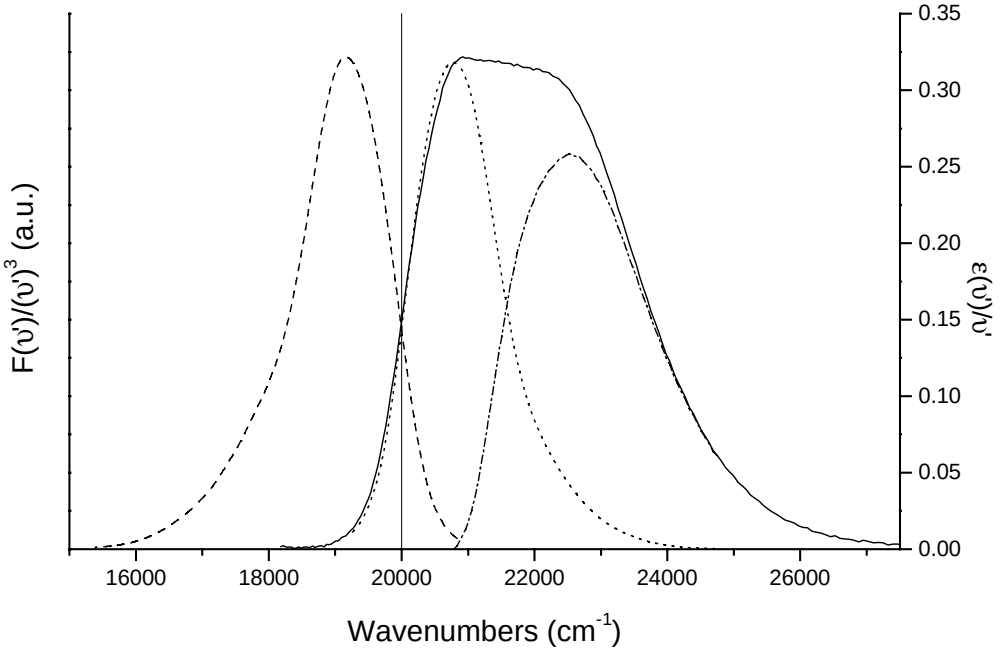

Figure 3.3. Modified long wavelength absorption band (full line) and modified/normalised fluorescence intensity (dashed line). The intersect gives the mirror image (dotted line). The total absorption subtracted by the fluorescence mirror image gives the second absorption band (dot-dashed line).

An unusual profile is observed when the absorption spectrum is traced from the visible region into the ultraviolet in figure 3.2. While there is almost no absorption at 350-360 nm, four very narrow peaks are observed at 330, 282, 241, and 210 nm, respectively, the width at half height being only 2200 cm^{-1} and 1800 cm^{-1} for

the first two transitions mentioned. The overlap of the bands at 241 and 210 nm prevents estimation of their width. The numeric $TOTA^+$ absorption data are collected in table 3.1 along with the data on the X^+ and PX^+ carbocations.

Table 3.1. The absorption wavelength λ_{max} (nm) and molar absorption coefficient ε ($M^{-1}cm^{-1}$) of $TOTA^+$ and 9-phenyl xanthylium (PX^+) in acetonitrile and xanthylium (X^+) carbocation in 1:1 (v/v) acetonitrile: trifluoroacetic acid at room temperature.

$TOTA^+$ [a]		PX^+ [b]		X^+ [c]	
λ_{max}	ε	λ_{max}	ε	λ_{max}	ε
481	6600	446	4900	434	1750
443	6700	X	X	X	X
329	26600	372	29400	372	32700
282	23300	285	small	X	X
240	38900	260	38700	254	35100

[a] This work,
[b] Taken from ref. [7] and [8]
[c] Taken from ref. [9]

The observed (τ_{fl}) and radiative (τ_{fl}^o) fluorescence lifetimes are compiled in table 3.2 together with the fluorescence quantum yield (ϕ_{fl}) of $TOTA^+$ in argon purged acetonitrile and water along with the data on the X^+ and PX^+ carbocations.

Table 3.2. The fluorescence lifetime (τ_{fl}), fluorescence quantum yield (ϕ_{fl}) and fluorescence maximum (λ_{max}) of $TOTA^+$ in argon purged water and acetonitrile, 9-phenyl xanthylium (PX^+) in acetonitrile and xanthylium (X^+) in 1:1 (v/v) acetonitrile: trifluoroacetic acid at room temperature. The radiative lifetime ($\tau°$) is deduced from $\tau° = \tau_{fl} / \phi_{fl}$.

carbocations	τ_{fl} (ns)	ϕ_{fl}	$\tau°$ (ns)	λ_{max} (nm)
$TOTA^+$ (acetonitrile)	14.6 [a]	0.53 [b]	27.5	522
$TOTA^+$ (water)	11.7 [a]	0.52 [b]	22.5	522
X^+ [c]	17.5	0.16	109	533
PX^+ [d]	27.6	0.47	58.7	535

[a] Estimated error ± 5%
[b] Estimated error ±10%
[c] taken from reference [9]
[d] taken from reference [7] and [10]

3.3.2 Dynamic quenching of the excited singlet state

The fluorescence of $TOTA^+$ is quenched by the ten aromatic molecules in acetonitrile. These molecules are pyrene, anthracene, phenanthrene, *trans*-stilbene, triphenylene, naphthalene, biphenyl, durene, mesitylene and *p*-xylene, respectively. This quenching was evident from the gradual shortening of the observed lifetime (figure 3.4) and from the progressive decrease in steady-state emission intensity (figure 3.5, in the next section) with increasing quencher concentration.

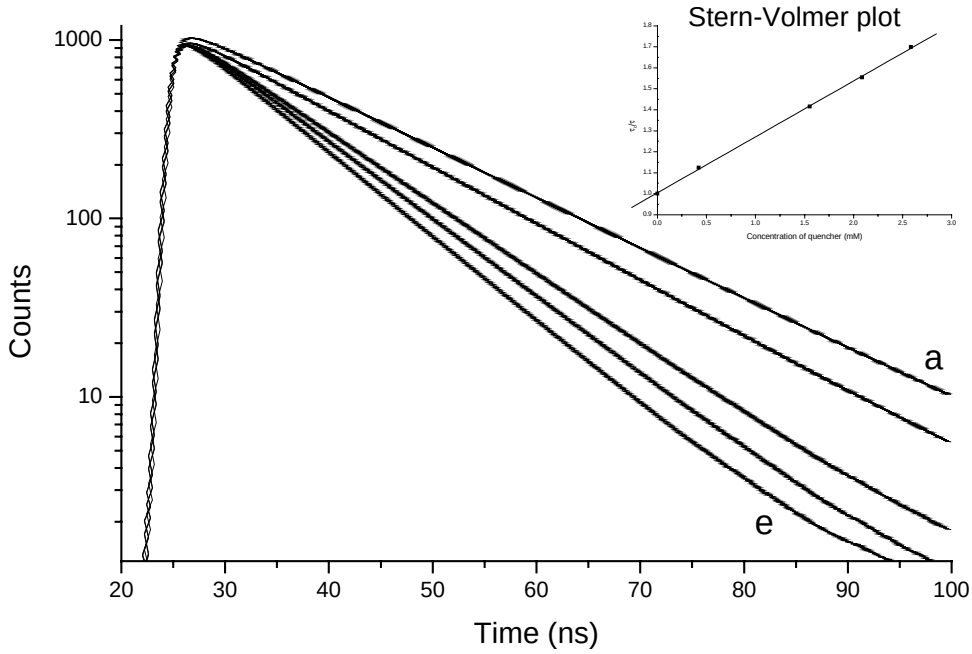

Figure 3.4. Quenching of the fluorescence lifetime of $TOTA^+$ (1×10^{-5} M in acetonitrile) upon gradual addition of *trans*-stilbene (a) 0.0, (b) 0.42, (c) 1.55, (d) 2.09, (e) 2.59 mM. The inset depicts the Stern-Volmer plot of the quenching.

The quenching rate constants were obtained from the slopes of the Stern-Volmer plots for the time-resolved measurements according to equation 1 ("TR" refers to Time Resolved):

$$\tau_{fl}/\tau' = 1 + k_q^{TR}\tau_{fl}[Q] \qquad 1)$$

The time resolved quenching constants for the aromatics are compiled in table 3.3 below along with the data on the X^+ and PX^+ carbocations.

Table 3.3. Bimolecular rate constants for the quenching of the lifetime (k_q^{TR}) fluorescence of $TOTA^+$ in argon purged acetonitrile and the quenching of the steady state (k_q^{SS}) fluorescence of 9-phenyl xanthylium (PX^+) in acetonitrile and xanthylium (X^+) in 1:1 (v/v) acetonitrile: trifluoroacetic acid at room temperature. The half wave-oxidation ($E_{½}^{ox}$) and ionisation (I_p) potentials of the aromatic donors are also given.

	$TOTA^+$	PX^+ [b]	X^+ [c]		
Quencher	k_q^{TR}, [a] 10^9 M^{-1} s^{-1}	k_q^{SS}, 10^9 $M^{-1}s^{-1}$	k_q^{SS}, 10^9 $M^{-1}s^{-1}$	$E_{½}^{ox}$, [d] V	I_p, [e] eV
p-xylene	9.28	14	20	1.56	8.44
Mesitylene	9.04	13	x	1.55	8.41
Durene	11.6	18	x	1.29	8.04
Biphenyl	12.5	16	19	1.48	7.95
Naphthalene	12.3	18	23	1.33	8.14
Phenanthrene	15.5	x	x	1.23	7.86
Pyrene	15.7	x	x	0.86	7.41
Anthracene	14.8	26	28	0.84	7.45
Triphenylene	13.5	x	x	1.22	7.84
t-stilbene	16.9	x	x	1.22[f]	7.7

[a] Estimated error, ± 5%
[b,c] Taken from ref. [9], [11] and [12]
[d] Versus Ag / 0.1 N Ag^+ in acetonitrile (taken from ref.[13])
[e] taken from ref. [13]
[f] Versus saturated calomel reference electrode in acetic acid. Converted according ref. [14]

Plots of the dynamic (k_q^{TR}) quenching rate versus the ionisation (I_p) and half wave oxidation ($E_{½}^{ox}$) potentials of the electron donors reveal a linear correlation shown in figures 3.6 and 3.7 (see next pages).

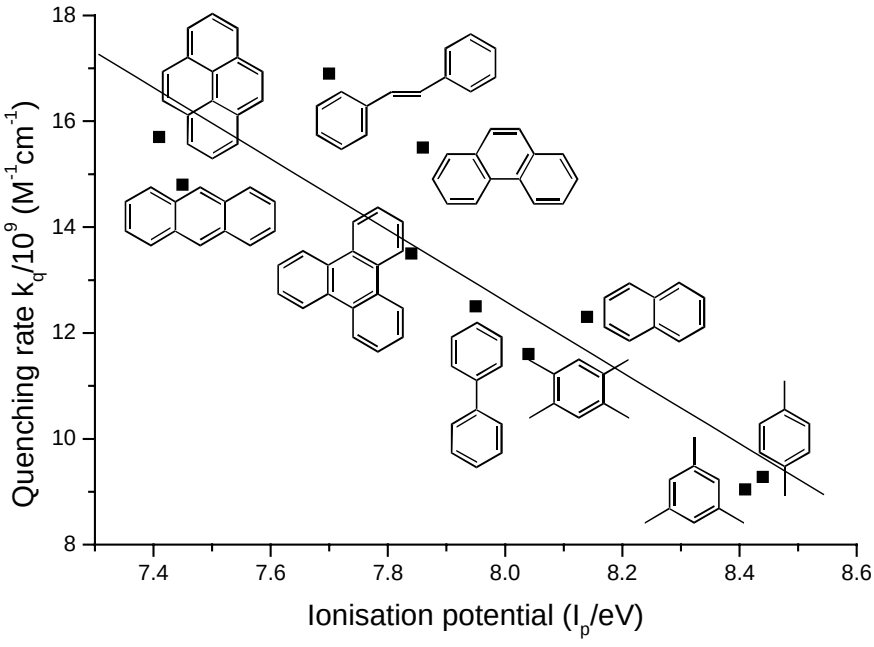

Figure 3.6. The dynamic quenching rates versus ionisation potentials of the quenchers.

A general increase in quenching rate correlates with the enhanced ability of the quencher to donate an electron implying that the quenching process is a single electron transfer from the aromatic donors to $TOTA^+$ (S_1).

The data points for the quenching rates are quite scattered when either plotted against ionisation or oxidation potentials. The methylated benzene derivatives all show somewhat lower quenching rates compared to their planar counterparts. Biphenyl exhibits a faster rate than average when plotted against the oxidation potential but slower for the ionisation potential. Both *trans*-stilbene and phenanthrene display higher quenching rates than expected from their potentials.

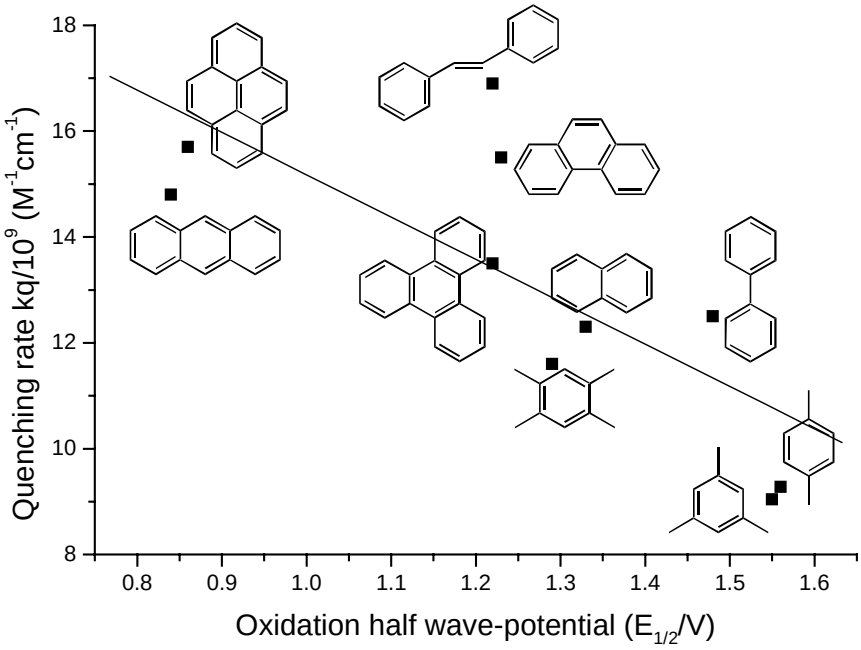

Figure 3.7. The dynamic quenching rates versus half-wave oxidation potentials of the quenchers.

The reduction potential of $TOTA^+$ has been reported as $E_{½}^{red}$ = -0.385 V (*vers.* SCE).[15;16] Using the $E_{½}^{red}$ value for $TOTA^+$ and applying the Rehm-Weller[17;18] equation (see equation 2), the free energy of electron transfer (ΔG_{ET}) from the donors to the $TOTA^+$ singlet was estimated. The coulombic energy term of the Rehm-Weller equation was not included since no new charges were formed.

$$\Delta G_{ET} = 96.53\left[E_{½}^{ox}/D - E_{½}^{red}/A^{\cdot-}\right] - E_{oo} \qquad 2)$$

Based on the $E_{½}^{ox}$ values from table 3.3, ΔG_{ET} values ranging from ca. – 125 kJ/mol (for *p*-xylene) to –210 kJ/mol (for anthracene) were obtained. Even with the most negative ΔG_{ET} values, no indication of the Marcus'[19-21] inverted region was observed.

3.3.3 Steady – state fluorescence quenching

The Stern – Volmer plots derived from the steady state fluorescence intensity measurements all curve upward as illustrated in the inset of figure 3.5.

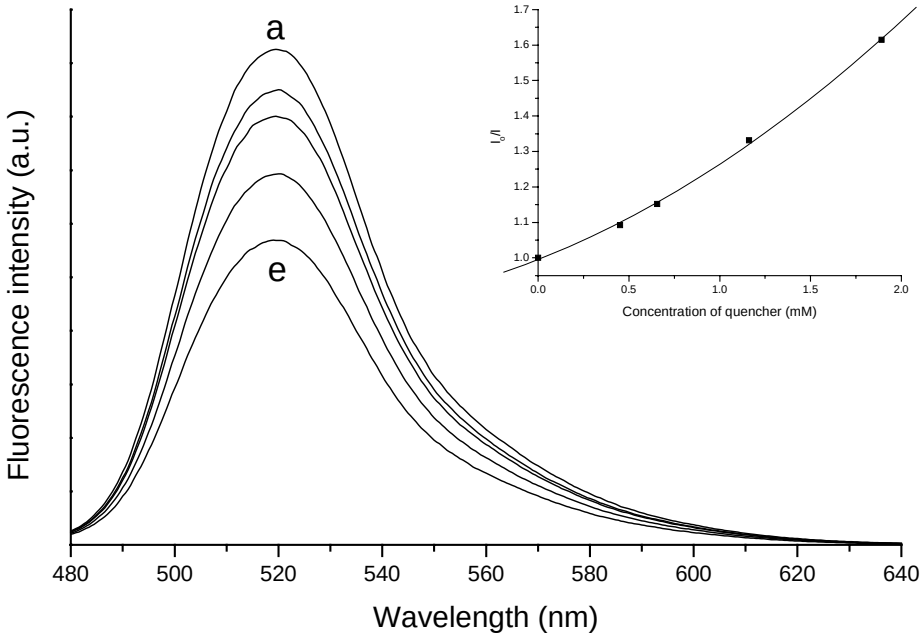

Figure 3.5. Quenching of $TOTA^+$ steady state fluorescence (1×10^{-5} M in acetonitrile) upon gradual addition (a) 0.0, (b) 0.45, (c) 0.66, (d) 1.16, (e) 1.89 mM of pyrene. The inset depicts the Stern-Volmer plot of the quenching.

This curvature clearly indicates formation of a ground state complex between the aromatic donor and $TOTA^+$.[22] The association constants (K_S) for the ground state complex formation is defined by equation 3 ([Q] standing for quencher concentration):

$$TOTA^+ + Q \Leftrightarrow TOTA^+ - Q$$

$$K_S = \frac{\left[TOTA^+ - Q\right]}{\left[TOTA^+\right]\left[Q\right]} \qquad 3)$$

Total concentration of $TOTA^+$ in the solution is:

$$\left[TOTA^+\right]_O = \left[TOTA^+\right] + \left[TOTA^+ - Q\right] \quad 4)$$

Substitution into equation 3 yields:

$$K_S = \frac{\left[TOTA^+\right]_O - \left[TOTA^+\right]}{\left[TOTA^+\right]\left[Q\right]} = \frac{\left[TOTA^+\right]_O}{\left[TOTA^+\right]\left[Q\right]} - \frac{1}{\left[Q\right]} \quad 5)$$

By substituting $TOTA^+$ concentration with its fluorescence intensities, and rearranging equation 5 yields:

$$I_O / I = 1 + K_S\left[Q\right] \quad 6)$$

I_o being the intensity of the fluorescence with no quencher present and I when there is, which is valid if fluorescence quenching can be attributed to ground state complex formation only. When both dynamic and static quenching take place both must be represented in the modified Stern-Volmer equation[22]:

$$I_O / I = \left(1 + K_D\left[Q\right]\right)\left(1 + K_S\left[Q\right]\right) \quad 7)$$

The K_S constants for the ground state complex formation were estimated by fitting the data to equation 7. The K_D constant is known from the time resolved measurements as $K_D = k_q^{TR} \tau_{fl}$. The K_S constants obtained are shown in table 3.4.

The constants range from very small for mesitylene to 560 M^{-1} for pyrene. It is apparent that the methylated benzene derivatives and biphenyl form the weakest ground state complexes while the larger fused ring aromatic systems interact more strongly with the exception of phenanthrene. *Trans*-stilbene also has a substantial ground state complexation.

Table 3.4. The ground state complex constants for $TOTA^+$ and the π-doners (quenchers).

π-doner	K_s [a] (M^{-1})
p-xylene	15
Mesitylene	5
Durene	10
Biphenyl	15
Naphthalene	40
Phenanthrene	90
Pyrene	560
Anthracene	470
Triphenylene	325
t-stilbene	250

[a] Estimated error, ± 15%

3.3.4 Quenching by oxygen and BF_4^-

The quenching rate of oxygen was estimated as $k_q^{oxygen} = 4\ (\pm\ 1)\ *10^9\ M^{-1}s^{-1}$ from both the steady state and the time resolved measurements. The fluorescence intensity of $TOTA^+$ was only slightly reduced (5 %) by saturation with $NaBF_4$.

3.3.5 Absorption spectra and ground state complexes

In order to observe ground state complex formation by absorption spectroscopy, tandem optical quartz cells were used (see experimental section). A spectrum was measured with $TOTA^+$ and the π-donor dissolved in separate compartments. Then the solutions were mixed and a spectrum measured again. This allows one to observe $TOTA^+$ and the π-donor with the same optical density (provided complex formation is not extensive) and therefore any change in intensity or shifts are a result of charge transfer complex formation. It was necessary to utilise saturated or very highly concentrated solutions of the π-donors and high concentration of $TOTA^+$ in order to observe a change after mixing.

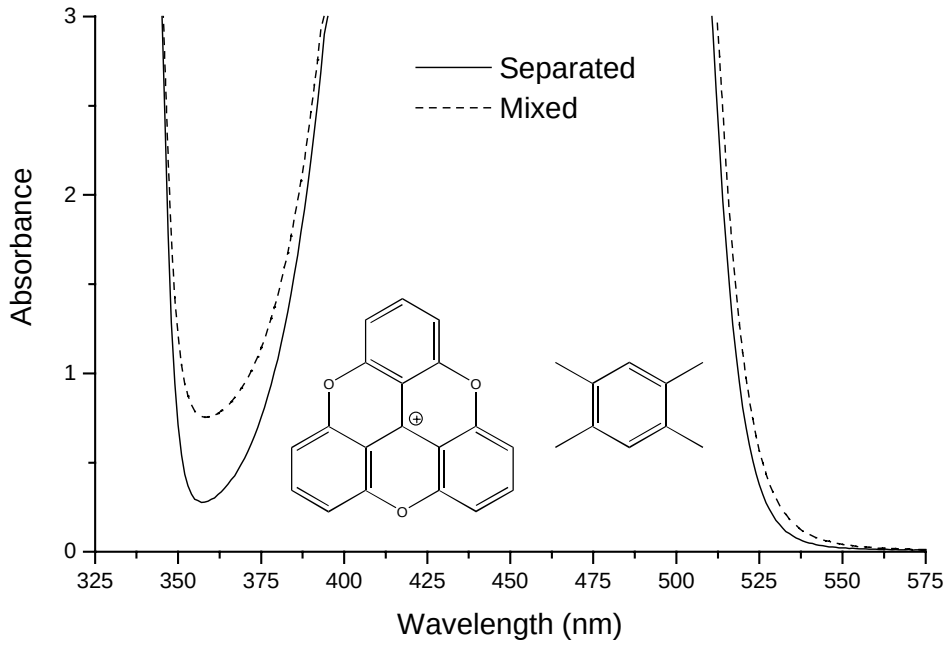

Figure 3.8. Electronic absorption spectra of $TOTA^+$ and durene in acetonitrile recorded in a 1×1 cm quartz tandem cell, first in separated compartments and then mixed together.

In general, apparent broadenings were observed in the absorption spectra for the transitions at 443 and 481 nm. Furthermore, a distinct increase in absorption in

the 350-400 nm region appeared for all the π-donors as shown in figure 3.8 for durene.

Pyrene and anthracene differed qualitatively from the other quenchers: The yellow solution of $TOTA^+$ in acetonitrile turned brown red upon addition of those donors in high concentration. The colour change is due to the appearance of a distinct long-wavelength charge-transfer band as shown in figure 3.9 for anthracene. In the solvent used in this study, no emission, which could be attributed to an exciplex was observed at longer wavelengths.

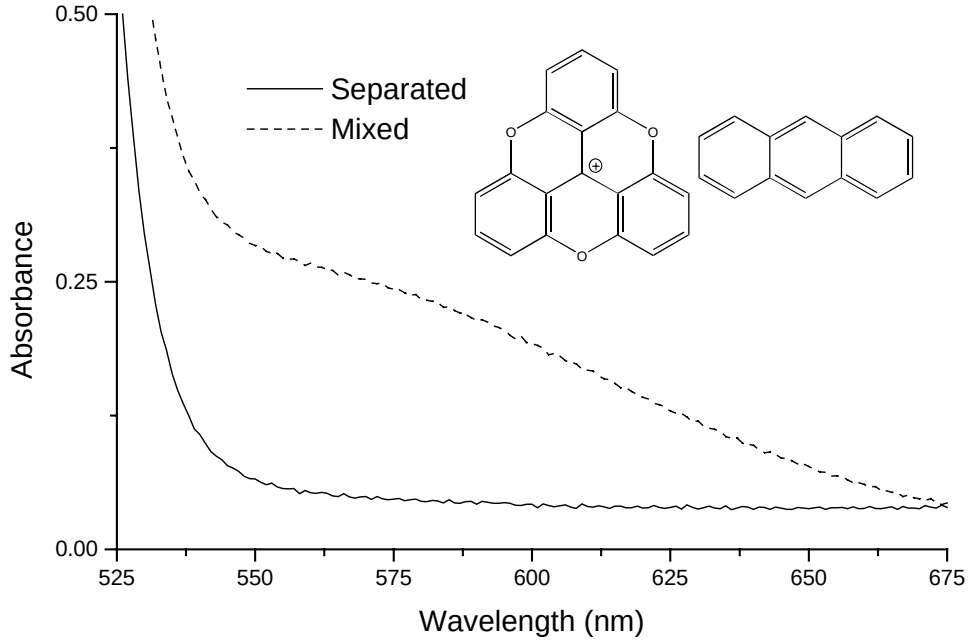

Figure 3.9. Electronic absorption spectra of $TOTA^+$ and anthracene solvated in acetonitrile, recorded in a 1×1 cm quartz tandem cell, first in separated compartments and then mixed together.

3.3.6 The triplet excited state of $TOTA^+$

The lifetimes and the transient absorption spectra of the triplet state of $TOTA^+$ were measured in water and acetonitrile. The lifetimes are shown in table 3.5. It is apparent that oxygen quenches the transient species and it is therefore concluded that the triplet state of $TOTA^+$ is indeed observed.

Table 3.5. The triplet lifetimes of $TOTA^+$ in microseconds (μs) determined with laser flash photolysis for argon purged and air saturated solutions.

	Ar purged	Air saturated	
	$\tau(\mu s)^a$	$\tau(\mu s)^a$	$[O_2]^b / 10^{-3}$
Water	34.2	3.33	0.29
Acetonitrile	23.2	0.66	1.9

[a] Estimated error ±10%
[b] From ref. [23]

The triplet state in water has longer lifetime than in acetonitrile. The transient spectrum of $TOTA^+$ in water is shown in figure 3.10. It has two maxima at λ_{max} = 360 nm and λ_{max} = 600 nm, respectively.

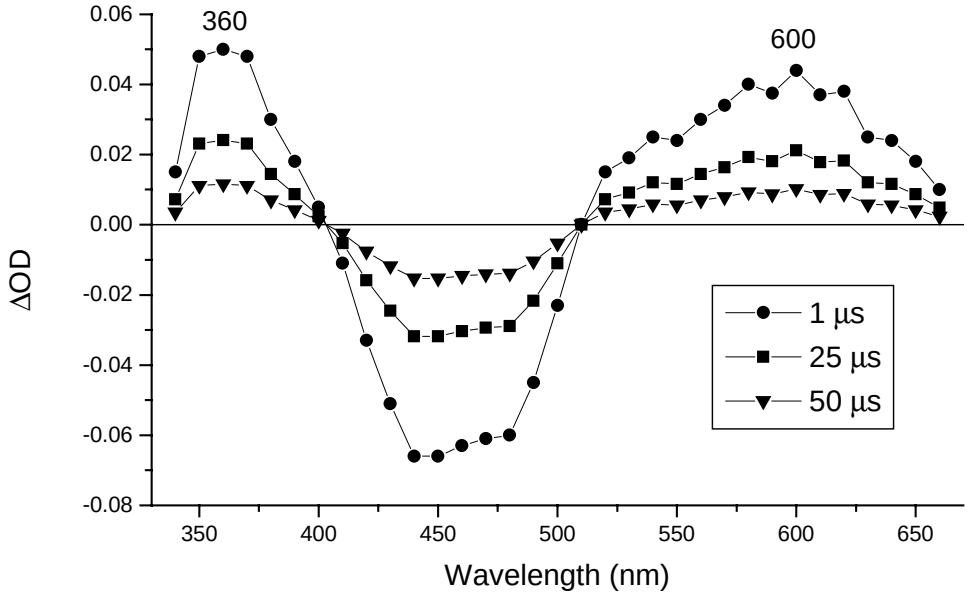

Figure 3.10. Transient absorption spectrum of $TOTA^+$ recorded 1 μs (circle), 25 μs (rectangle) and 50 μs (triangle) after 308 nm laser photolysis of a deoxygenated 1×10^{-4} M solution of $TOTA^+$ in water.

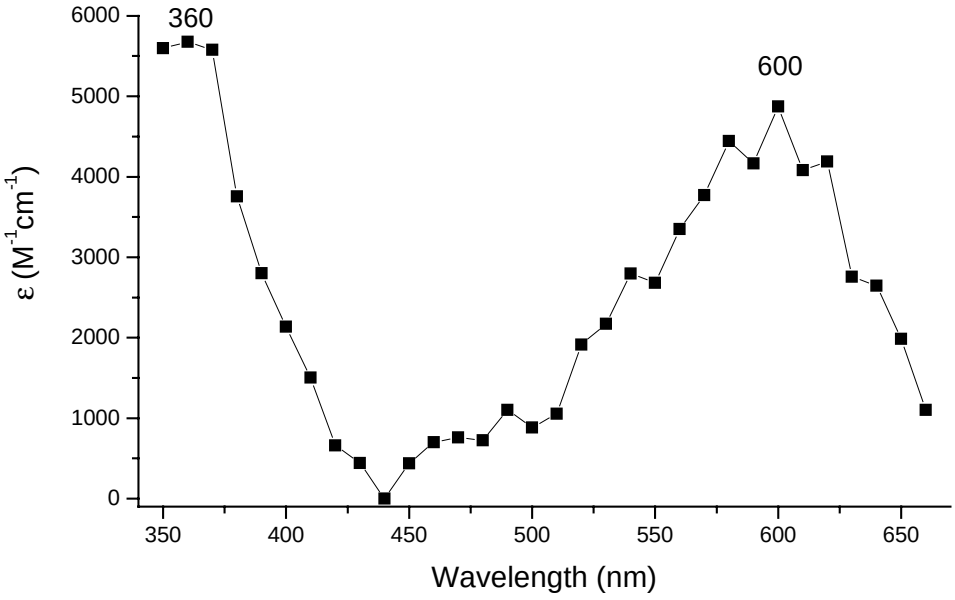

Figure 3.11. Absorption spectrum of the lowest triplet state of $TOTA^+$ calculated from the transient absorption spectrum and the ground state singlet absorption spectrum in water with the singlet depletion method.[24]

The triplet-triplet absorption spectrum was calculated from the transient spectrum and the ground state singlet spectrum of $TOTA^+$ with the singlet depletion method.[24] The calculated spectrum is depicted in figure 3.11. The singlet depletion method utilises the change in OD (optical density) where the triplet state does not absorb. It was assumed that the triplet state does not absorb at 440 nm and equation 8 was applied in order to estimate the concentration of the transient.

$$\Delta OD_{440} = -\varepsilon_S \left[{}^3M \right] l \qquad 8)$$

ε_S is the extinction coefficient for the singlet ground state, $[^3M]$ is the concentration of the triplet and l is the path length of the monitoring beam. The flash induced concentration of triplet in water was estimated $[^3M] = 4.5\times10^{-6}$ M and triplet-triplet extinction coefficients for all of the measured wavelengths were calculated using equation 9:

$$\Delta OD = \varepsilon_T \left[{}^3M \right] l - \varepsilon_S \left[{}^3M \right] l \qquad 9)$$

The quantum yield of intersystem crossing (ISC) can be deduced from equation 10 since the triplet and ground state [M] concentrations are known. It is assumed that all of the ground state $TOTA^+$ molecules are excited into the lowest singlet state by the laser flash.

$$\phi_{ISC} = \frac{\left[{}^3M \right]}{\left[M \right]} \qquad 10)$$

The predicted ISC is $\phi_{ISC} \geq 0.07$. The ϕ_{ISC} value is a minimal because if not all to the ground state is excited, the concentration of the singlet excited state is less than assumed and $\phi_{ISC\ is}$ larger.

Moderate phosphorescence emission was observed at 77 K in ethanol and the spectrum is shown in figure 3.12. Vibrational fine structure is observed with maxima at λ_{max} = 548 nm and at 572 nm. The fluorescence (λ_{max} = 520 nm) and phosphorescence maxima are only separated by 2000 cm^{-1} which is an unusually small value for $\pi\pi^*$ transition states as well as the appearance of fine structure which is more inherent to $n\pi^*$ transitions. The phosphorescence lifetime was determined as τ_{pho} = 2.75 s. The triplet energy is deduced as 52 Kcal/mol.

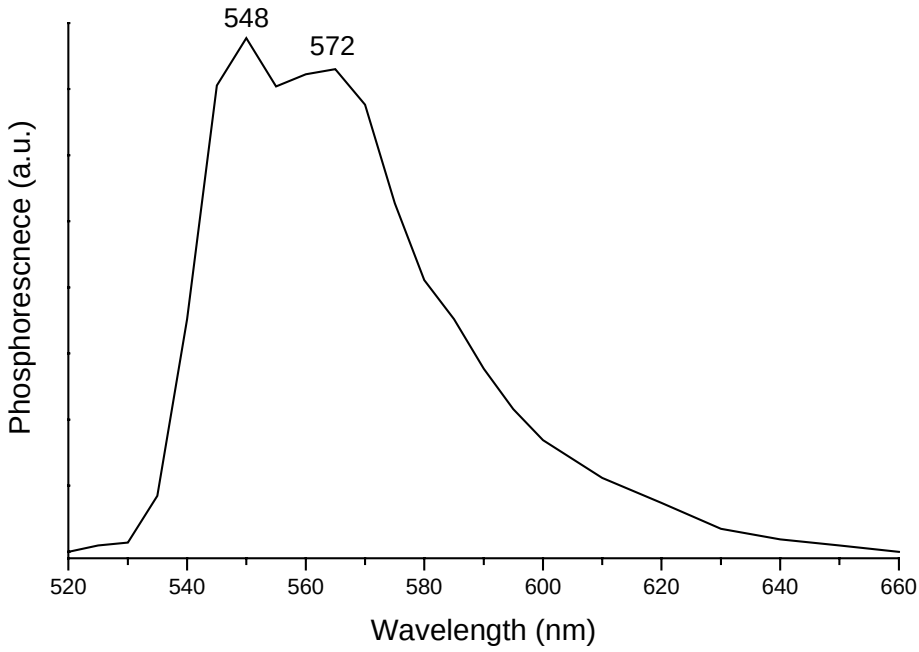

Figure 3.12. The phosphorescence spectrum of $TOTA^+$ in ethanol at 77 K.

3.4 Discussion

3.4.1 Absorption spectra

In general, a good mirror-image relationship is observed between the fluorescence and the low-energy absorption band in the xanthylium carbocations.[25] Samanta *et al.*[9] derived the radiative lifetime for X^+ and PX^+ by means of the Strickler-Berg formula[26] and found excellent agreement with the experimental values obtained from the fluorescence lifetimes and quantum yields. This result implies that only one electronic transition is contributing to the low energy absorption band of the xanthylium carbocations.

In contrast, the data on $TOTA^+$ shows that the long wavelength absorption band consists of two close lying electronic transitions (figure 3.3). $TOTA^+$ has D_{3h} symmetry and these (π,π*)-transitions connect the ground state (A_1') with doubly degenerate E' states. The same relative positioning of the energy levels is found among symmetrically substituted triphenylmethyl carbocations with D_3 symmetry. [1] Thus, the long wavelength absorption band of the parent triphenylmethyl carbocation features two doubly degenerate transitions like $TOTA^+$. [27] The absorption coefficient of the long wavelength band of $TOTA^+$ is ca. 25 % larger than that of PX^+ (table 3.1), which is due to the more extended conjugation and planarity introduced by the two additional bridging oxygen atoms in $TOTA^+$. The PX^+ and X^+ carbocations also display intense bands at 372 nm (table 3.1). The corresponding transition is found at 329 nm in the spectrum of $TOTA^+$. The absorption coefficients of this band are roughly the same for all three, but the $TOTA^+$ band is much narrower. A small peak appears at 285 nm for the PX^+ cation corresponding to the band at 282 nm for $TOTA^+$ but no transition is observed at that region for the X^+ carbocation. The PX^+ and X^+ carbocations display intense bands at 260 and 254 nm, respectively, which

corresponds with the peak at 240 nm for $TOTA^+$. The absorption coefficients are similar for all three. These differences of the intensity and location of the transitions between $TOTA^+$ and the xanthylium carbocations in the UV region are most likely due to the rigidity of the $TOTA^+$ molecular framework.

3.4.2 Fluorescence

The photophysical properties of the xanthylium carbocations have been investigated in a number of polar solvents.[7-9;11;28-30]Since the excited singlet states of these carbocations are very sensitive to nucleophilic attack, several values have been reported for their emission parameters. The numbers quoted in table 3.2 for compounds X^+ and PX^+ were obtained in 1:1 (v/v) acetonitrile: trifluoroacetic acid and dry acetonitrile, respectively.[7-9] In contrast, the excited singlet state of $TOTA^+$ seems only marginally affected by nucleophiles since roughly the same lifetimes were observed in water and acetonitrile.

Introduction of the 9-phenyl substitute on the xanthylium chromophore increases the fluorescence lifetime and quantum yield substantially of the PX^+ carbocation (see table 3.2). The emission takes place from the xanthylium moiety since the fluorescence maxima are found at practically the same wavelength for the X^+ and PX^+ carbocations. It has been estimated by *semi*-empirical calculations that the 9-phenyl ring is twisted 59° out of planarity of the xanthylium moiety. [31]

The $TOTA^+$ carbocation is more planar and rigid compared to the xantylium systems, which is reflected in the more efficient non-radiative deactivation of the latter. The Stoke shift of $TOTA^+$ (1633 cm^{-1}) is smaller compared to its xanthylium counterparts (4227 cm^{-1} for X^+ and 3720 cm^{-1} for PX^+). This implies that the singlet excited state of $TOTA^+$ is structurally similar to its ground state.

3.4.3 Electron transfer quenching

Boyd and coworkers [7;25;28;30;31] observed quenching by water, alcohols and ethers of the fluorescence from a range of substituted 9-phenylxanthylium and 9-phenylthioxanthylium carbocations. The quenching rate varied more than the expected reduction potential of the cations indicating a quenching mechanism not relying on single electron transfer. Consequently, it was concluded, that the quenching action was initiated by a nucleophilic attack.

Single electron transfer has been demonstrated to occur as a general phenomenon between excited carbocations and aromatics or alkenes.[25] In particular, Samantha *et al.* [9;11;32] and Azarani *et al.* [12] have determined the quenching rates for a series of aromatic donors of the fluorescence from X^+ and PX^+ by means of steady state Stern-Volmer kinetics. No ground state complex formation was observed between the carbocations and the aromatic quenchers. Relevant values for the quenching rate constants (k_q^{SS}) obtained by Samantha *et al.* are listed in table 3.3. There is an obvious trend towards increasing reactivity with decreasing oxidation potential of the aromatic, which suggests that electron transfer is involved for the X^+ and PX^+ carbocations.[12]

The same dependence on donor oxidation potential is observed in the case of $TOTA^+$, signifying a transfer of a single electron from the quencher to the singlet excited state of the carbocation. Comparing the three carbocations (in table 3.3), fluorescence quenching is seen to be slower for $TOTA^+$ relative to PX^+, which again is slower than the rate constant for X^+ (in the diffusion controlled limit).

The reduction potentials of the carbocations are decisive in determining the quenching rate of the fluorescence. The potential for $TOTA^+$ is $E_{½}^{red} = -0.385$ V (*vers.* SCE)[15;16]. The reduction potentials for the PX^+ and X^+ carbocations are $E_{1/2}^{red} =$

–0.374 V and $E_{1/2}^{red}$ = –0.352 V (*vers.* Ag/Ag^+ glassy carbon electrode), respectively.[33] After conversion form the Ag/Ag^+ electrode to the SCE standard electrode (by subtracting 0.29V[14]) the PX^+ and X^+ carbocations acquire the values of $E_{1/2}^{red}$ = –0.664 V and $E_{1/2}^{red}$ = –0.642 V, respectively. It is apparent that the PX^+ and X^+ carbocations are almost twice as reductive as $TOTA^+$. Also, the singlet energies of the PX^+ and X^+ carbocations (~250 kJ/mol[16;25]) are roughly 10 kJ/mol higher than for $TOTA^+$ (239 kJ/mol). Hence, the more efficient electron transfer from the aromatics to the excited PX^+ and X^+ carbocations compared to $TOTA^+$. It has been postulated that the lower quenching rate of the PX^+ compared to its X^+ counterpart is due to the steric hindrance of the phenyl moiety of the PX^+ carbocation, since they have almost the same $E_{½}^{red}$ and singlet energies.[9]

Considerable scatter is observed in figures 3.6 and 3.7 when the quenching rates are plotted against the ionisation and oxidation potentials. Partially, this spread can be due to the intrinsic properties of the methods by which ionisation (I_p) and oxidation ($E_{½}^{ox}$) potentials are determined. The physical surroundings of the oxidant differ quite substantially between the methods. The ionisation potential is determined in vacuum, where it is bombarded with electrons. The oxidation potential is determined in solution where the molecule interacts with the metal surface of an electrode. The circumstances, on the molecular level, for both of these methods differ from the situation of a contact complex between a donor and an acceptor molecules in solution.

Biphenyl is either faster or slower than average depending on the potential used (see figures 3.6 and 3.7). Biphenyl is non-planar [34;35] in the gas phase and therefore it can appear slower when plotted against ionisation potentials due to sterical hindering. Biphenyl is also nonplanar in the liquid phase [10] but it can be speculated

that, when it approaches an oxidising electrode, it is forced to assume a more planar configuration before delivering its electron and therefore it acts more like a planer molecule.

Another reason for this scattering could be that the oxidation and ionisation potentials only reflect the exothermic factor of the formation of the geminate contact pair, excluding any effect the activation energy might have on the electron transfer rate, which is described by the Marcus theory. [21] Also the extent of the avoided crossing of the relevant potential energy surfaces is not accounted for, i.e., the extent of the interaction of the surfaces. This effect is described by the preexponential factors in equation 11[32]:

$$k_{et} = \upsilon_N \kappa \exp\left[-\Delta G^{\neq} / RT\right] \quad 11)$$

The first preexponential term (υ_N) is the nuclear frequency factor of the reaction. For aromatic donors, it is dominated by the high frequency inner modes of the C-C stretching of aromatic donors.[36] The unusually high quenching rate of *trans*-stilbene can eventually be attributed to the fact that *trans*-stilbene is not a rigid fused ring system like the other donors, even though it is planar[32], and therefore should have more low vibrational modes available, facilitating its more effective avoided crossing. The second preexponential term (κ) is the transmission coefficient of the reaction. It is related to the perturbation hamiltonian (H_{AB}) coupling of the initial and final states of the system ($k \propto H_{AB}$). The value of H_{AB} depends on the overlap between the electronic wavefunctions of the donor and acceptor, which decreases exponentially with distance.[36] This can be the cause for the lower quenching rate of the methylated

benzene derivatives. The methyl groups are sterically hindering, causing a larger average distance between the donor and acceptor, compared to the planar molecules.

Gould, Farid and co-workers[37;38] studied back electron transfer to methyl substituted aromatic donors from cyanoanthracene derivatives, which had gained an electron from the aromatic derivatives when electronically excited. They found considerable less scattering in their data, when radical cations of methyl substituted benzene acceptors where fitted separately with acceptors based on naphthalene, biphenyl and phenanthrene. Unfortunately the available data for $TOTA^+$ is not extensive enough in order to follow the procedure of Gould and Farid.

Even with the most negative ΔG_{ET} values, there was no indication of the Marcus inverted region.[21 19;20] Neither was this expected, since inverted behaviour is generally not observed for emission quenching in fluid solutions at ambient temperatures [18] unless electron transfer takes place within a supermolecule [39-41]or a close radical ion pair.[37]

3.4.4 Quenching by oxygen

An interesting general feature of carbocationic fluorescence is its resistance to quenching by oxygen ($k_q^{oxygen} \sim 10^9\ M^{-1}s^{-1}$),[7;9;12;29] which is slower by an order of magnitude compared to the rates observed for quenching by aromatic hydrocarbons[42;43] and diphenylpolyenes.[44] This behaviour illustrates that molecular oxygen and a carbocation are both electron acceptors and no electron transfer reaction can occur. The excited singlet state of $TOTA^+$ is more reactive ($k_q^{oxygen} = 4\ (\pm\ 1) \times 10^9\ M^{-1}s^{-1}$) than of the other carbocations due to the more efficiently delocalised positive charge in $TOTA^+$. In addition to electron transfer, molecular oxygen can quench *via* paramagnetically induced intersystem crossing.[5]

3.4.5 Formation of ground state complexes

Dynamic quenching results from collisional encounters between the fluorophore and quencher. Non-collisional or static quenching can occur when a non-fluorescent complex is formed between the fluorophore and quencher in their ground states. In case of $TOTA^+$, the Stern-Volmer plots of the steady state quenching revealed an upward curvature, signifying static quenching due to ground state complex formation.[22] Among those, pyrene and anthracene have the highest affinity towards ground state complex formation, which also is manifested by the appearance of a distinct charge transfer bands in their absorption spectra (figure 3.8). Aside from reductive power, structural properties of the donors also play a role in their ability to form ground state complexes. The individual nodal structures of the HOMOs and LUMOs involved determine the orbital overlap in each case. Furthermore, the polymethylated benzenes are hindered by the substituents. For biphenyl, a planar configuration and unhindered interaction with the $TOTA^+$ π-system is hampered by repulsion among its *ortho*-hydrogens.

Samantha *et al.*[12] were unable to detect any ground state complexation between a range of aromatic donors and X^+ or PX^+ even at the highest concentrations obtainable. Other carbocations, like the tropylium system, [45] are able to form charge transfer complexes with aromatic electron donors.

3.4.6 The excited triplet state of $TOTA^+$

Johnston and Wong[46;47] have characterised the triplet excited state of PX^+ by both luminescence and transient absorption. The excitation of the cation in TFE or in ethanol/H^+ glasses at 77 K shows weak phosphorescence at 600 nm, giving an estimate of its triplet energy at ~48 Kcal/mol. The triplet – triplet absorption, obtained by laser flash photolysis (355 nm) in TFE, shows $\lambda_{max} \leq 300$ nm and decays over several microseconds (5 – 15 μs). The triplet is efficiently quenched by molecular oxygen.

Cozens and colleagues also generated the triplet excited PX^+ carbocation via 355 nm laser excitation formed by adsorption of the alcohol within acid zeolites. [48] Transient spectra recorded 1 μs after laser excitation show reflectance near 300 nm previously assigned to the triplet cation[46;47], as well as a strong band at 520 – 570 nm. Both bands were formed promptly after the laser pulse, decay at the same rate in nitrogen purged samples. The bands are similarly quenched by oxygen leading to the conclusion that both bands are due to the presence of the triplet transient carbocation.[48] In addition, the measured lifetime for the triplet PX^+ carbocation within the zeolite is approximately 50 μs.

The phosphorescence maximum of $TOTA^+$ is blue shifted 1580 cm^{-1} compared to PX^+. This shift is considerably smaller for the singlet state (539 cm^{-1}) for the same molecules.

The lifetime of the triplet state of $TOTA^+$ in solution at room temperature (23.5 μs in acetonitrile) is significantly higher than its counterpart for PX^+(5 – 15 μs). $TOTA^+$ is a planar rigid molecule while PX^+ has more flexibility and has therefore

more opportunities to deactivate via vibrational relaxation. On the other hand, when PX^+ is adsorbed to a surface, the triplet lifetime becomes twice as long as $TOTA^+$'s. This is due to deactivation of vibrational modes of PX^+ when stuck to a surface, hindering its deactivation.

The transient triplet – triplet absorption spectra of $TOTA^+$ has a transition at 360 nm and PX^+ in solution at the 300 nm region. $TOTA^+$ also exhibits a transition at 600 nm but no transition is observed at the longer wavelength for PX^+ unless is absorbed to a surface of a zeolite. When adsorbed to a surface PX^+ could take more planar configuration, like $TOTA^+$. This observation suggests that the phenyl moiety be close to perpendicular to the xanthyl chromophore, inhibiting interaction between the π-systems of the groups. Both the transitions in the transient triplet – triplet absorption spectrum for $TOTA^+$ are red shifted compared to the ones for PX^+. $TOTA^+$ has more singlet absorption states (see table 3.1), particularly S_2 where PX^+ has none compared to $TOTA^+$. The S_2 in $TOTA^+$ has its corresponding T_2 where none exists for PX^+. Hence, the triplet states lie relatively closer together in $TOTA^+$ than for PX^+.

3.5 Conclusions

The fluorescence and phosphorescence emission properties of $TOTA^+$ resemble those of the xanthenium carbocations. The $TOTA^+$ fluorescence is quenched by several aromatics *via* an electron transfer mechanism, the excited carbocation acting as an electron acceptor. The dynamic quenching rate constant (k_q^{TR}) correlates roughly with the half-wave oxidation potential of the quenchers. Electron transfer occurs in the normal region of the Marcus theory. Upward curvature is observed for the Stern-Volmer plots derived from the steady state quenching measurements. This is due to fractional ground state complex formation between $TOTA^+$ and the electron donors. Pyrene and anthracene demonstrated the best ability to form ground state complexes with $TOTA^+$. Both give rise to distinct charge transfer absorption bands.

3.6 Reference List

1) Duxbury, D.F. *Chem.Rev.* **1993**, *93*, 381-433.

2) Faldt, A.; Krebs, F.C.; Thorup, N. *J.Chem.Soc., Perkin Trans.2* **1997**, 2219-2227.

3) Williams, A.T.R.; Winfield, S.A. *Analyst* **1983**, *108*, 1067-1071.

4) Stewart, W.W. *Cell* **1978**, *14*, 741-759.

5) Birks, J.B. *PHOTOPHYSICS OF AROMATIC MOLECULES*; Wiley-Interscience: London, 1970; pp 84-87.

6) Lakowicz, J.R. *Principles of Fluorescence Spectroscopy*; Plenum Press: New York, 1983; pp 7.

7) Valentino, M.R.; Boyd, M.K. *J.Org.Chem.* **1993**, *58*, 5826-5831.

8) Bedleck, J.M.; Valentino, M.R.; Boyd, M.K. *J.Photochem.Photobio.A.* **1996**, *94*, 7-13.

9) Samanta, A.; Gopidas, K.R.; Das, P.K. *J.Phys.Chem.* **1993**, *97*, 1583-1588.

10) Suzuki, H. *Bull.Chem.Soc.Jpn.* **1959**, *32*, 1340-1350.

11) Samanta, A.; Gopidas, K.R.; Das, P.K. *Chem.Phys.Lett.* **1990**, *167*, 165-169.

12) Azarani, A.; Berinstain, A.B.; Johnston, L.J.; Kazanis, S. *J.Photochem.Photobiol.A.* **1991**, *57*, 175-189.

13) Siegerman, H.In *Technique of Electroorganic Synthesis*; Weinberg, N.L., Ed.; John Wiley & sons: New York, 1975; pp 667-842.

14) Kavarnos, G.J.*Fundamentals of Photoinduced Electron Transfer*; VCH Publishers, Inc.: New York, 1993; pp 35.

15) Nemcová, I.; Nemec, I. *J.Electroanal.Chem.* **1971**, *30*, 506-510.

16) Nemcová, I.; Nemec, I. *Chem.zvesti.* **1972**, *26*, 115-125.

17) Rehm, D.; Weller, A. *Ber.Bunsen-Ges.Phys.Chem.* **1969**, *73*, 834-839.

18) Rehm, D.; Weller, A. *Isr.J.Chem.* **1970**, *8*, 259-271.

19) Marcus.R.A. *J.Chem.Phys.* **1965**, *43*, 679-683.

20) Marcus.R.A. *Ann.Rev.Phys.Chem.* **1964**, *15*, 155-196.

21) Marcus.R.A.; Sutin, N. *Biochimica et Biophysica Acta* **1985**, *811*, 265-322.

22) Lakowics, J.R. *Principles of Fluorescence Spectroscopy*; Plenum Press: New York, 1983; pp 257-301.

23) Murov, S.L.; Carmichael, I.; Hug, G.L.*Handbook of Photochemistry*; Marcel Dekker, Inc.: New York, 1993; pp 264-265.

24) Carmichael, I.; Hug, G.L. *J.Phys.Chem.Ref.Data* **1986**, *15*, 1-32.

25) Boyd, M.K. *Organic Photochemistry*; Ramamurthy, V., Schanze, K.S., Eds.; Marcel Dekker: New York, 1997; pp 147-186.

26) Strickler, S.J.; Berg, R.A. *J.Phys.Chem.* **1962**, *37*, 814-822.

27) Dekkers, H.P.J.M.; Kielman-van, E.C.M. *Mol.Phys.* **1976**, *31*, 1001-1019.

28) Boyd, M.K.; Lai, H.Y.; Yates, K. *J.Am.Chem.Soc.* **1991**, *113*, 7294-7300.

29) Minto, R.E.; Das, P.K. *J.Am.Chem.Soc.* **1989**, *111*, 8858-8866.

30) Valentino, M.R.; Boyd, M.K. *J.Photocem.Potobio.A:chem.* **1997**, *89*, 7-12.

31) Boyd, M.K. *Spectrum* **1998**, *11*, 6-10.

32) Görner, H.; Kuhn, H.J. *Cis-Trans Photoisomerization of Stilbenes and Stilbene-Like Molecules*; Wiley & Sons, Inc.: Chichester, 1995; pp 1-117.

33) Arnett, E.M.; Amarnath, K.; Harvey, N.G.; Cheng, J. *J.Am.Chem.Soc.* **1990**, *112*, 344-355.

34) Bastiansen, O.; Trætteberg, M. *Tetrahedron.* **1962**, *17*, 147-154.

35) Karle, I.L.; Brockway, L.O. *J.Am.Chem.Soc.* **1944**, *66*, 1974-1979.

36) Balzani, V.; Scandola, F. *Supramolecular Photochemistry*; Ellis Horwood: New York, 1991;

37) Gould, I.R.; Ege, D.; Moser, J.E.; Farid, S. *J.Am.Chem.Soc.* **1990**, *112*, 4290-4301.

38) Gould, I.R.; Farid, S. *Acc.Chem.Res.* **1996**, *29*, 522-528.

39) Chen, P.; Duesing, R.; Tapolsky, G.; Meyer, T.J. *J.Am.Chem.Soc.* **1989**, *111*, 8305-8306.

40) Wasielewski, M.R.; Niemczyk, M.P.; Svec, W.A.; Pewitt, E.B. *J.Am.Chem.Soc.* **1985**, *107*, 1080-1082.

41) Miller, J.R. *J.Am.Chem.Soc.* **1984**, *106*, 3047-3049.

42) Patterson, L.K.; Porter, G.; Topp, M.R. *Chem.Phys.Lett.* **1970**, *7*, 612-614.

43) Brown, R.G.; Phillips, D. *Trans.Faraday.Soc.2* **1974**, *70*, 630-636.

44) Chattopadhyay, S.K.; Das, P.K.; Hug, G.L. *J.Am.Chem.Soc.* **1982**, *104*, 4507-4514.

45) Takahashi, Y.; Sankararaman, S.; Kochi, K. *J.Am.Chem.Soc.* **1989**, *111*, 2954-2697.

46) Johnston, L.J.; Wong, D.F. *J.Phys.Chem.* **1993**, *97*, 1589-1595.

47) Johnston, L.J.; Wong, D.F. *Can.J.Chem.* **1992**, *70*, 280-282.

48) Cozens, F.L.; Garcia, H.; Scaiano, J.C. *Langmuir* **1994**, *10*, 2246-2249.

Chapter 4

Studies of the TOTA$^+$-DNA Complex and its Photocleavage Properties

4.1 Introduction

More than 35 years ago it was suggested that the DNA's internal tunnel of stacked π-orbitals might serve as a conduit for electrical charge, i.e., a molecular wire.[1] This idea was practically forgotten until about seven years ago, when Barton et al. [2] published a paper reporting evidence that DNA might indeed be wirelike. She used two metallointercalators, serving as a acceptor – donor pair, which were tethered to the opposite ends of a 15 – base pair DNA duplex (~40 Å) and observed the effective quenching of the luminescence of the acceptor. Following this publication many studies have followed but unfortunately the results vary dramatically, asserting either that DNA is indeed a wire or that DNA is practically a insulator.[3-6]

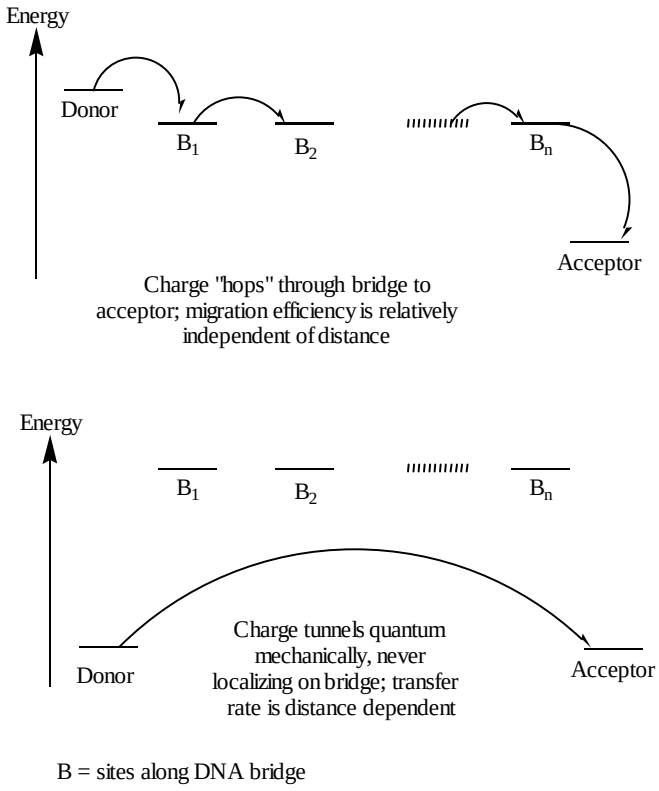

Figure 4.1. Possible mechanisms for electron migration through DNA.

The question of how and how fast electrical charge wanders through DNA has significant bearing on issues such as DNA damage, genetic detection and microelectronics.

Two scenarios have received most of the attention of the researchers: the tunnelling and hopping mechanisms. These are illustrated in figure 4.1 (previous page). The tunnelling mechanism is sometimes termed "π-way" and is based on the assumption that a charge can quantum mechanically "tunnel" its way through a stack of the π-orbitals of the base pairs in a DNA helix, newer localising on a base pair. The hopping mechanism falls under the Marcus theory [7-9] where the charge is expected to hop from base to base. Neither of those theories adequately describes the experimental and theoretical results obtained in laboratories around the globe.

Recently, Gary B. Schuster at Georgia Technical Institute came up with another possible mechanism, which is dubbed "phonon-assisted polaron-like hopping." [10] This mechanism is illustrated in figure 4.2.

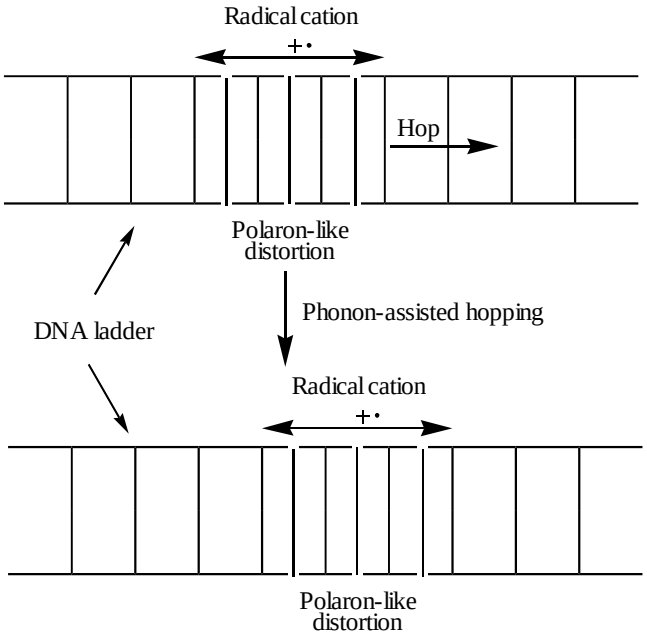

Figure 4.2. Phonon-assisted polaron-like hopping: A radical cation charge is delocalised within a polaron-like distortion in duplex DNA. In this case, the polaron "hops" to the right with a step size of one DNA base pair.

Deriving his model from those of synthetic conducting polymers, he suggested that when a positive charge enters the DNA strand, it causes a localised distortions in the bases around it. The charge itself is delocalised through the group of distorted bases. This distortion, known as a polaron, changes the overlap of orbitals, allowing the charge to hop through the strand. The polaron shifts through the strand to accompany the hopping charge. The phonons are thermal motions of a DNA helix in solution.

Intercalation sites in the DNA duplex are created by thermal motions by accompanying concerted changes in backbone torsional angles.[11] At 25 °C and 0.1 M salt concentration association of simple intercalators with nucleic acid duplexes occurs with a half life less than one millisecond and creation of an intercalation site must therefore occur within that time period.[12] Figure 4.3 illustrates space filling models of a dimer DNA with ethidium intercalated between the base pairs. [13]

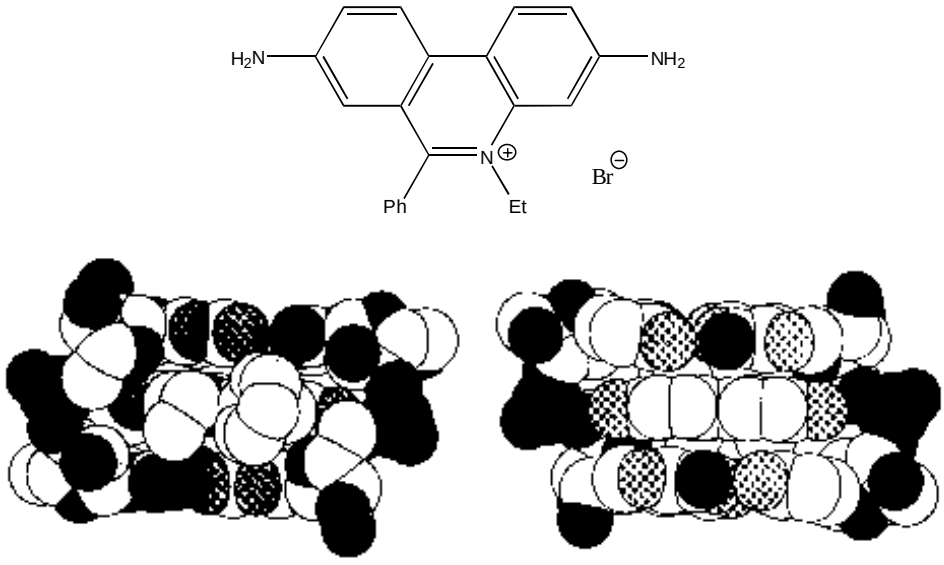

Figure 4.3. The molecular structure of ethidium bromide and space filling models of it intercalated between two base pairs. The ethidium – DNA complex is shown from the minor groove (left) and the major groove (right). The hydrogen atoms have been deleted to assist in visualisation of the system. The atom colouring is as follows: Carbon and hydrogen – white, nitrogen – light grey, oxygen – dark grey, and phosphorous – black.

The main purpose of the following project was to utilise the high symmetry (D_{3h}) and equal charge distribution of the $TOTA^+$ carbocation in order to create an artificial polaron by intercalating it between the base pairs and to investigate how the charge distorts the structure of the DNA helix. It is possible to crystallise short segments of DNA with ligands, which is an excellent method to explore the structural parameters of ligand-DNA interactions. My part of the project was to establish the binding mechanism of $TOTA^+$ to DNA, i.e., does it intercalate between the base pairs or does it sit in the minor or the major grooves on DNA? This is no straightforward procedure and various experimental methods were employed. $TOTA^+$ was also shown to be a photonuclease and its properties were studied.

4.2 Experimental

Trioxatriangulenium (4,8,12-trioxadibenzo[*cd,mn*]pyrenylium) tetrafluoroborate was synthesized according to the procedure published by Faldt et al.[14]

4.2.1 Determination of Binding Constant

A buffer solution of $TOTA^+$ (25 μM in a 1.0 cm cuvette) was titrated with a concentrated calf thymus DNA (CT-DNA) solution. The calf thymus was purchased from Sigma (St. Louis, MO). The optical density of the solution at 330 nm was measured initially and after each addition on a Hewlett Packard 8453 absorption spectrometer. The change in optical density was used to calculate α, the fraction of bound $TOTA^+$ to CT-DNA. [15]

4.2.2 Fluorescence Quenching

Solutions of 25 μM $TOTA^+$ and CT-DNA (from 0 to 150 μM) were prepared in pH = 7 phosphate buffer and transferred to a standard 1×1 cm optical quartz cell. The spectra were obtained on a Spex 1681 Fluorolog emission spectrometer in the normal 90º configuration. The samples were irradiated at 450 nm and the fluorescence emission spectra were recorded from 475 to 650 nm at room temperature.

4.2.3 Viscosity Experiments

Viscosity experiments used a Cannon - Ubbelohbe semi-micro dilution viscometer (series #75, Cannon Instrument Company), immersed in a thermostated water bath maintained at 33.3 ºC (±0.02 ºC). Titration with $TOTA^+$ was performed by the addition of small volumes of concentrated stock solution (5×10^{-4} M) to the DNA sample in the viscometer. Solutions in the viscometer were mixed by bubbling air through the solution. DNA concentration of approximately 2.4×10^{-4} M (in base pairs) of sonicated calf thymus DNA (average 800 base pair long) was used. $TOTA^+$ and DNA solutions were buffered with PIPES (pH = 7, piperazine-N, N'-bis-2-ethanesulfonic acid, Sigma chemicals). Relative viscosities for DNA in either presence or absence of ligand were calculated from the relation:

$$\eta = \frac{(t - t_O)}{t_O}$$

Where t is the observed flow time of the DNA containing solution, and t_o is the flow time of the buffer alone. Viscosity data were plotted as $(\eta/\eta_o)^{1/3}$ versus the binding ratio r, according to the theory of Cohen and Eisenberg. [16]

4.2.4 Induced Circular Dichroism (CD) Spectroscopy

CD spectra were recorded on a JASCO J-270 instrument. A 10 cm path length cylindrical quartz cell was used. Buffer solutions of $TOTA^+$ (30 μM in 10 mM sodium phosphate, pH = 7) and sonicated CT-DNA (40 μM, base pairs) were used. Spectra were recorded from 550 to 200 nm.

4.2.5 Melting Point Temperatures of DNA (T_m)

5 μM solutions of two complementary 12-mer oligonucleotides (5'-AAA GGT AAC GCG-3' and 5'-CGC GTT ACC TTT-3') in 10 mM phosphate buffer were prepared, pH = 7. Melting curves were obtained by monitoring the absorbance at 260 nm and the temperature was ramped from 20 to 90 °C at the rate of 0.5 °C/min. Curves obtained from heating and cooling ramps gave identical curves. Cary 1E UV-Visible spectrophotometer with temperature controller (Varian analytical instruments) was used in order to obtain the melting curves.

4.2.6 Competition Dialysis Experiment

Multiple disposable dialysis units, each containing 0.5 mL of a 75 μM solution of the DNA samples, are listed in table 4.1, were placed in a beaker containing 200 mL of a 1 μM $TOTA^+$ solution. The system was allowed to equilibrate for 24 hours with continuos stirring. After equilibrium dialysis was attained, the amount of $TOTA^+$ bound to the DNA was measured by the absorbance of $TOTA^+$ after it has been extracted from the DNA samples with a SDS (sodium dodecyl sulfate) solution. Since all of the DNA samples are in equilibrium with the same $TOTA^+$ concentration, the amount of bound ligand is directly proportional to the association constant of $TOTA^+$ bound to a particular structure. This process is described in detail by J. Ren and J.B. Chairs. [17]

4.2.7 Phosphorescence Quenching

Solution of 10 μM $TOTA^+$ in 1:1 (v/v) 10 mM pH = 7 phosphate buffer : ethylene glycol was prepared and transferred to a cylindrical glass phosphorescence tube, which was then submerged in an optical Dewar flask containing liquid nitrogen. The samples were irradiated at 450 nm and the fluorescence / phosphorescence emission spectra were recorded from 475 to 650 nm. Two samples containing $TOTA^+$ and DNA was prepared as described above but 10 and 50 μM calf thymus DNA (base pairs) were added. A blank sample containing only the ethylene glycol / buffer was used to record the base line, which was subtracted form the spectra in order to eliminate light scattering effects. The fluorescence, which was observed, was removed electronically from the phosphorescence spectrum. The spectra were run on a Spex 1681 Fluorolog emission spectrometer with front face configuration.

4.2.8 Cleavage Analysis by Radiolabelling and PAGE

A 12-mer oligonucleotide (5'-AAA GGT AAC GCG-3') was radiolabelled at the 5'-OH using (γ-^{32}P) ATP and bacterial T_4 polynucleotide kinase. [18] Radiolabelled DNA was purified on a 20% PAGE gel. Samples for irradiation were prepared by hybridising a mixture of cold and radiolabelled oligonucleotide (5μM) with 5 μM of the complementary strand and 10 μM $TOTA^+$ in phosphate buffer, pH = 7. Hybridisation was achieved by heating the samples at 90 ºC for 5 min and slowly cooling to room temperature. These samples were irradiated in microcentrifuge tubes in a Rayonet photoreactor containing eight lamps emitting at 350 nm (Southern New England Ultraviolet Company, Bransford, CT). After irradiation, the samples were precipitated with ethanol, dried and then treated with 90 ºC hot piperidine (1 M) for 15 min. After evaporation of the piperidine the samples (150 cpm) were separated by electrophoresis on 20% denaturing 19:1 acrylamide - bis(acrylamide) gel containing 7 M urea. Gels were dried and the cleavage was visualised by autoradiography.

4.3 Results

4.3.1 Equilibrium Binding Constant

Binding of $TOTA^+$ to calf thymus (CT) DNA was investigated by UV-Visible and fluorescence spectroscopies. The three lowest energy absorption bands for $TOTA^+$ exhibit pronounced hypochromic effect (40 - 50%) as well as a bathochromic shift (540 - 830 cm^{-1}) in the presence of CT-DNA. The bathochromic effect is most pronounced for the lowest energy absorption band at 480 nm and the hypochromisity is most effective for the transition at 330 nm as depicted in figure 4.4.

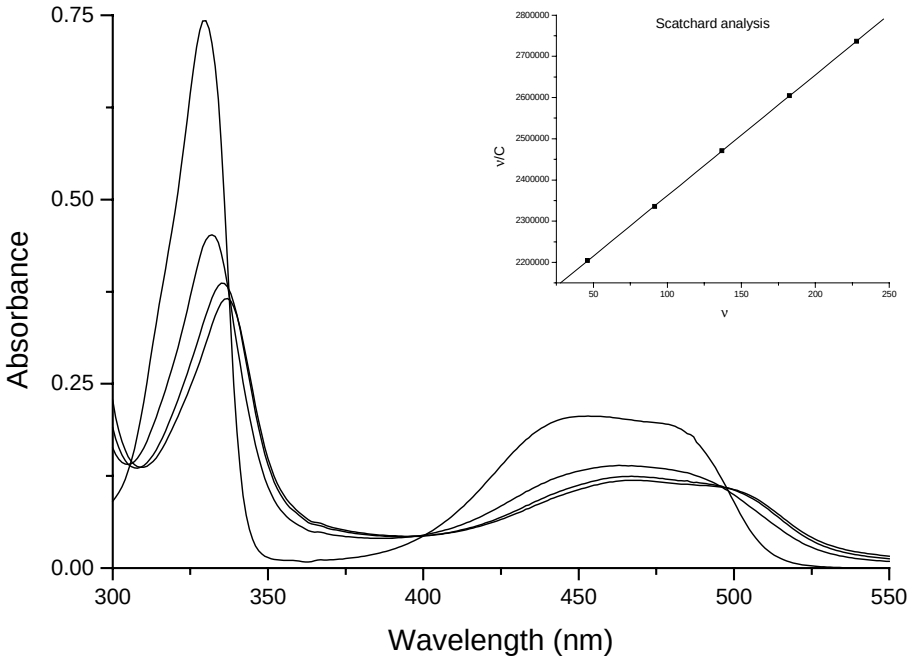

Figure 4.4. Absorption spectra for $TOTA^+$ binding to calf thymus DNA in 10 mM sodium phosphate buffer, pH = 7. Total $TOTA^+$ concentration for each spectrum is 50 μM. DNA base pair concentration (μM) for each spectrum (from left to right): 0.0, 41.5, 83.0 and 166.5. The inset depicts Scatchard analysis [19] of the data.

Equilibrium binding constant for $TOTA^+$ was measured by titrating a buffered solution (10 mM phosphate, pH = 7) with CT-DNA and monitoring the decrease in absorbance and red shift of the transition at 330 nm. Scatchard analysis [19] of the data

yields a linear fit as seen in the inset of figure 4.4, indicative of binding to DNA by a single mode. The resulting binding constant is $K_S = 4.1 \pm 0.3 \times 10^4\ M^{-1}$, which is defined by the equation 1:

$$TOTA^+ + DNA \Leftrightarrow TOTA^+ - DNA$$

$$K_S = \frac{\left[TOTA^+ - DNA\right]}{\left[TOTA^+\right]\left[DNA\right]} \qquad 1)$$

Where [DNA] is measured as mole base pairs per litre. The extinction coefficient of the $TOTA^+$ - DNA complex was estimated as 12200 $M^{-1}cm^{-1}$ at 336 nm. It is difficult to deduce the extinction coefficients for the two other transitions of $TOTA^+$, which also absorb in the visible range, due to their extensive overlap. The significant hypochromicity observed upon interaction of $TOTA^+$ and DNA can only be explained by extensive overlap of the π-orbitals of $TOTA^+$ and the nucleic acids. Neither the minor nor the major grooves on the DNA helix have enough π-orbitals in order for such an extensive overlap, which leads to the conclusion that $TOTA^+$ is intercalated between the base pairs of the DNA strand. The linearity of the Scatchard analysis[19] therefore indicates that only the intercalation process is active, excluding other forms of $TOTA^+$-DNA interactions.

$TOTA^+$ ground state binding to DNA was also investigated with fluorescence spectroscopy. The fluorescence of $TOTA^+$ was quenched in the presence of CT-DNA as depicted in figure 4.5 (see next page). Stern – Volmer plot of the quenching (see inset figure 4.5) revealed an upward turning curve, indicating that both dynamic and static quenching processes are active. [20] The static association constant (K_S) and the dynamic quenching constant (K_D) were deduced by fitting th data to the modified Stern – Volmer equation 2:

$$I_o/I = (1 + K_S[Q])(1 + K_D[Q]) \quad 2)$$

Where [Q] is the concentration of CT-DNA (quencher). The K_S was found to be $3.5 \pm 0.7 \times 10^4$ M^{-1}, which corresponds well with the binding constant, derived from absorption spectroscopy. The Stern – Volmer constant representing the dynamic quenching was $K_D = 4.5 \pm 0.7 \times 10^3$ M^{-1}. It is roughly an order of a magnitude lower than its static counterpart. The dynamic quenching constant is $k_q = 3.8 \times 10^{11}$ $M^{-1}s^{-1}$ derived from $K_D = \tau_o \times k_q$. The size of the CT-DNA fragments is ~800 base pairs and they are not homogenous. The K_D probably represents a collection of quenching constants since singlet state of $TOTA^+$ can most likely be quenched by intercalation, insertion in the major or the minor groove or simply by interacting with the exterior of DNA.

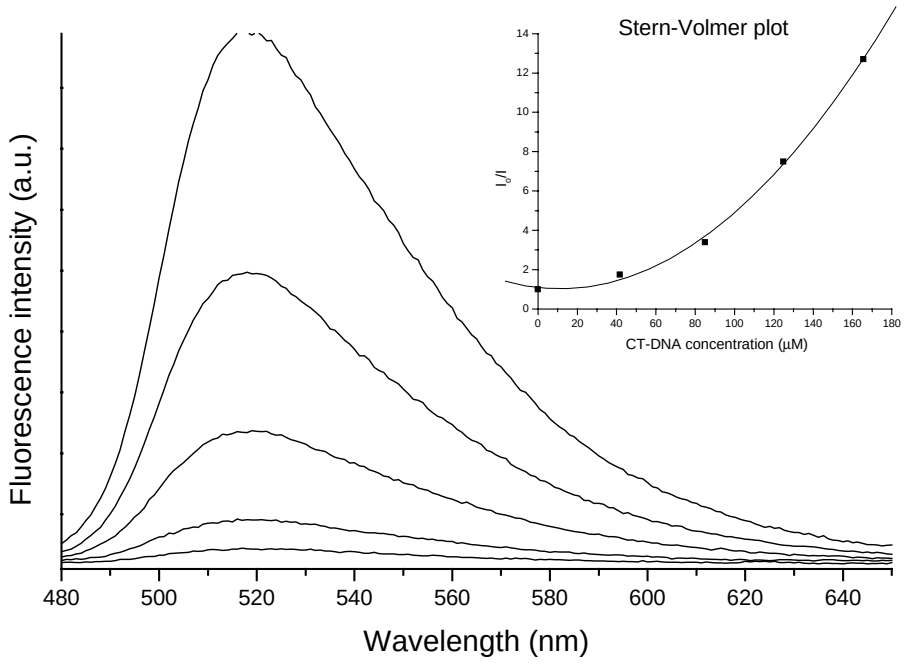

Figure 4.5. Quenching of the fluorescence of $TOTA^+$, binding to calf thymus DNA in 10 mM sodium phosphate buffer, pH = 7. Total $TOTA^+$ concentration for each spectrum is 25 μM. DNA base pair concentration (μM) for each spectrum is (from top to bottom): 0.0, 41.5, 83.2, 124.9, 166.5. The inset is the accompanying Stern-Volmer plot.

4.3.2 Geometry of the Intercalation Complex

Intercalation or groove binding of a molecule is distinguishable by viscosity changes. If a compound binds externally to the DNA double helix, only modest changes in viscosity are generally noted. The electrostatic attraction of positively charged cation to the negatively charged phosphate groups has little affect on the effective length of the polymer. Intercalation, on the other hand, proceeds by unwinding the double helix to accommodate a co-planar molecule that becomes inserted and stacked between the base pairs. This process results in an effective increase in the DNA contour length. The results obtained for viscosity measurements of DNA with increasing amounts of bound $TOTA^+$ are shown in figure 4.6. $TOTA^+$ increases the length of DNA, resulting in an increased viscosity, which underscores that $TOTA^+$ intercalates. The increase of sheared DNA helix length upon intercalation of $TOTA^+$ can be calculated from the experimental results of the intrinsic viscosities according to approximation 3 [12]:

$$\frac{L}{L_O} \cong \left[\frac{[\eta]}{[\eta_O]}\right] \frac{f(p)_O}{f(p)} \cong \left[\frac{[\eta]}{[\eta_O]}\right]^{1/3} \cong 1 + \beta r \qquad 3)$$

Where L/L_o is the helix length ratio in the presence (L) and absence (L_o) of the drug treatment; $[\eta]/[\eta_o]$ is the ratio of the intrinsic viscosity; $f(p)_o$ and $f(p)$ are functions of the DNA axial ratio p, which varies little for the large axial ratio values of linear DNA; r is the bound drug to DNA ratio; β is the slope when L/L_o or $([\eta]/[\eta_o])^{1/3}$ are plotted against r.

The intercalating model predicts that for a perfect monofunctional intercalator, the β value should be 1,[28] corresponding to the length increase of an intercalated dye

relative to that separating adjacent base pairs in the B structure of DNA (3.4 Å).[12] The value obtained for $TOTA^+$ is 1.3 Å.

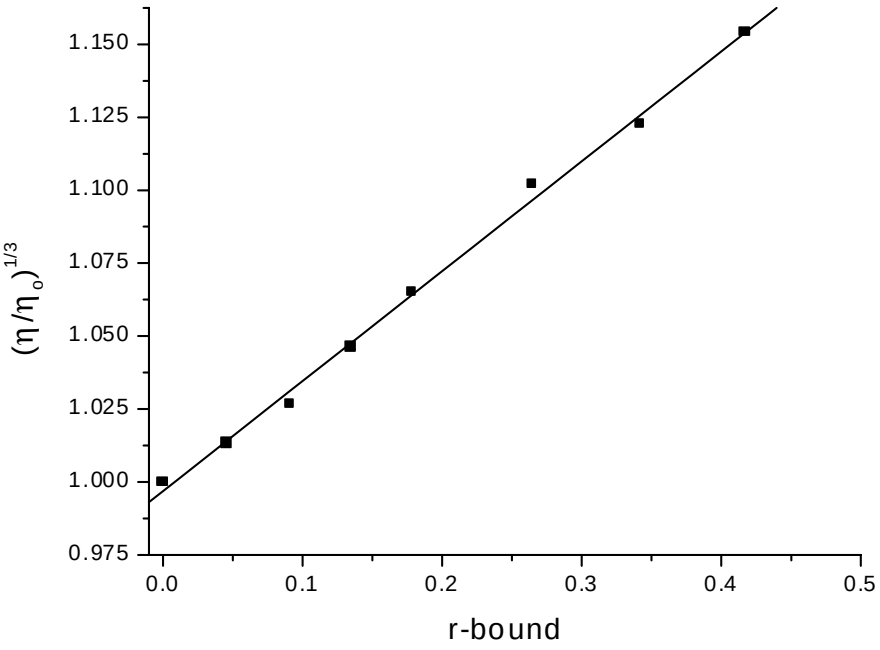

Figure 4.6. The relative specific viscosity of calf thymus DNA in the presence of $TOTA^+$ shown as a function of the binding ratio.

Information about the geometry of the DNA / $TOTA^+$ intercalation complex can be gleaned with the help of circular dichroism (CD) spectroscopy. Binding of an achiral molecule within a chiral environment, such as a right handed double helical DNA, can lead to induced optical activity for the bound species.[21] This is manifested in the appearance of a CD absorption band, assignable to the ligand but observed only in the presence of DNA. Provided the ligand absorbs light in a region where the DNA is transparent, it is straightforward to assign the new bands to the ligand. This is a known effect observed for a variety of DNA intercalators. [22] In the absence of DNA there are no observable CD bands for $TOTA^+$. However, $TOTA^+$ exhibits positive

induced CD bands upon binding to CT-DNA as shown in figure 4.7. The intensity if these induced bands is weak, indicating an intercalation mode of binding for $TOTA^+$. Intercalation mode of binding typically induces a weaker CD response than does groove binding of a ligand. [23]

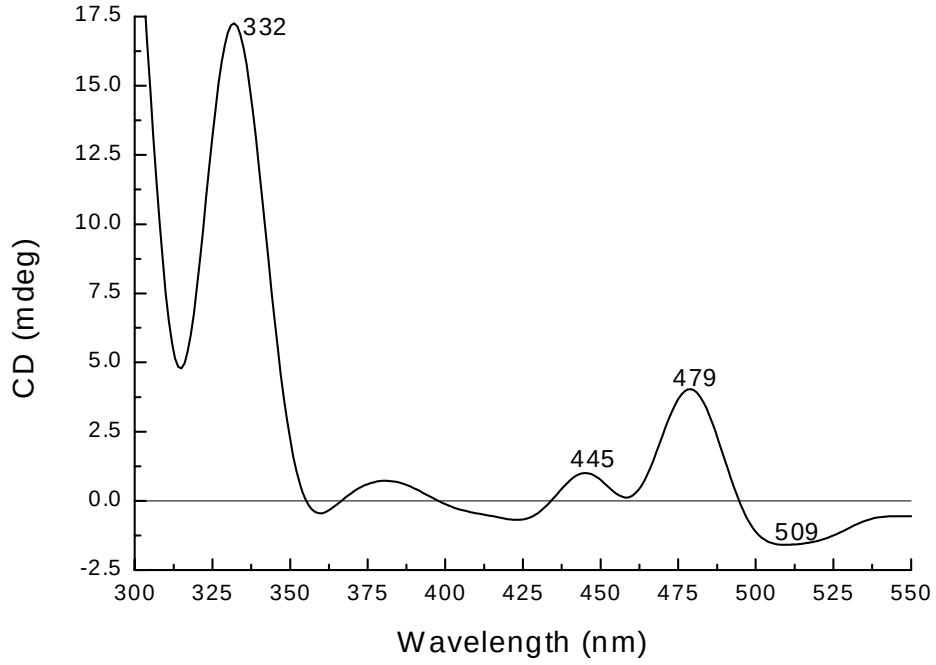

Figure 4.7. Induced circular dichroism (CD) spectrum for $TOTA^+$ (30 μM) in the presence of 33 μM sonicated calf thymus DNA (base pairs). 10 cm cylindrical quartz cell was employed. In the absence of DNA, no CD signal was observed in this region for $TOTA^+$. [24]

Further support of intercalation binding mode of $TOTA^+$ rather than groove binding can be achieved by monitoring the increase in absorbance at 260 nm of double helix DNA when temperature of the solution is raised. The thermal dissociation profiles provide information on the binding ligand, which is reflected in the melting temperatures (T_m). A positively charged intercalator stabilises the helical structure of DNA double helix and therefore increases T_m. A groove binder, on the other hand, has little or no effect on the T_m.

The T_m of a 12-mer dublex is increased by 4.5 ºC when one equivalent of $TOTA^+$ is added as depicted in figure 4.8. This in turn further supports that the intercalation mechanism is active for $TOTA^+$.

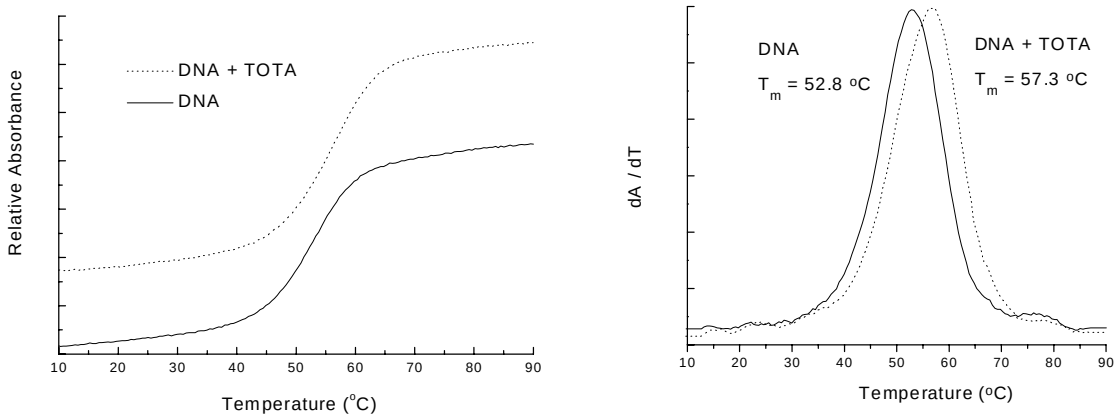

Figure 4.8. Heating curves obtained by monitoring the absorbance at 260 nm of a 12-mer dublex (5 μM) in 10 mM sodium phosphate buffer (pH = 7) without and with $TOTA^+$ (5 μM) are shown on the left hand side. The corresponding first derivative curves are shown on the right hand side.

4.3.3 Sequence and Structural Selectivity

The method utilised for sequence and structural selectivity was developed from a technique used by Müller and Crothers to explore the base specificity of DNA intercalation reactions.[32] In the application used here, a suitable buffer has been devised in which a variety of DNA and RNA structures are stable. Table 4.1 lists these structures, along with some of their physical properties. In the competition dialysis experiment, equal volumes of theses DNA samples (at identical concentrations) are dialysed against a common dialysate solution containing the ligand being studied. After equilibrium dialysis is attained (~24 h), the amount of ligand bound to each DNA is measured by a simple absorbance assay. Since all of the DNA samples are in equilibrium with the same free ligand concentration, the amount of bound ligand is directly proportional to the association constant for ligand binding

to a particular structure. Comparison of the amount of ligand bound to each DNA sample provides a rapid, thermodynamically rigorous indication of the structural selectivity of the ligand being studied.

Table 4.1. Nucleic acid conformation and samples used in competition dialysis experiment.

Conformation	DNA/oligonucleotide
Tetraplex DNA	$(5'\text{-}T_2G_{20}T_2\text{-}3')_4$
Triplex DNA	poly dA : $(\text{poly dT})_2$
Z - DNA	Brominated $(\text{poly (dGdC)})_2$
Duplex RNA	poly rA : poly U
DNA - RNA hybrid	poly rA : poly dT
Duplex DNA	$(\text{poly (dGdC)})_2$
	$(\text{poly(dAdT)})_2$
	poly dA : poly dT
	M. lysodeikticus (72% GC)
	Calf thymus DNA (42% GC)
	C. perfringes (31% GC)
Single strand pyrimidine	poly dT
Single strand purine	poly dA

Figure 4.9 illustrates the affinity of $TOTA^+$ towards the various DNA types. The data shows that there was no appreciable binding of $TOTA^+$ to single stranded forms [i.e., poly(dT) or poly(dA)]. $TOTA^+$ binds well to most duplex DNA forms, both from natural origin and synthetic deoxypolynucleotide duplexes. The exception is poly(dA)-poly(dT), to which $TOTA^+$ binds poorly as do most intercalators, an effect that is well known and which is due to the unusual structure adopted by the polymer in solution.[25] $TOTA^+$ shows a clear preference for GC base pairs, as judged by its increased level of binding to *M. lysodeikticus* (72% GC) DNA relative to that to *C. perfringes* (31% GC). $TOTA^+$ binds poorly, if at all, to RNA [poly(rA)-poly(U)] but slightly to the DNA-RNA [poly(rA)-poly(dT)] hybrid. Surprisingly, strong binding was observed to the triplex poly(dA)-poly(dT)_2 despite the fact that the triplex is made up from AT base pairs. This selectivity was confirmed by melting point measurements. Significant binding was found to the parallel stranded tertaplex form

$[(T_2G_{20}T_2)_4]$ and to the left handed Z-DNA. It is quite possible that the apparent affinity of $TOTA^+$ to Z-DNA is caused by allosteric conversion of the left-handed form of the polymer to a right-handed form, $TOTA^+$ forming stable complexes with the latter. This phenomenon has been established for the ethidium bromide intercalator. [26]

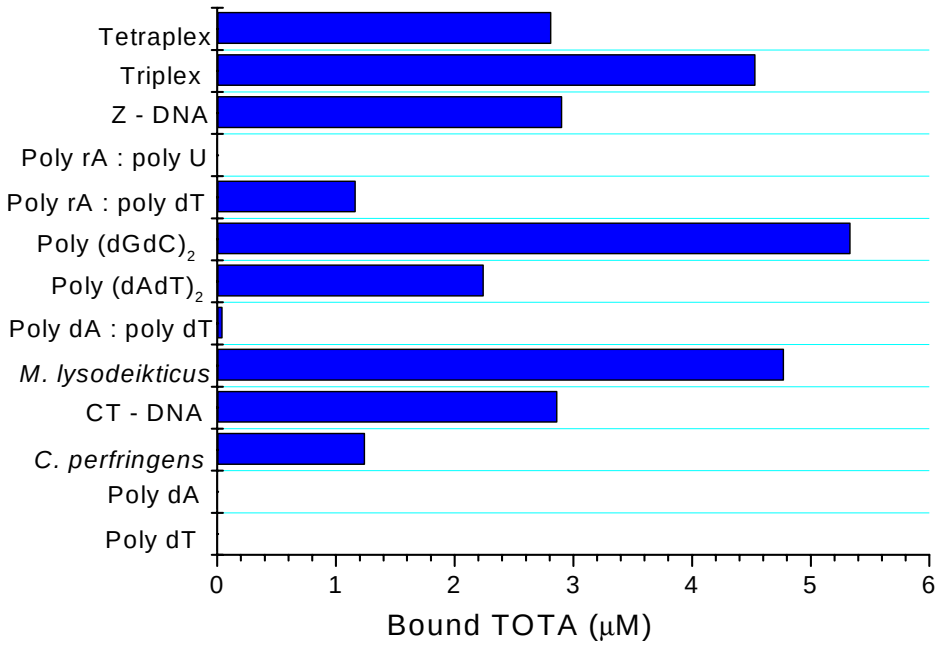

Figure 4.9. The amount of bound $TOTA^+$ to various nucleic acid conformation and samples deduced from the competition dialysis experiment. $TOTA^+$ shows a strong preference for GC pairs but it is overcome by structural affinity towards the triplex.

4.3.4 The Quenching of the Phosphorescence of $TOTA^+$

Excited triplet state formation of a DNA intercalated electron acceptor plays a crucial role in photooxidative damage of DNA. A triplet radical ion pair will exhibit slower charge recombination than the analogous singlet pair since the back electron transfer is spin forbidden, thereby permitting separation to compete effectively with back electron transfer. [27-31]

$TOTA^+$ phosphoresces moderately in a frozen solution. In the absence of DNA, excitation of $TOTA^+$ in a glassy matrix at 77 K leads to phosphorescence from its lowest triplet state (figure 4.10, next page). When $TOTA^+$ is bound to CT-DNA, the phosphorescence is completely quenched. The singlet state of $TOTA^+$ is quenched by CT-DNA (figure 4.5), which readily explains the disappearance the phosphorescence emission. However, it is still possible that the phosphorescence quenching can be partially attributed to rapid electron transfer form a DNA base to the excited triplet state of the $TOTA^+$ carbocation. This would facilitate charge migration in the DNA strand.

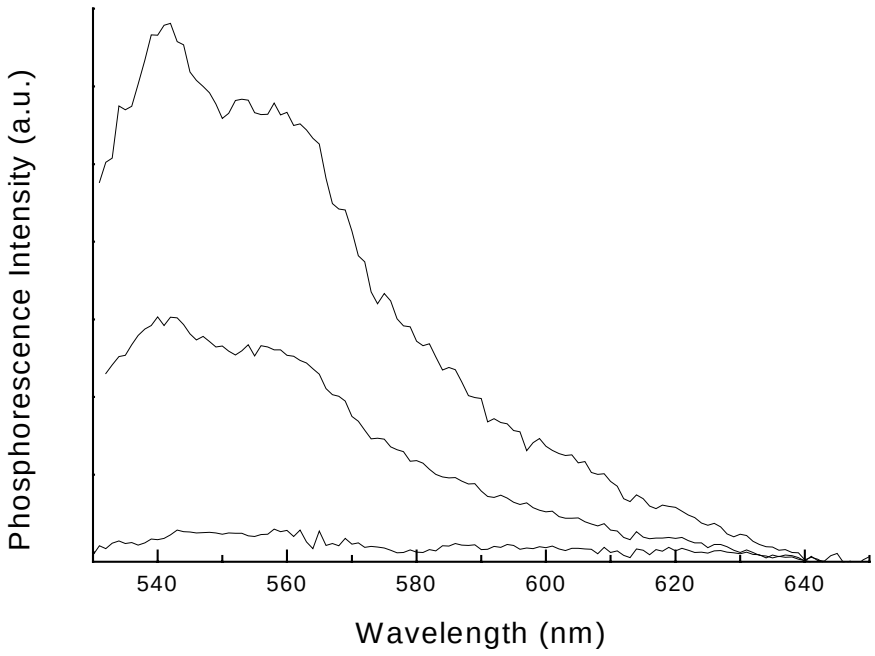

Figure 4.10. Quenching of the phosphorescence of $TOTA^+$, binding to calf thymus DNA in 1:1 (v/v) 10 mM sodium phosphate buffer (pH = 7) and ethylene glycol at 77 K. Total $TOTA^+$ concentration for each spectrum is 10 μM. DNA base pair concentration (μM) for each spectrum is (from top to bottom): 0.0, 10.0, and 50.0.

4.3.5 Cleavage of DNA

Photocleavage of DNA by $TOTA^+$ was investigated by means of electrophoreses. Damage appeared selectively at the 5'-G of GG step of duplex DNA after 2 hours of irradiation (see figure 4.11). A radical cation is postulated to localise at a GG step where it reacts irreversibly with H_2O and O_2.[31;32] This assumption is supported by *semi-empirical* calculations which indicate that GG steps may have a specially low oxidation potential.[33;34] No cleavage was observed for unirradiated $TOTA^+$ / DNA mixture indicating that no dark reaction occurred. The cleavage can possibly be caused by $^1O_2$ formed by interaction of $^3O_2$ with the excited singlet or triplet states of $TOTA^+$. The concentration of free $TOTA^+$ in solution was calculated to be 30 nM, which makes singlet oxygen an unlikely candidate causing cleavage. The appearance of the scission at the GG step in itself confirms that charge migration is initiated from photoexcited $TOTA^+$.

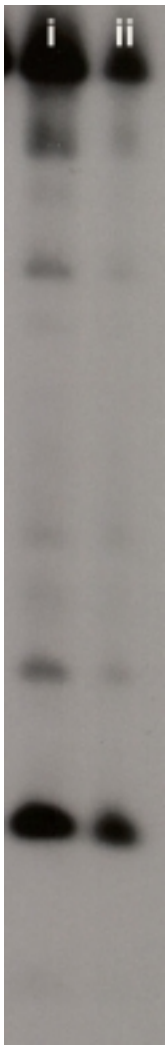

Figure 4.11. Autoradiogram demonstrating DNA cleavage of DNA duplex as induced by irradiation of $TOTA^+$ (350 nm). Lane i and ii irradiated for 2 and 3 hours respectively and treated with piperidine for 30 min at 90 °C. The two predominant spots in the lower region of the radiogram represent cleavage products at the GG step. Control experiments revealed no cleavage unless $TOTA^+$ is present and irradiated.

4.4 Discussion

Binding of $TOTA^+$ to DNA resulted in significant hypochromicity, considerable bathochromicity and induction of circular dichroism in the three lowest energy absorption bands. These results, taken together with the increased viscosity and melting temperature (T_m), lead us to assign intercalation between adjacent base pairs as the binding mode for $TOTA^+$ to DNA.[19; 20; 28; 41]

The binding constant for simple intercalators are in the 10^5 - 10^6 M^{-1} range,[35;36] which makes $TOTA^+$ ($K = 4.1\times10^4$ M^{-1}) somewhat a poorer binder than average. $TOTA^+$ is readily soluble in water (to the ca. 10^{-3} M limit) and since the main driving force for intercalation is hydrophobicity, [37;38]a lower than average binding constant can be expected.

A key feature of the intercalation model proposed by Lerman [39;40] is the lengthening of the DNA helix as the base pairs are separated to bind to the ligand. Hydrodynamic methods to determine length changes have been among the most stringent tests of the binding mode of ligands to DNA. [35;41] Viscosity measurements are sensitive to length changes for rod like DNA. $TOTA^+$ increases the length of DNA, resulting in an increased viscosity as seen in figure 4.6. The increase corresponded to 1.3 Å lengthening per intercalated $TOTA^+$. This is somewhat less lengthening compared to other intercalating agents, i.e., between 1.8 and 4.5 Å. [42-44] The classical intercalators proflavine and ethidium bromide give lengthening of only of 2.72 and 2.48 Å respectively, which is shorter than the expected 3.4 Å rise in the helix per base pair.[16;45] A number of possible reasons for this behaviour have appeared in the literature.

i) DNA segments do not behave as rigid rods. [16;36 46]

ii) A fraction of the bound ligand may be bound by electrostatic attachment to the outside of the helix and therefore not contributing to the lengthening.[35]

iii) Third, kinking or bending of the helix may occur, causing changes in persistence length. [47]

The second possibility can be disregarded in case for $TOTA^+$, since it has been shown that it intercalates and its Scatchard analysis[15] reveals a linear fit (figure 4.4) indicating only one mode of interaction between $TOTA^+$ and DNA.

A fourth explanation of shorter lengthening than expected can be related to the cationic nature of the intercalators. Due to their electron deficient nature, close interaction with the comparatively electron rich base pairs is expected. This interaction can possibly lead to shortening of distance between the intercaltor and the flanking base pairs. The exceptionally shorter lengthening for $TOTA^+$ can be attributed to its symmetry and the delocalisation of the positive charge over the whole molecule (see chapter 2). These properties should enable an extensive overlap of the π-orbitals of $TOTA^+$ and the adjacent base pairs, affecting a distortion of the double helix in order to accommodate the cationic nature of $TOTA^+$ resulting in the shorter lengthening.

The distance between base pairs of DNA dimers is reported to be 6.7 Å for intercalated proflavine and ethidium bromide employing crystallographic methods (see figure 4.12). [48-52] The lengthening is 3.3 Å, i.e., 0.1 Å shorter than the expected lengthening for classical intercalation. The effect of shorter lengthening discussed in previous paragraph for cationic intercalators attracting the flanking base pairs, can

possibly explain this shorter lengthening. This effect is undoubtedly diminished due to proflavine and ethidium carbocations being stacked both above and below the base pairs in the crystal lattice, thus competing for the π- electrons on the base pairs with their intercalated counterpart. Figure 4.12 depicts the DNA dimer and intercalated ethidium ion.

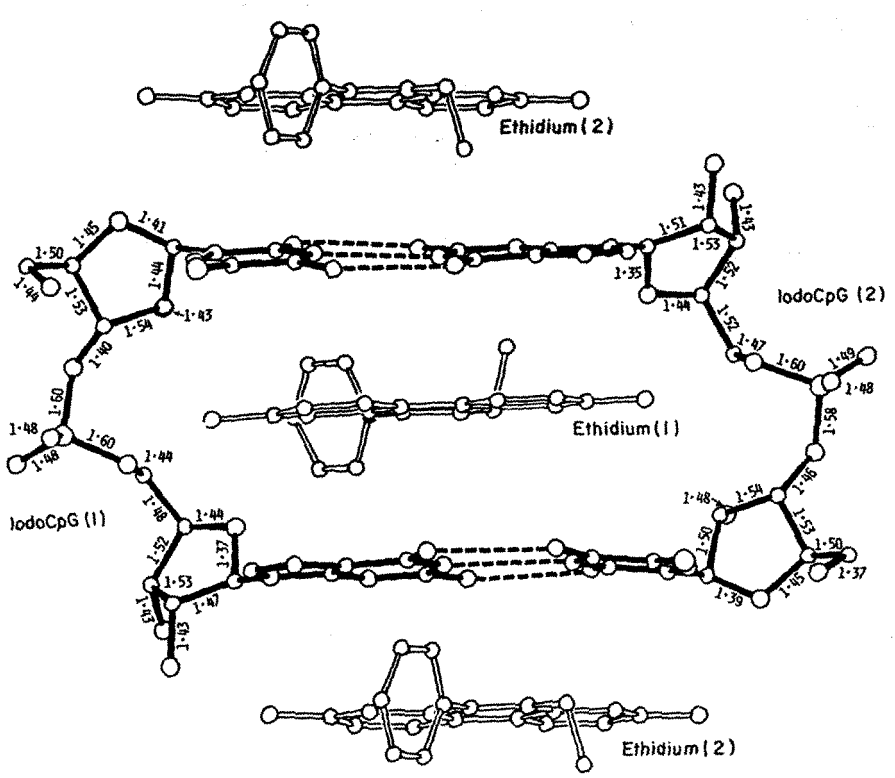

Figure 4.12. A portion of the ethidium:iodoCpG (cytosine phosphate guanine) crystal structure viewed approximately parallel to the planes of the guanine·cytosine base pairs and ethidium molecules showing bond distances of sugar-phosphate chains. IodoCpG molecules are drawn with dark solid bonds; intercalative ethidium molecule (ethidium (1)) and stacked ethidium molecules (ethidium (2)) have been drawn with light open bonds. Hydrogen bonding between guanine·cytosine base pairs in indicated with broken lines.[49]

Measures are being taken in order to obtain the crystal structure of a complex between $TOTA^+$ and a hexameric DNA double strand in order to verify the distorting effects of cationic species on the helical structure of DNA.

Simple intercalators, like $TOTA^+$, generally vary from being slightly GC to slightly AT specific.[53] Crothers and coworkers [53] have pointed out that due to the dipole moment of a GC base pair being greater than for an AT base pair, highly polarisable compounds exhibit significant GC base pair specificity. In agreement, the competition dialysis experiment clearly shows that $TOTA^+$ prefers to interact with GC base pairs (see figure 4.9). Also the oxidation potential of the guanine base is the lowest of the four bases making up the DNA base pairs,[54] facilitating close interaction with the electrophilic $TOTA^+$ carbocation. The structural affinity of $TOTA^+$ towards triplex DNA, even though it is made up by AT base pairs, can be explained by the size and electron deficiency of the π-system of $TOTA^+$. $TOTA^+$ is a six ring fused system and a triplex helix can provide a more extensive overlap with $TOTA^+$'s partially vacant π-orbtals than a dublex DNA. It is interesting that almost no interaction is observed between $TOTA^+$ and the single strands. Apparently base pairs are needed for an extended overlap of the π-systems, single bases not sufficing.

Thermodynamic considerations play a key role in assessing the likelihood that excited $TOTA^+$ carbocation will react with DNA by electron transfer. The oxidation potentials of the nucleic acid bases have been determined. [54;55]Guanine has the lowest oxidation potential and the purines are more easily oxidised than the pyrimidines. The reduction potential of $TOTA^+$ is –0.385 V (vis SCE). [56;57] The singlet energy has been determined at 239 kJ/mol and the triplet energy at 220 kJ/mol (see chapter 3). Substitution of these values into the Rehm-Weller equation (equation 4) [58;59] reveals that electron transfer from the DNA bases to the singlet or triplet excited states of $TOTA^+$ is exothermic and therefore thermodynamically feasible (~200 kJ/mol). The coulombic energy work term is omitted from the Rehm-Weller equations since no new charges are formed.

$$\Delta G_{et} = (E_{D+/D} - E_{A/A+} - \Delta E_{0,0}) \qquad 4)$$

The rapid quenching of the fluorescence of $TOTA^+$ by CT-DNA (figure 4.5) explains the reduced phosphorescence emission observed in figure 4.11. If no triplet state is formed in the excited ground state complex, then the migration of the electron from the DNA helix takes place to the singlet excited state. When $TOTA^+$ is reduced it forms a neutral radical and the donating base pair a radical cation, which in turn facilitates the radical cation to migrate more easily into the DNA strand, since no coulombic attraction exists between the radicals forming the geminate pair.

On the other hand if the triplet state forms then the back electron transfer is spin forbidden and the migration of the radical cation into the DNA strand is further facilitated. It has been shown that $TOTA^+$ forms a triplet state in water solution (chapter 3) and the phosphorescence is quenched by introduction of CT-DNA (figure 4.11). It has been demonstrated that the cage escape of radical ion products competes much more effectively with back electron transfer for triplet pairs, as opposed to singlet pairs generated from singlet precursors.[29;30;60]

The properties of the $TOTA^+$ - DNA complex is crucial to the question whether charge migration takes place from a triplet or a singlet state. If $TOTA^+$ retains its original photophysical properties, electron transfer from the adjacent bases quenches its singlet state. It has been demonstrated earlier in this chapter that the $TOTA^+$ - DNA interactions are very extensive, creating a supramolecular conglomeration. It can be argued that this system can form a triplet state, facilitating charge migration into the DNA strand.

It is clear that a scission takes place at the GG of a 12-mer oligomer when it is irradiated in the presence of $TOTA^+$ at 350 nm (figure 4.12). The available data does not suffice to determine whether singlet or triplet states are responsible for the migration of the radical cation into the DNA string.

The sequence of the 12-mer used in the cleavage experiment is 5'-AAAGGTAACGCG-3' and in the light of the affinity experiment (figure 4.9) $TOTA^+$ is either intercalated at the GG step or at the 3' end of the duplex as shown in figure 4.13.

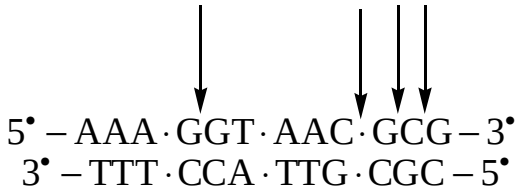

Figure 4.13. The 12-mer used in the cleavage experiment and its possible intercalation sites.

It can be argued that the a cleavage is not initiated at the GG step when $TOTA^+$ is intercalated there because it inhibits the concerted thermal motions necessary for a base to swing out of the stack and contact water molecules.[11] Therefore a charge has to travel at least five base pairs before reaching the GG step from the 3' end of the DNA duplex.

4.5 Conclusion

The $TOTA^+$ carbocation was found to intercalate between base pairs of a DNA duplex with the binding constant of $K = 4.1\times10^4\ M^{-1}$. $TOTA^+$ showed a clear affinity towards GC base pairs but also a significant structural selectivity for triplet DNA. Viscosity experiments reveal a 1.3 Å lengthening of a DNA rod per intercalated $TOTA^+$, which is the smallest value yet, reported in the literature. This implies that the intercalated ligand distorts the structure of the DNA helix to considerable extent.

The $TOTA^+$ carbocation is a photonuclease, scission appearing at GG steps in the DNA duplex.

4.6 Reference List

1) Wilson, E.K. *Chem.Eng.News* **1999**, *Aug. 23*, 43-48.

2) Murphy, C.J.; Arkin, M.R.; Jenkis, Y.; Ghatlia, N.D.; Bossmann, S.H.; Turro, N.J.; Barton, J.K. *Science* **1993**, *262*, 1025-1029.

3) Lewis, F.D.; Wu, T.; Zhang, Y.; Letsinger, R.L.; Greenfield, S.R.; Wasielewski, M.R. *Science* **1997**, *277*, 673-67.

4) Wan, C.; Fiebig, T.; O'Kelley, S.; Treadway, C.R.; Barton, J.K.; Zewail, A.H. *Proc.Nat.Acad.Sci.USA* **1999**, *96*, 6014-6022.

5) Steenken, S.; Jovanovic, S.V. *J.Am.Chem.Soc.* **1997**, *119*, 617-618.

6) Jortner, J.; Bixon, M.; Langenbacher, T.; Michel-Beyerle, M.E. *Proc.Nat.Acad.Sci.USA* **1998**, *95*, 12759-12765.

7) Marcus.R.A. *J.Chem.Phys.* **1965**, *43*, 679-683.

8) Marcus.R.A. *Ann.Rev.Phys.Chem.* **1964**, *15*, 155-196.

9) Marcus.R.A.; Sutin, N. *Biochimica et Biophysica Acta* **1985**, *811*, 265-322.

10) Henderson, P.T.; Jones, D.; Hampikian, G.; Kan, Y.; Schuster, G.B. *Proc.Nat.Acad.Sci.USA* **1999**, *96*, 8353-8358.

11) Folta-Stogniew, E.; Russu, I. *Biochemistry* **1996**, *35*, 8439

12) Wilson, W.D.; Tanious, F.A.In Neidle, S., Waring, M.J., Eds.; The Macmillan Press Ldt.: London, 1994; pp 243

13) Neidle, S. *Landolt - Bornstein Nuleic Acids*. Saenger, W., Ed.; Springer Verlag: Berlin, Heidelberg, 1989; pp 247

14) Faldt, A.; Krebs, F.C.; Thorup, N. *J.Chem.Soc., Perkin Trans.2* **1997**, 2219-2227.

15) Peacocke, A.R.; Skerret, J.N.H. *Faraday Soc.Trans.* **1956**, *52*, 261-279.

16) Cohen, G.; Eisenberg, H. *Biopolymers* **1969**, *8*, 45-55.

17) Ren, J.; Chaires, J.B. *Biochemistry* **1999**, *38*, 16067-16075.

18) Sambrook, J.; Fritsch, E.F.; Maniatis, T. *Molecular Cloning. A Laboratory Manual*; Cold Spring Harbor Laboratory Press: Cold Spring Harbor, NY, 1989;

19) Scathard, G. *Ann.N.Y.Acad.Sci.* **1949**, *51*, 660-672.

20) Lakowics, J.R. *Principles of Fluorescence Spectroscopy*; Plenum Press: New York, 1983; pp 257-301.

21) Nordén, B.; Tjerneld, F. *Biopolymers* **1982**, *21*, 1713-1734.

22) Kubista, M.; Åkerman, B.; Nordén, B. *J.Phys.Chem.* **1988**, *92*, 2353-2356.

23) Lyng, R.; Rodger, A.; Nordén, B. *Biopolymers* **1991**, *31*, 1709-1720.

24) Lyng, R.; Rodger, A.; Nordén, B. *Biopolymers* **1992**, *32*, 1201-1214.

25) Herrera, J.E.; Chaires, J.B. *Biochemistry* **1989**, *28*, 1993-2000.

26) Walker, G.T.; Stone, M.P.; Krugh, T.R. *Biochemistry* **1985**, *24*, 7462-7471.

27) Armitage, B.; Yu, C.; Devadoss, C.; Schuster, G.B. *J.Am.Chem.Soc.* **1994**, *116*, 9847-9859.

28) Johnston, L.J.; Wong, D.F. *J.Phys.Chem.* **1993**, *97*, 1589-1595.

29) Gould, I.R.; Ege, D.; Moser, J.E.; Farid, S. *J.Am.Chem.Soc.* **1990**, *112*, 4290-4301.

30) Gould, I.R.; Ege, D.; Mattes, S.L.; Farid, S. *J.Am.Chem.Soc.* **1987**, *109*, 3794-3796.

31) Ly, D.; Kan, Y.; Armitage, B.; Schuster, G.B. *J.Am.Chem.Soc.* **1996**, *118*, 8747-8748.

32) Breslin, D.T.; Schuster, G.B. *J.Am.Chem.Soc.* **1996**, *118*, 2311-2319.

33) Saito, I.; Nakamura, T.; Nakatani, K.; Yoshioka, Y.; Yamaguchi, K.; Sugiyama, H. *J.Am.Chem.Soc.* **1998**, *120*, 12686-12687.

34) Sugiyama, H.; Saito, I. *J.Am.Chem.Soc.* **1996**, *118*, 7063-7068.

35) Dougherty, G.; Pilbrow, J.R. *Int.J.Biochem.* **1984**, *16*, 1179-1192.

36) Müller, W.; Crothers, D.M. *J.Mol.Biol.* **1968**, *35*, 251-290.

37) Chaires, J.B. *Curr.Opin.Struc.Bio.* **1998**, *8*, 314-320.

38) Chaires, J.B. *Biopolymers* **1998**, *44*, 201-215.

39) Lerman, L.S. *J.Mol.Biol.* **1961**, *3*, 18-30.

40) Lerman, L.S. *Proc.N.A.S.* **1963**, *49*, 94-102.

41) Suh, D.; Chaires, J.B. *Bioorg.Med.Chem.* **1995**, *3*, 723-728.

42) Maiti, M.; Nandi, R.; Chaudhuri, K. *Ind.J.Bio.Biophys.* **1984**, *21*, 158-165.

43) Waring, M.J.; Gonzáles, A.; Jiménez, A.; Vázques, D. *Nuc.Acids Res.* **1979**, *7*, 217-230.

44) Baez, A.; Gonzáles, A.; Vázques, D.; Waring, M.J. *Biochem.Pharma.* **1983**, *32*, 2089-2094.

45) Saucier, J.M.; Festy, B.; Le Pecq, J.B. *Biochimie* **1971**, *53*, 973-980.

46) Li, H.I.; Crothers, D.M. *J.Mol.Biol.* **1969**, *39*, 461-477.

47) Gabbay, E.J.; Scofield, R.E.; Baxter, C.S. *J.Am.Chem.Soc.* **1973**, *95*, 7850-7857.

48) Tsai, C.; Jain, S.C.; Sobell, H.M. *J.Mol.Biol.* **1977**, *114*, 301-331.

49) Jain, S.C.; Tsai, C.; Sobell, H.M. *J.Mol.Biol.* **1977**, *114*, 317-331.

50) Jain, S.C.; Sobell, H.M. *J.Biomol.Stru.Dynm.* **1984**, *1*, 1161-1177.

51) Jain, S.C.; Sobell, H.M. *J.Biomol.Stru.Dynm.* **1984**, *1*, 1179-1194.

52) Bhandaty, K.K.; Sakore, T.D.; Sobell, H.M.; King, D.; Gabbay, E.J. *J.Biomol.Stru.Dynm.* **1984**, *1*, 1195-1217.

53) Müller, W.; Crothers, D.M. *Eur.J.Biochem.* **1975**, *54*, 267-277.

54) O'Neill, P.; Davies, S.E. *Int.J.Radiat.Biol.* **1987**, *52*, 577-587.

55) Jovanovic, S.V.; Simic, M.G. *J.Phys.Chem.* **1986**, *90*, 974-978.

56) Nemcová, I.; Nemec, I. *J.Electroanal.Chem.* **1971**, *30*, 506-510.

57) Nemcová, I.; Nemec, I. *Chem.zvesti.* **1972**, *26*, 115-125.

58) Rehm, D.; Weller, A. *Ber.Bunsen-Ges.Phys.Chem.* **1969**, *73*, 834-839.

59) Rehm, D.; Weller, A. *Isr.J.Chem.* **1970**, *8*, 259-271.

60) Johnston, L.J.; Wong, D.F. *Can.J.Chem.* **1992**, *70*, 280-282.

Chapter 5

Structural Properties of DNO Investigated with Pyrene Excimer Formation

5.1.1 Introduction

The initial objective of this project was to lodge $TOTA^+$ between two large fused ring aromatics; i.e. to make a molecular sandwich where $TOTA^+$ acts as the salami and the aromatic molecules as slices of bread. To hold this conglomeration together the idea was to attach the aromatics to a synthetic polypeptide (the butter for the sandwich). This is depicted in figure 5.1.

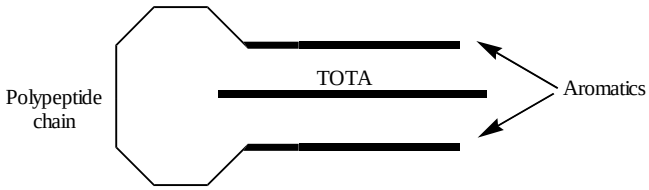

Figure 5.1. The envisioned structure of the $TOTA^+$-aromatic sandwich structure.

If such structures were relatively easily synthesised, the next step would be to make heterogenic liquid crystals. Liquid crystals today are often made up from large carbocationic centre units with aliphatic tendrils, which stack into columns. A column stack made up of a carbocationic species sandwiched between neutral aromatics would undoubtedly demonstrate interesting new properties.

Pyrene was used as the aromatic moiety and the polypeptide is called DNO (see later in text). The DNO and $TOTA^+$ absorption and emission spectra overlap extensively as shown in figure 5.2 (see next page). Substituted DNO oligomers have

very low solubility in polar and non-polar solvents. Due to these factors the experimental results were inconclusive whether a sandwich structure formed or not.

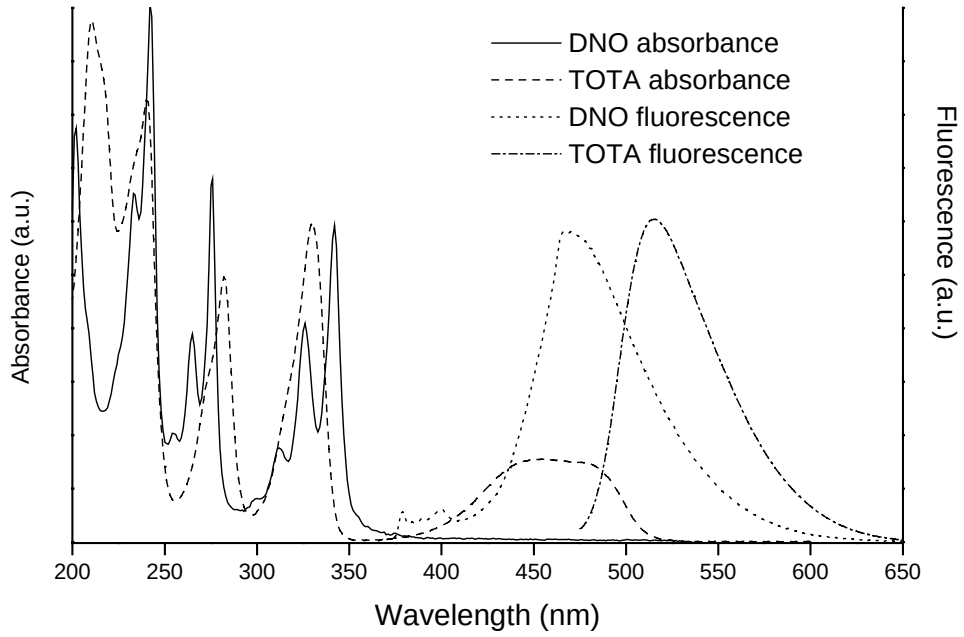

Figure 5.2 The absoprtion and emission spectra of $TOTA^{+}$ and a DNO derivative.

On the other hand considerable structural information was gleaned from the photophysical data collected on the DNO derivatives as will be described on the following pages.

5.1.2 Introduction

Peptides are ideally suited for the design and synthesis of novel molecules and materials with potentially interesting structures and functions. [1-3] Recently, a novel class of peptides containing azobenzene chromophores was investigated as materials for optical storage of information. [4-6] These peptides can be made up of diamino acids, e. g., ornithine units (DNO, figure 5.3) dimerised or oligomerised through the δ-amino groups and with the chromophores attached to the α-amino groups by carbonyl linkers. In analogy to the design of PNA [7-9], DNO was designed with a molecular geometry similar to that of DNA so as to impose orientational order on the chromophores.

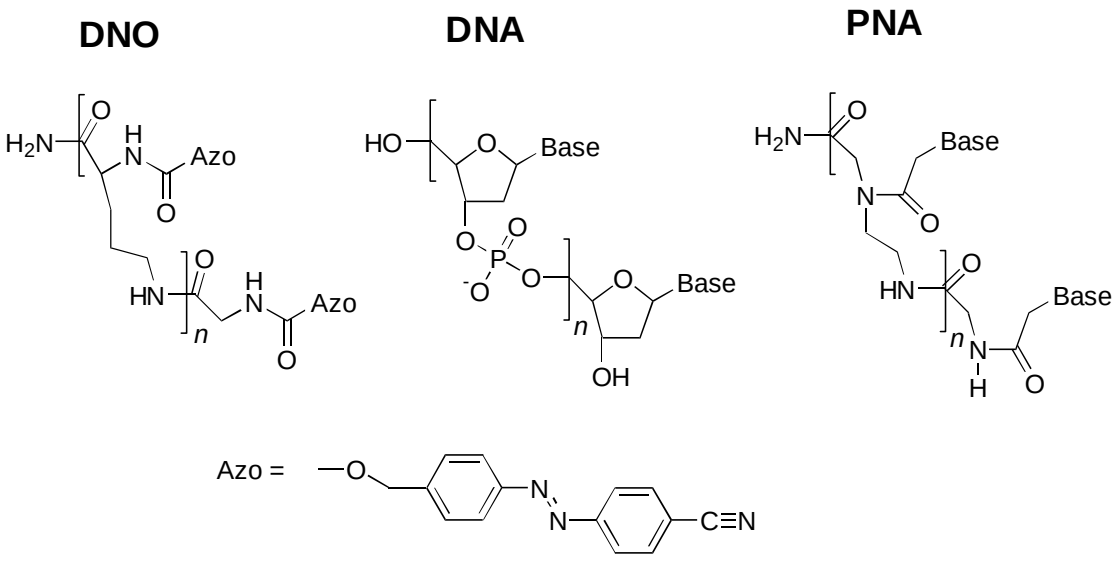

Figure 5.1. Chemical structures of ornithine-based DNO substituted with azobenzene chromophores, DNA and PNA.

At present, it has not been possible to obtain direct structural information about DNO *via* x-ray crystallography or NMR spectroscopy.

Photophysical probes have been used extensively in order to investigate the structure and dynamics of molecules in a variety of systems. [10] In the present paper, we report on the structural properties of DNO investigated with pyrene excimer formation. Excimer (excited dimer) formation of two pyrene moieties is one of the more widely used photophysical probes. [11] The pyrene excited singlet state has the interesting property of efficient excimer formation with its ground state counterpart, as well as a high fluorescence quantum yield and a long lifetime (ϕ_{fl} = 0.72 [12], τ_{fl} = 190 ns in polar solvents [13]). The excimer is largely deactivated by emission, which takes place at a longer wavelength (~ 480 nm) than the fluorescence of the pyrene singlet state (~ 380 nm). These properties make a pyrene pair an excellent photophysical probe. The first obvious consequence of pyrene chromophores being linked to the same molecule is the greatly enhanced local concentration of the chromophores allowing excited state complex formation at very low concentrations. The extent of excimer formation is limited by the probability for a molecule containing two pyrenyls to reach, within the lifetime of the excited singlet state, a conformation suitable for excimer formation. [14] The interchromophore face-to-face distance of excimers has been estimated to be ca. 3 to 3.5 Å in diaryl substituted polypeptides. [15] However, due to molecular fluctuation at room temperature and taking the attractive forces of the excimer in account, the critical distance of excimer formation is ca. 4.5 Å for pyrenyl groups. [15]

Winnik has described very useful experimental criteria to detect pyrene ground state association and excimer formation in supramolecular systems utilising absorption and fluorescence spectroscopic techniques. [11] The pyrene molecule has a distinct vibronic structure observed for its absorption and fluorescence excitation spectra, which looses its resolution when association between two pyrene moieties

takes place in the ground state. The peak-to-valley ratio of the (0,0) transition of the ^1L_a band and its adjacent minimum is a convenient way of measuring this loss of resolution (see results for further details). [11] Relative bathochromic shift of the excitation fluorescence excimer spectrum compared to the spectrum of the monomer of the (0,0) transition in the ^1L_a bands (341-2 nm) is also indicative of a ground state association [$\Delta\lambda = \lambda_{max}$(excimer)-$\lambda_{max}$ (pyrene)]. [11] In systems where association occurs, $\Delta\lambda$ takes positive values from 1 to 4 nm. [11]

Here, four pyrene-substituted DNO dimers (**DNO-1**, **DNO-2**, **DNO-3**, and **DNO-4**, respectively, Figure 5.4) were prepared. The pyrene pair was used as a photophysical probe to investigate the effect of varying the number of bonds in the backbone. A pyrene monomer (**1**) was prepared as a reference. The absorption, fluorescence excitation and emission spectra of the derivatives were measured as well as the lifetimes of the fluorescence emissions. The data are analysed for information on the DNO backbone's structure and dynamics based on the experimental criteria defined by Winnik [11] and by comparison with force field calculations.

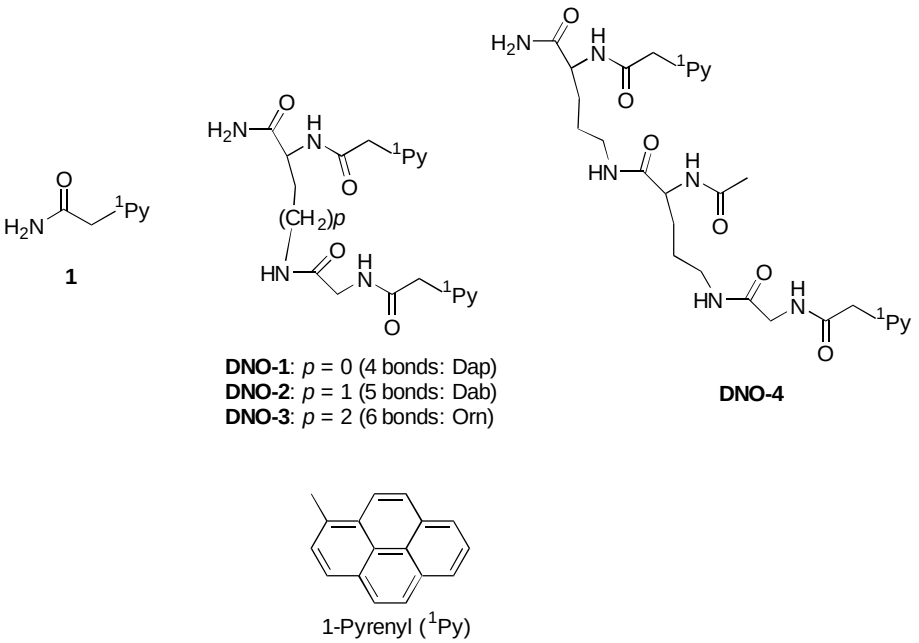

Figure 5.4. Chemical structures of the DNOs used in this study.

5.2 Experimental

The DNOs were synthesised by stepwise Merrifield synthesis [16;17] using a synthetic protocol similar to the one previously reported for azobenzene-substituted DNO [4] except that (1-pyrenyl) acetic acid was used as the side-chain monomer. The DNOs were purified by semi-preparative HPLC and were shown to have the expected molecular masses by MALDI-TOF mass spectrometry.

The absorption spectra were measured on a Perkin-Elmer Lambda 5 UV/VIS Spectrophotometer using 1×1 cm optical quartz cells.

Solutions (~1×10^{-5} M in methanol) were prepared in order to obtain the fluorescence excitation and emission spectra and lifetimes. Methanol (HPLC-quality) was used as received and it showed no fluorescence at the excitation wavelengths employed.

For steady state fluorescence emission and excitation spectra a FS900, Edinburgh Analytical Instrument luminescence spectrometer was used. Highly concentrated (ca. 5 g/L) solution of Rhodamine B in glycerol was used as a quantum counter in order to correct the excitation spectra. Raman scattering did not interfere with any of the fluorescence spectra shown.

The fluorescent lifetimes were measured on a time-correlated single-photon-counting (SPC) apparatus (FL900, Edinburgh Analytical Instruments) using a nanosecond flash lamp filled with nitrogen or hydrogen. The nitrogen line at 337 nm and hydrogen at the same wavelength were used for excitation. Hydrogen was used for lifetimes below and nitrogen above 10 ns. Emission was monitored at 378 nm and 466 nm. As a detector photomultiplier tube was used (Hamamatsu R1527). A Ludox dispersion was used to obtain the instrument response function. Fluorescence decay curve analysis was performed by a reconvolution of the instrument response function with

an assumed decay law. The decay parameters were determined by a least-squares fitting routine, the quality of which was evaluated by the reduced χ^2 values, as well as by the randomness of the weighted residuals.

Both steady state and time-resolved fluorescence experiments were performed in the normal 90° configuration. All samples were purged with argon prior to fluorescence emission measurements.

The program HyperChem 4.0 [18] was used for geometry optimisation with the MM+ force field package.

5.3 Results

5.3.1 Absorption

The absorption spectrum for the monomer **1** is shown in figure 5.5. The absorption spectra of the other derivatives including two pyrene chromophores are qualitatively identical except broadening of the vibronic bands and a slight red shift of ca.1 nm for the band at 341 nm. A convenient relative measure of the loss in resolution can be extracted from the ratio (P_A) of the absorption intensity of the most intense band (341 nm, (0,0) transition in ^1L_a band) and that of the adjacent minimum at shorter wavelength. [11] This ratio is usually smaller than 3.0 for ground state associated systems for 1-substituded pyrenyl compounds. [11] The P_A values were determined for all the derivatives and the results are given in table 5.1. The P_A value of **1** is 3.6, which is considerably higher than for the other derivatives and is a clear indication that a ground state association is present in all the doubly substituted derivatives. The DNO-1 and DNO-2 dimers show considerably more ground state complexation than their DNO-3 and DNO-4 counterparts.

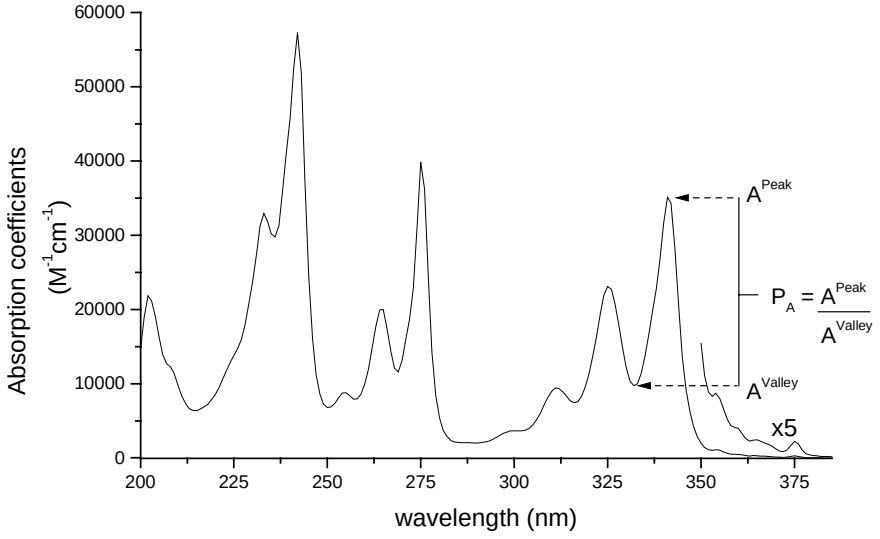

Figure 5.5. The absorption spectrum of the monomer (**1**) in methanol at room temperature. The ^1L_a (0,0) transition at 341 nm and the adjacent valley at 332 nm were used to determine P_A.

5.3.2 Steady State Emission Spectra

The fluorescence spectra obtained are depicted in figure 5.6. All of the DNO derivatives with two pyrenyl moieties exhibit emission at 466 nm, albeit the intensity of the **DNO-2** is relatively low. This emission must be contributed to the formation of intramolecular excimers between the pyrene groups, because insignificant fluorescence was observed at 466 nm for **1** at the same concentration. The excimer emission maxima of the derivatives are at the same wavelength, which entails that the same excimer species is present for all the derivatives. The relative efficiency of an excimer formation is expressed by the ratio I_E/I_M of intensities measured at the maxima of excimer (I_E = 466 nm) and monomer (I_M = 378 nm) emissions, respectively. [11] I_E/I_M of the intensities were determined for all the derivatives and the results are shown in table 5.1.

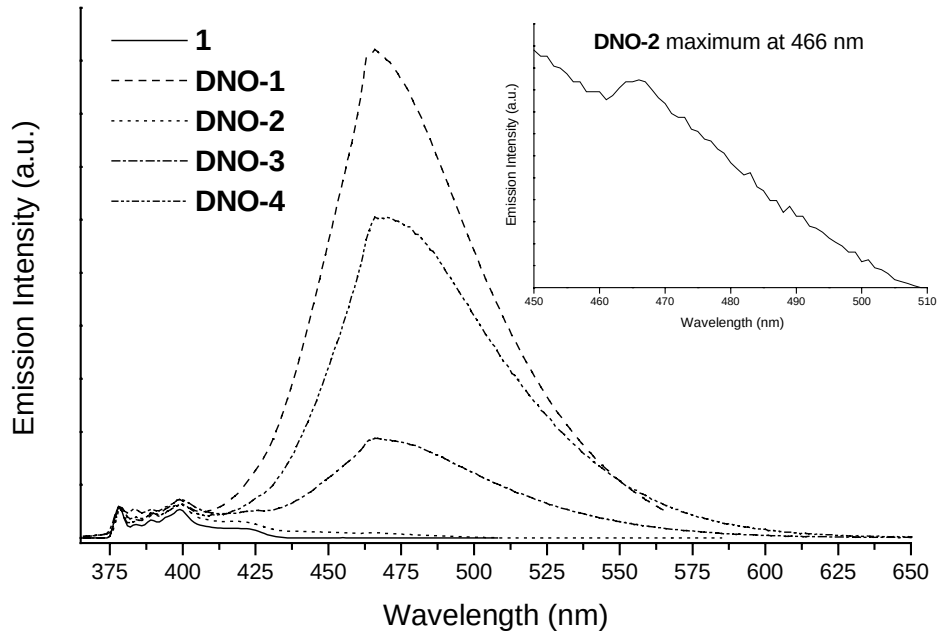

Figure 5.6. The steady state emission spectra of the derivatives in methanol at room temperature (~1×10^{-5} M). The spectra are normalised at 378 nm. The maxima of the monomer emission are at 378 (I_M) and 399 nm. The excimer peak is localised at 466 nm (I_E). The inset depicts the maximum of the **DNO-2** derivative.

It is apparent that the **DNO-1** has the most intensive excimer emission compared to the monomer fluorescence, followed by the **DNO-4** derivative. The **DNO-3** derivative showed considerable excimer emission but hardly any is observed for the **DNO-2** derivative.

5.3.3 Excitation Spectra

The pyrene and excimer excitation spectra for **DNO-1** are depicted in figure 5.7. Association can be revealed by comparing the adjacent peak-to-valley ratio for the (0,0) transition in the ^1L_a band (341-2 nm) of the excitation spectra recorded at the monomer (P_M) and the excimer (P_E) emissions maxima. [11] In situations where pyrene association in the ground state takes place P_E is smaller than its P_M counterpart. [11] The results for the derivatives are given in table 5.1. The **DNO-2** derivative shows the most extensive association followed by **DNO-1**. On the other hand, the **DNO-3** and **DNO-4** dimers demonstrate hardly any ground state aggregation when their P_M and P_E values are compared.

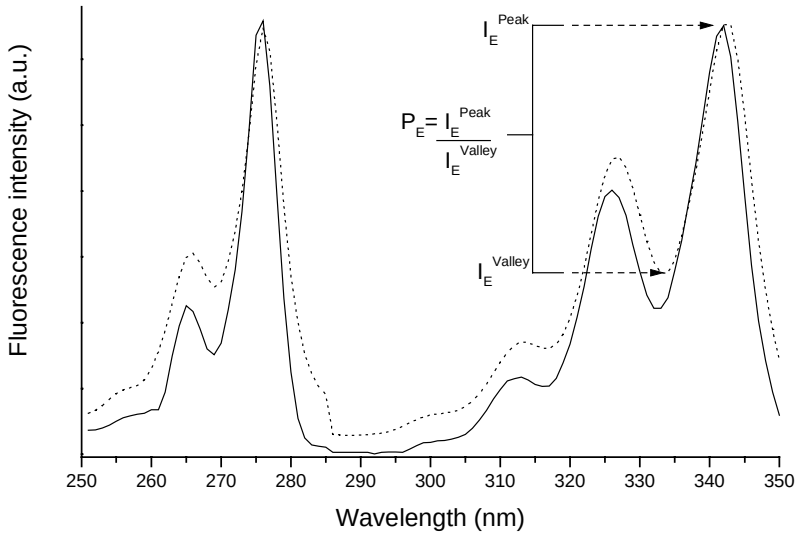

Figure 5.7 Normalised excitation spectra of the **DNO-1** derivative in methanol at room temperature. Emission is monitored at 378 nm (monomer, full line) and 466 nm (excimer, dotted line). The loss of the resolution is reflected in the P_M and P_E values determined from the ratio of the transitions at 341-342 nm and its adjacent valley.

The monomer **1** does not have an opportunity to form a ground state complex due to its low concentration (1×10^{-5} M) [19], hence its relatively large P_M value. The red shift of the wavelength maxima for the (0,0) transition in the ^1L_a band of the excimer emission compared to the monomer fluorescence is 1 nm for the **DNO-3** and **DNO-4** dimers and 2 nm for the **DNO-1** and **DNO-2** derivatives. These observations support the results obtained by the peak- to-valley criteria, i.e., the **DNO-1** and **DNO-2** derivatives exhibit more extensive ground state association than the **DNO-3** and **DNO-4** dimers.

5.3.4 Time resolved fluorescence

The lifetime of the observed fluorescence was measured at the pyrene (378 nm, τ_M) and the excimer (466 nm, τ_E) emissions and the results are shown in table 5.1. The decay of the **DNO-3** excimer emission is depicted in figure 5.8.

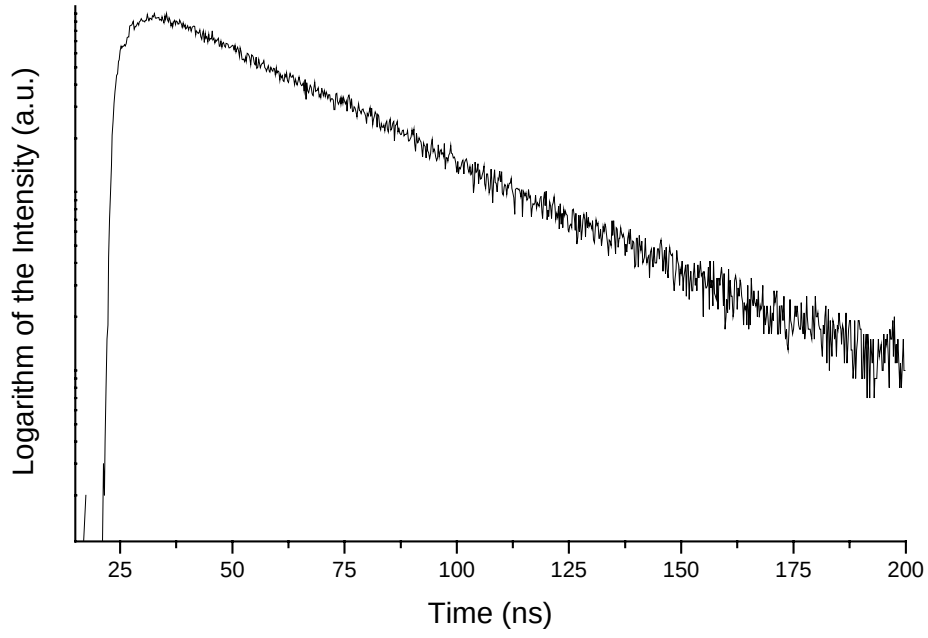

Figure 5.8. The emission decay curve of the **DNO-3** derivative excimer emission, monitored at 466 nm in methanol at room temperature.

Monomer **1** has a long lifetime, similar to the lifetime of unsubstituted pyrene (190 ns in ethanol [13]). The lifetime of the pyrene emission of **DNO-1**, **DNO-3** and **DNO-4** are much shorter due to excimer formation, which deactivates the pyrene singlet state. The **DNO-2** dimer falls in neither category. Single exponential decay is observed for all the derivatives within the time regime available. De Schryver *et al.* associates a two-decay parameter of the pyrene fluorescence with two ground state peptide chain conformations. [20] Hence, it is possible to attribute the pyrene fluorescence single exponential decay of the **DNO-1**, **DNO-3** and **DNO-4** derivatives to one ground state conformation.

The excimer decay parameters are all single exponential, and have similar lifetimes ranging from 35 to 42 ns. This homogeneity in decay profiles within the excimer emission signals the existence of only one emitting excimer species. [11]

It was possible to follow the formation time of the excimers of the **DNO-3** and **DNO-4** dimers as shown in figure 5.9.

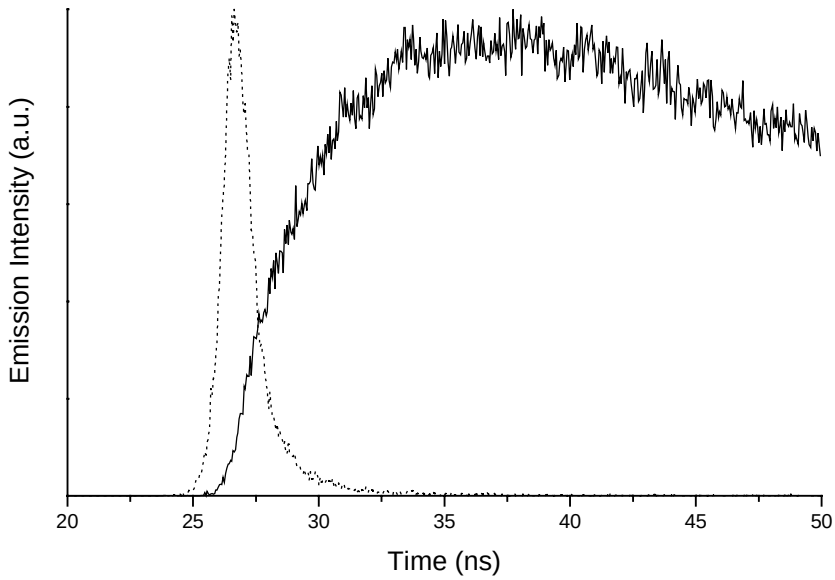

Figure 5.9. The formation curve of the excimer for the **DNO-4** derivative measured in methanol at room temperature.

However, since the time resolution of the present experiments is limited to approximately 1 ns, it was not possible to measure the formation times for the **DNO-1** and **DNO-2** dimers, which fall into the picosecond regime. The rise times of the **DNO-3** and **DNO-4** derivatives were fitted to equation 1:

$$I_F = A_1\left(1 - e^{-t/\tau_F}\right) \quad 1)$$

The formation times (τ_F) are given in table 5.1. The **DNO-3** derivative exhibits a faster formation rate than its **DNO-4** counterpart.

The monomer lifetimes (τ_M) and excimer rise times (τ_F) for the **DNO-3** and **DNO-4** derivatives correlate well, connecting the deactivation of the pyrene singlet state and the formation of the excited dimer.

Table 5.1. The I_E/I_M is the ratio of the monomer and excimer steady state emissions. P_M and P_E are the peak to valley ratios for the monomer and excimer excitation spectra, respectively. P_A is the peak to valley ratio for the absorption spectra. The time resolved values are the monomer emission lifetimes (τ_M), excimer lifetimes emission (τ_E) and the formation time of the excimer (τ_F).

	Absorption	Emission	Excitation		Time resolved fluorescence		
	P_A[b]	I_E/I_M[b]	P_M[b]	P_E[b]	τ_M[c] (ns)	τ_E[b] (ns)	τ_F[d] (ns)
1	3.6	x	3.4	x	153[b]	x	x
DNO-1	2.3	15.8	3.0	2.4	2.1	42.4	0[a]
DNO-2	2.4	0.2	2.6	1.7	62.4[b]	36.5	0[a]
DNO-3	2.8	3.2	2.3	2.4	3.0	34.8	3.5
DNO-4	2.9	10.3	2.3	2.2	3.8	41.3	4.5

x: no excimer emission observed
a) time resolution not adequate
b) estimated error ± 5%
c) estimated error ± 10%
d) estimated error ± 15%

5.3.5 Force field calculations

The structures were optimised from the classical B-DNA geometry with the MM+ force field package. The average distance between pyrene moieties obtained for the DNO derivatives is 4.0 ± 0.1 Å, which is within the critical distance of excimer formation predicted at ca. 4.5 Å. [15] The angles between the molecular long axis of the pyrene moieties were determined as 19.1° ± 0.2° for the **DNO-1**, **DNO-3** and **DNO-4** derivatives. However, the **DNO-2** exhibits an angle of 10.0°. The molecular mechanics results have to be interpreted carefully, since solvent and electronic effects are omitted, in particular hydrogen bonds cannot be simulated with the MM+ package. Since these non-covalent interactions cannot be effectively reproduced only qualitative conclusions should drawn from these calculations.

The excimer state has been described theoretically by configurational mixing of exciton – resonance states and charge resonance states.[21;22] The optimal geometry of the pyrenyls is the parallel arrangement of the molecular long axes in the excimer state. Both the exciton and resonance interactions favour a sandwich-like structure since they yield the smallest distance between the molecular centres. [21] The geometries of the pyrene moieties predicted by the MM+ package are not far form the criteria for excimer formation described above and this geometry is only imposed on them by the DNO backbone.

5.4 Discussion

It has been observed that the intensity of the excimer emission in pyrene labelled polypeptides is dependent on the chirality of the 1-pyrenylalanine employed in their synthesis [23]. Circular polarised fluorescence spectra (CPF), of pyrene labelled polypeptides, show negative and positive dissymmetries in the pyrene excimer emission wavelength range [24]. Dissymmetric CPF spectra are diagnostic of the presence of the more than one emissive species [25]. Egusa *et al.* [23;26] attributed the dissymmetry observed in the CPF spectra of pyrene labelled polyalanines to the presence of two kinds of excimer species: a non-polar excimer (λ_E = 460 nm) of well defined geometry and a polar excimer emitting at longer wavelengths (λ_E = 520 nm), which may exist in a variety of configurations and where the interchromophoric distance is longer than for the non-polar excimer.

In the present study, the pyrene excimer emission maximum is invariably found at 466 nm for the **DNO** series, which means that the hypothetical non-polar excimer species are predominant. Furthermore, in all lifetime measurements - monomer or excimer - a strictly monoexponential decay was observed and only insignificant variation was observed in the excimer lifetime (τ_E, Table 5.1). These findings support the existence of a single equilibrium excimer geometry common to all the molecular systems.

The structural differences among the **DNO**-derivatives rely mainly on the length of the backbone connecting the amide units bearing the pyrenyl substituents (Figure 5.4). **DNO-1**, **DNO-2**, and **DNO-3** are DNO-dimers having a linking chain of 4, 5, and 6 bonds, respectively, between the α-carbonyls of the dipeptide. **DNO-4** is a tripeptide with a total of 12 bonds in the linking chain including the intermediate amide group.

The increasing chain length in the series **DNO-1** to **DNO-4** is parallel to the observed increase in the P_A-parameter (Table 5.1), being derived from the absorption spectra. A smaller P_A-value, as observed for **DNO-1,** means stronger interaction between the ground state pyrenyls. Still, they are not completely independent even in **DNO-4**, since the P_A value remains markedly lower than that for the free monomer **1**. From the absorption data alone it cannot be concluded, whether the increased decoupling in the series **DNO-1** to **DNO-4** relates to higher flexibility of the longer chains or if a generally rigid configuration is increasingly unfavourable for interaction between the pyrenyls.

However, the ratio between the relative fluorescence intensities originating from excimer and excited monomer (I_E/I_M, Table 5.1) decreases dramatically when going from **DNO-1** ($I_E/I_M = 15.8$) to **DNO-2** ($I_E/I_M = 0.2$). Apparently, the dominating ground state configuration of **DNO-2** represents a very unfavourable geometry for excimer formation from ground state associated pyrenyls. Furthermore, the configuration is locked so that any configurational diffusion is prohibited. Since the **DNO-1** backbone is shorter than that of **DNO-2,** restricted mobility of the pyrenyls must also be expected in **DNO-1**. In this case, however, the dominating ground state configuration is very favourable for excimer formation as reflected in the high I_E/I_M value. An increase in relative excimer intensity is observed when proceeding from **DNO-2** to **DNO-3** ($I_E/I_M = 3.2$) and even further in case of **DNO-4** ($I_E/I_M = 10.3$). As shall be seen, this trend is due to increased flexibility of the linkers, thus permitting the pyrenyls to diffuse together during the excited state lifetime. Thus, for **DNO-4** an efficient excimer formation is observed in spite of the relatively weak interaction between the pyrenyls in the ground state.

It is important to distinguish between the peak-to-valley ratios obtained from absorption (P_A) and excitation spectra (P_M and P_E), respectively (see Table 5.1). While an absorption spectrum reflects the situation in the whole molecular population, an excitation spectrum only concerns the ground state molecules leading to the emission monitored.

For both **DNO-1** and **DNO-2**, P_M is greater than P_E, which means that the pyrenyls leading to monomer fluorescence are less associated than those forming excimers. In case of **DNO-3** and **DNO-4** the P_M values are smaller (2.3) and in level with the P_E values (2.2-2.4).

Therefore, the monomer and excimer fluorescence originate from excitation of the same conformational population. This is characterized by a relatively strong association between the pyrenyls since the P_M, and P_E values (2.3-2.4) are substantially smaller than the P_M = 3.4 value for the monomer **1**. However, the mutual orientation of the pyrenyls is not favourable for excimer formation. Following excitation, the relative intensities of excimer and monomer emissions from **DNO-3** and **DNO-4** are determined by the competitive processes of monomer radiative deactivation and conformational diffusion towards a pre-excimer geometry. As can be seen from the I_E/I_M ratios, the last process is most efficient in case of **DNO-4** thereby demonstrating a greater flexibility of the longer **DNO-4** linker in spite of the intermediate peptide bond.

The peak-to-valley ratio derived from the excimer excitation spectra vary insignificantly among the **DNO-1**, **DNO-3**, and **DNO-4** derivatives (P_E = 2.2-2.4). Only **DNO-2** stands out with a markedly smaller value (P_E = 1.7). As mentioned above, this result only concerns the molecules, which actually display excimer fluorescence, which is a minute fraction in case of **DNO-2**. These, on the other hand,

interact strongly already in the ground state. This finding elaborates the model derived above. There appears to be (at least) two ground state populations of **DNO-2** molecules which are *not* interconvertible on a timescale shorter than the lifetime of the excited singlet state. In the major population, the configuration is fixed very unfavourably for excimer formation and monomer fluorescence dominates. In a small fraction, strong pre-association and "pre-excimer" geometry leads to excimer formation and emission.

In the force field calculations, an angle of 10.0° was found between the long axis of the pyrenyl moieties of **DNO-1** while ca. 20° displacement was predicted for **DNO-2** (and **DNO-3/4)**. Since a co-axial configuration is considered the optimum geometry for excimer formation, [21;22] this result - in combination with the rigid framework - is consistent with the vastly more efficient excimer formation (I_E/I_M value, Table 5.1) found for **DNO-1** relative to **DNO-2**.

The time resolved measurements give further information. The fluorescence lifetime of the monomer **1** is 153 ns (Table 5.1). This is shortened by a factor of 50 or more in the molecules **DNO-1, DNO-3,** and **DNO-4** due to the competitive excimer formation. In case of **DNO-2** a much longer lifetime is observed in agreement with the model described above, since the majority of excited singlet pyrenyls are prohibited from deactivation by excimer formation.

In case of **DNO-3** and **DNO-4** a grow-in of the excimer fluorescence could be observed. As can be seen from Table 5.1, a good agreement is observed in each case between the excimer formation time (τ_F) and monomer singlet lifetime (τ_M). This means that excimer formation is the dominant deactivation path for the excited monomer, the rate being determined by conformational diffusion.

Interesting is the fact, that no grow-in could be observed in case of **DNO-1** and **DNO-2** in spite of the either very long (**DNO-2**) or still observable (**DNO-1)** monomer lifetimes. These observations are fully compatible with previous conclusions. A major population of **DNO-1** molecules holds a configuration with strong interaction among the pyrenyls and a mutual orientation optimal for excimer formation (pre-association). When excited, these molecules form excimers on a sub-ns time scale. A minor fraction of the **DNO-1** molecules is not perfectly in line with the excimer configuration and the excited pyrenyl lives long enough (τ_M = 2.1 ns) in order to fluoresce a little before it is deactivated by (mainly) excimer formation. The relative contribution from these molecules to the excimer emission intensity is too small in order to manifest itself in the on-set profile.

On the contrary, the majority of the **DNO-2** molecules are fixed in a configuration prohibitive for excimer formation and fluoresce as the monomer with long lifetime. A minute fraction is held in a strongly interacting, pre-excimer configuration which generate the excimer with sub-ns rate upon excitation.

When pyrene is used as a conformational probe, it is customary to distinguish between “dynamic excimers” and “static excimers”[11]. The first term refer to Birks’ original picture for excimer formation as a result of a diffusional encounter between individual monomers, one of them in the excited singlet state the other in the ground state. This process usually occurs on a nanosecond time-scale. When the excimer is formed by direct excitation of a ground state dimer, it is called “static” even though its formation should be observable with sub-ns resolution[11]. In the DNO-derivatives studied in this work, however, ground state interaction is observed to a varying degree as deduced from the absorption and excitation spectra of all four derivatives. But static excimer formation is only observed in case of **DNO-1** and to a small extent for

DNO-2. Some examples have been reported in the literature of strongly interacting pyrene moieties showing no excimer emission [23;27;28]. Oishi *et al.* [29] have reported on the photophysical properties of a peptide carrying two pyrene residues which formed a sandwich-type close pair in the ground state as evidenced by CD spectroscopy. Still, no excimer emission was observed. It is argued that formation of a strictly fixed sandwich type ground state dimer hinders the formation of an excimer [29]. These reports demonstrate that a strong interaction in the ground state, manifesting itself in absorption spectroscopy or circular dichroism does not necessarily imply efficient excimer emission.

The high affinity of the **DNO-1** and **DNO-2** derivatives to form ground state complexes and the restricted conformational freedom in the excited state are imposed onto the pyrene moieties by the DNO backbone. In contrast, the longer linkers of **DNO-3** and **DNO-4** are less rigid, thereby allowing for dynamic excimer formation from a less interacting pair of ground-state pyrenyls. Among these two, the **DNO-4** linker provides the greatest configurational freedom since excimer formation is efficient (high I_E/I_M) in spite of weak ground state interaction (high P_A). This conclusion is also evidenced by the relatively longer monomer fluorescence lifetime (τ_M), excimer formation time (τ_F) and excimer lifetime (τ_E) for **DNO-4** compared to **DNO-3**.

It has been observed that protic solvents, which are able to form hydrogen bonds, reduce excimer formation in pyrene labelled polypeptides [30]. Hydrogen bond forming solvents shift the equilibrium towards random coil conformation, which is unfavourable for excimer formation [30]. The extensive excimer formation of the **DNO-1**, **DNO-2** and **DNO-3** derivatives and the clear ground state association of the

DNO-2 derivative in methanol reveals that the DNO backbone is not particularly susceptible to random coiling even in protic solvents.

It has been reported that helical polypeptide chains are rigid enough to support side chain groups, including such large chromophores as pyrenyl groups, in specific spatial arrangement [15]. In agreement, the experimental results reported herein also point towards to the decisive role played by the specifically designed secondary helical structure of the DNO backbone. [4]

5.5 Conclusions

The pyrenyls of all of the doubly substituted DNO derivatives are associated to some extent in the ground state or are in the relative vicinity of each other when excited. This proximity is imposed on them by the DNO backbone. These results exclude the possibility of a random coiled configuration of the polypeptide. However, as deduced from the time resolved measurements, each derivative display individual dynamic properties, and ground state interaction occurs without necessarily leading to static excimer formation upon excitation:

1) For **DNO-1** the situation is relatively straightforward. In the major ground state population pre-association prevails, and “static” excimers are formed with great efficiency. In a minor ground state population, however, deactivation via the excimer occurs dynamically by configurational diffusion.
2) As to **DNO-2**, the major ground state configuration is strongly unfavourable for excimer formation. Apparently, the pyrenyls are sufficiently close to each other, but the molecular axis make an angle. The rigid backbone prevents reorientation and monomer emission dominates. However, in a minute fraction of the ground state molecules pre-association is tight and static excimer formation occurs.

5.6 Reference List

1) Voyer, N.In *Topics in Current Chemistry*; Springer Verlag: Berlin, 1996; pp 1-37.

2) Deming, T.J. *Adv.Mater.* **1997**, *9*, 299-311.

3) Tirrel, J.G.; Fournier, M.J.; Mason, T.L.; Tirell, D.A. *Chem.Engineer.News* **1994**, *December 19*, 40-51.

4) Berg, R.H.; Hvilsted, S.; Ramanujam, P.S. *Nature* **1996**, *383*, 505-508.

5) Rasmussen, P.H.; Ramanujam, P.S.; Hvilsted, S.; Berg, R.H. *Tetrahedron* **1999**, *40*, 5953-5956.

6) Rasmussen, P.H.; Ramanujam, P.S.; Hvilsted, S.; Berg, R.H. *J.Am.Chem.Soc.* **1999**, *121*, 4738-4743.

7) Egholm, M.; Nielsen, P.E.; Buchardt, O.; Berg, R.H. *J.Am.Chem.Soc.* **1992**, *114*, 9677-9678.

8) Egholm, M.; Buchardt, O.; Nielsen, P.E.; Berg, R.H. *J.Am.Chem.Soc.* **1992**, *114*, 1895-1897.

9) Nielsen, P.E.; Egholm, M.; Berg, R.H.; Buchardt, O. *Science* **1991**, *254*, 1497-1500.

10) Kleinman, M.H.; Bohne, C. *Molecular and Supramolecular Photochemistry*; Ramamurthy, V., Schanze, K.S., Eds.; Marcel Dekker, Inc.: New York, 1997; pp 391-466.

11) Winnik, F.M. *Chem.Rev.* **1993**, *93*, 587-614.

12) Parker, C.A.; Joyce, T.A. *Trans.Faraday Soc.* **1966**, *62*, 2785-2792.

13) Bright, F.V. *Appl.Spectrosc.* **1988**, *42*, 1531-1537.

14) De Schryver, F.C.; Boens, N.; Put, J. *Adv.Photochem.* **1977**, *10*, 359-463.

15) Sisido, M. *Prog.Polym.Sci.* **1992**, *17*, 699-764.

16) Merrifield, R.B. *J.Am.Chem.Soc.* **1963**, *85*, 2149-2154.

17) Merrifield, R.B. *Science* **1986**, *232*, 341-347.

18) HyperChem 4.0. Release 4 for WIndows Molecular Modelling Systems(4). 1994. Hypercube, Inc.

19) Dyke, D.A.V.; Pryor, B.A.; Smith, P.G.; Topp, M.R. *J.Chem.Edu.* **1998**, *75*, 615-620.

20) De Schryver, F.C.; Collart, P.; Vandendriessche, J.; Goedeweeck, R.; Swinnen, A.M.; Van Der Auweaer, M. *Acc.Chem.Res.* **1987**, *20*, 159-166.

21) Birks, J.B. *Rep.Prog.Phys.* **1975**, *38*, 903-974.

22) Schweitzer, D.; Colpa, J.P.; Behnke, J.; Hausser, K.H.; Haenel, M.; Staab, H.A. *Chem.Phys.* **1975**, *11*, 373-384.

23) Egusa, S.; Sisido, M.; Imanishi, Y. *Macromolecules* **1985**, *18*, 882-889.

24) Steinberg, I.Z. *Ann.Rev.Biophys.Bioeng.* **1978**, *7*, 113-137.

25) Richardson, F.S.; Riehl, J.P. *Chem.Rev.* **1977**, *77*, 773-792.

26) Egusa, S.; Sisido, M.; Imanishi, Y. *Chem.Lett.* **1983**, 1307-1310.

27) Inai, Y.; Sisido, M.; Imanishi, Y. *J.Phys.Chem.* **1990**, *94*, 2734-2735.

28) Inai, Y.; Sisido, M.; Imanishi, Y. *J.Phys.Chem.* **1990**, *94*, 8365-8370.

29) Oishi, O.; Yamashita, S.; Ohno, M.; Lee, S.; Sugihara, G.; Nishino, N. *Chem.Phys.Lett.* **1997**, *269*, 530-534.

30) Goedeweeck, R.; De Schryver, F.C. *Photochem.Photobi.* **1984**, *39*, 515-520.

Appendix I

The photostability of $TOTA^+$

I.1 Introduction

The photostability of a molecule intended for the study of photophysical properties or for use for more practical purposes such as commercial dyes is important. If a chromophore is degraded by light then it is usually not applicable for commercial exploitation. In the case of photophysical investigations, special steps have to be taken in order to obtain viable results, such as flow-through cells. The solvents used often play a paramount role in the stability of the chromophore. The solvent may react with the excited state of the chromophore or the solvent and the chromophore may form a ground state complex which is photolabile. Carbocations are unstable by intrinsic nature so special care has to be taken in order to investigate their stability.

In this chapter the photostability of $TOTA^+$ was investigated in three solvents: water, methanol and acetonitrile. An excimer laser and a high pressure xenon lamp were used as light sources. Absorption and NMR spectroscopies were employed in order to monitor the effects of irradiation and the solvent. The results are compared to theoretical calculations on the *semi – empirical* level.

I.2 Experimental and Calculations

The ^{1}H-NMR spectra were recorded on a Varian Mercury 300 MHz spectrometer using tetramethylsilane (TMS) as internal standard. The deuterated solvents were used as received.

The program HyperChem 4.0 was used to geometry optimise the structure and generate the oscillator strengths. The first guess for optimised geometry was achieved with the MM+ force field package and then further refined with the PM3 *semi-empirical* method. The oscillator strengths were calculated utilising the ZINDO/S *semi-empirical* package. One electron excitation with 10 highest occupied and 10 lowest unoccupied configuration interactions singles (CI singles) was used.

A Lambda Physik EMG102 xenon-chloride laser was used to irradiate the samples with excitation wavelength at λ = 308 nm. The laser pulse had the duration of ca. 10 ns and the energy output of approximately 0.8 J/pulse. The solutions had absorption of A = 0.5 at 308 nm.

A standard high pressure xenon lamp was used in order to irradiate the solutions of $TOTA^{+}$ ($\sim 5\times10^{-5}$ M).

The optical density of the solutions was monitored on a Hewlett Packard 8453 absorption spectrometer.

I.3 Results and Discussion

The ground state interaction of $TOTA^+$ and solvents was investigated by means of ^{1}H-NMR spectroscopy. Spectra were recorded in four deuterated solvents, being methanol-d_4, ethanol-d_6, D_2O and acetonitrile-d_3.´ Two peaks with triplet and doublet multiplicities attributed to $TOTA^+$ appeard in water and acetonitrile with chemical shifts at $\delta = 8.4$ and $\delta = 7.8$ ppm, respectively. The spin coupling of the peaks are $J = 0.03$ ppm. The triplet is assigned to the *para* - hydrogen (atom 8, figure I.5) and the doublet to the *ortho* – hydrogen atoms (atoms 7, figure I.5). Integration reveals a 2:1 ratio of the peaks and confirms the assignment to the respective hydrogen atoms. In the case for the deuterated alcohol solvents, two sets of doublets and triplets appear as depicted in figure I.1 for methanol. The more intense set of peaks has the same chemical shift as the ones observed in acetonitrile and D_2O, verifying the presence of $TOTA^+$ in the solution.

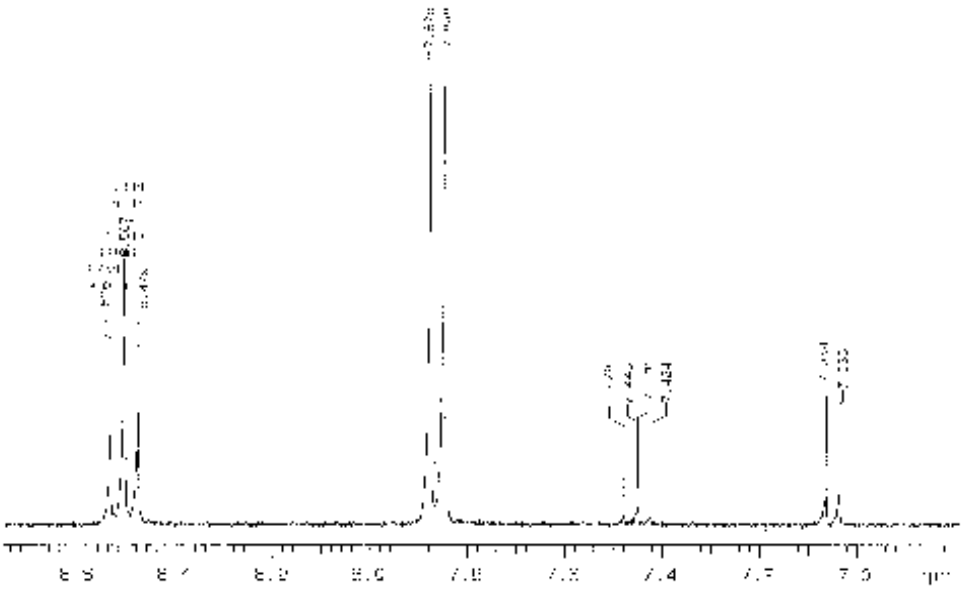

Figure I.1. The ^{1}H-NMR spectrum of the $TOTA^+$ carbocation in deuterated methanol. Two sets of triplets and doublets appear verifying ground state interaction between $TOTA^+$ and methanol.

The new set of peaks is shifted upfield relative to their counterparts by 1.1 ppm for the triplet and 0.8 ppm for the doublet. This increased shielding of the protons indicates a higher electron density of the new species. The new species retains the same peak configuration and same spin coupling. With this evidence at hand it is safe to conclude that a nucleophilic attack takes place at the centre carbon atom (atom 1, figure I.5) as shown in figure I.2.

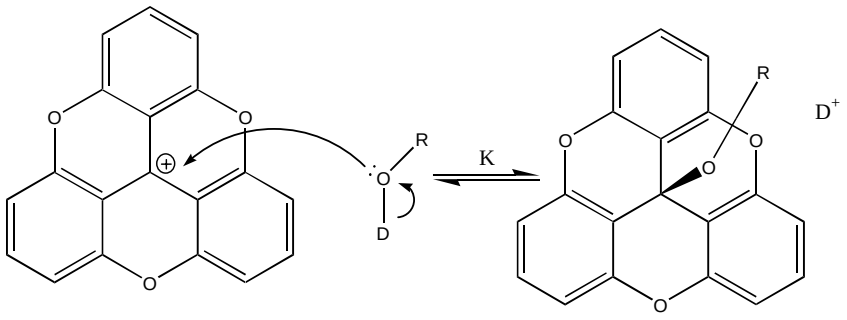

Figure I.2. Nucleiophilic attack of the lone pair on the alcohol solvent on the centre carbon atom of the $TOTA^+$ carbocation (atom 1, figure I.5).

The reaction is depicted as reversible; it is very likely that the proton produced is able to reclaim its electron via an electrophilic attack on the ether oxygen of the new species (ether – $TOTA^+$). The ratio of the peak sets was determined as 2:1 of $TOTA^+$ versus its ether derivative in ethanol and 12:1 for methanol. The concentration of the deuterated solvents are 17.04 M for ethanol and 24.68 M for methanol. With the initial concentration known and the integrals from the ^{1}H-NMR spectra it is possible to calculate the equilibrium constant K:

$$K = \frac{\left[D^+\right]\left[TOTA - OR\right]}{\left[TOTA^+\right]\left[R - OD\right]}$$

The concentration of D^+ and TOTA-OR is the same simplifying the calculations. The determined equilibrium constants are $K = 1.06\times10^{-5}$ for ethanol and $K = 1.38\times10^{-6}$ for methanol. The ion pair association constant (K_A) is 18 for methanol and 133 for ethanol (Isaacs, N. *Physical Organic Chemistry*; Second Edition; Longman Scientific & Technical: Essex, 1994; pp 272). This constant reflects the nucleophilic nature of the alcohols. This difference of the K_A constants explains the higher concentration of the ether derivative in ethanol.

The structure of the new species was investigated with force field and *semi – empirical* methods. Geometry optimisation reveals an inverted umbrella shaped structure as depicted in figure I.3 for the methyl ether derivative.

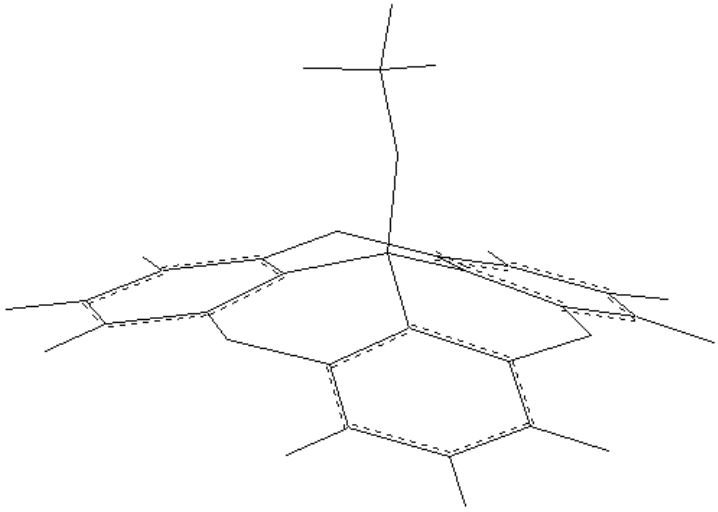

Figure I.3. The structure of the methyl – ether - $TOTA^+$ optimised with the PM3 *semi – empirical* method.

The *semi – empirical* ZINDO/S method was used to generate the electronic absorption transitions of the ether $TOTA^+$ from the optimised structure. Two transitions were predicted above 200 nm, the first at 205.8 nm with oscillator strength of 1.70 and the

second at 222.2 nm with oscillator strength of 0.24. In summary, ether $TOTA^+$ does have significant absorption just above 200 nm according to this theoretical model.

The photostability of $TOTA^+$ was investigated in methanol, water and acetonitrile. Solutions were irradiated at λ = 308 nm with an excimer laser (2.1 μeinstein/pulse). After 100 pulses the absorption at 450 nm had decreased by 0.5 % for the acetonitrile solution, 1.5 % for the water solution and 2.5 % for the methanol solution, which makes $TOTA^+$ photostable for all practical purposes. When a solution of $TOTA^+$ was exposed to the irradiation of an unfiltered high pressure Xe – lamp, rapid photodegradation was observed for the methanol solution as depicted in figure I.4. The Xe-lamp emits a broad spectrum of light, including the region between 200 – 250 nm where the ether – $TOTA^+$ derivative absorbs. It is therefore reasonable to conclude that the ether – $TOTA^+$ derivative is not photostable and when degraded, the equilibrium shown in figure I.2 shifts to the right and gradually all of the $TOTA^+$ in an alcohol solution is consumed.

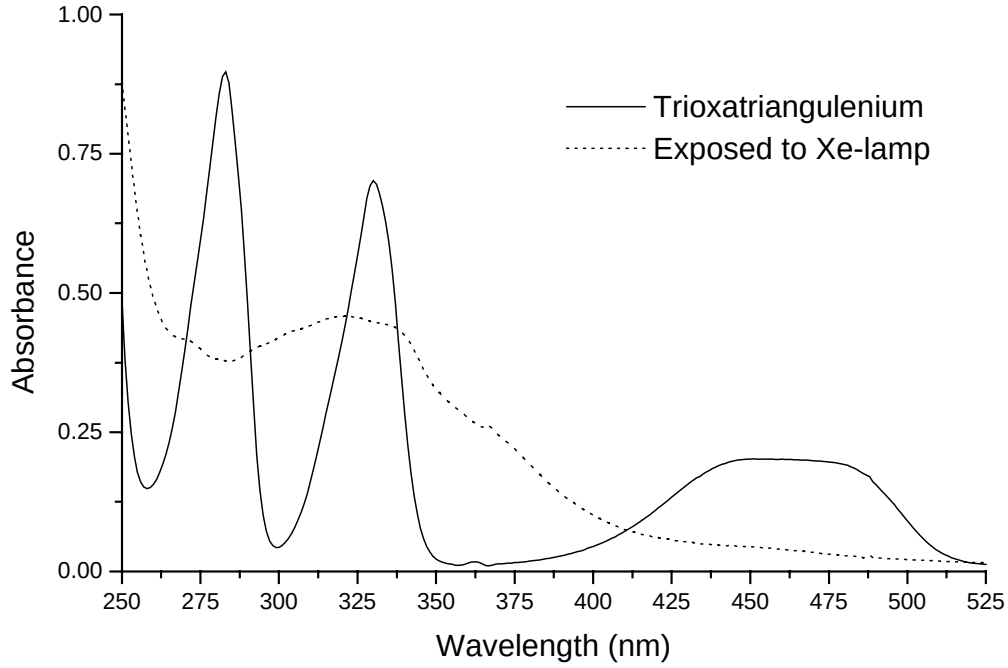

Figure I.4. Absorption spectra of $TOTA^+$ in methanol before and after exposure to unfiltered Xe-lamp irradiation. Photodegradation is clearly observed for $TOTA^+$.

Further support of the photostability of $TOTA^+$ in methanol can be gleaned from its fluorescence lifetime. It is τ_{fl} = 11.9 ns, only ~20% lower than in acetonitrile (τ_{fl} = 14.6 ns) and practically the same as in water (τ_{fl} = 11.7 ns, see table 3.2). It can be speculated that the positive charge is even more delocalised in the singlet exited state of $TOTA^+$, making it more resistant to nucleophilic attack than its ground state even though the overall electrophilicity is increased for the excited species. This conjecture was investigated qualitatively by means of computational method. As before the PM3 *semi – empirical* package was used, which can predict the charge distribution in the ground (S_0) and the singlet excited (S_1) states. The charge distribution is shown in table I.1 and the corresponding atoms are depicted in figure I.5. The values are normalised with the charge on the atom number 8. It is apparent the positive charge density is dramatically decreased for the singlet excited state on the centre atom (atom 1) where the nucleophilic attack is thought to take place. These theoretical results elucidate the similarity of the fluorescence lifetimes.

Table I.1. The charges on the atoms of $TOTA^+$ predicted for the ground (S_0) and singlet excited state (S_1). The PM3 *semi-empirical* method was utilised. The values are normalised with respect to the charge on atom 8.

atoms	S_0	S_1
1	2.07	-0.81
2	-1.80	-0.18
3	1.36	0.67
4	-0.42	-0.34
5	-1.19	-0.92
6	0.43	-0.56
7	1.19	1.13
8	1.00	1.00

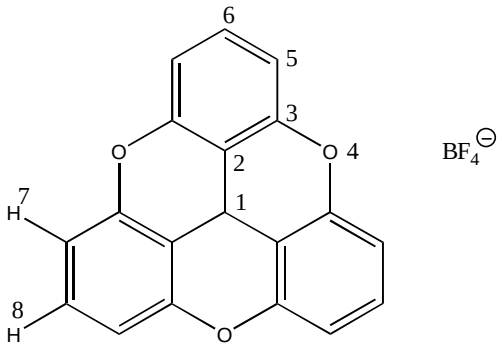

Figure I.5. Trioxatriangulenium and its counter ion. Numbering of atoms of the $TOTA^+$ carbocation.

Appendix II

Resonance Raman spectra of $TOTA^+$

II.1 Introduction

The resonance Raman spectra of $TOTA^+$ were measured at four wavelengths depicted in figure II.1.

It was not possible to acquire spectra from the two lowest lying absorption bands due to high fluorescence intensity in that region.

Unfortunately there was no time to make the necessary quantum mechanical calculations to interpret these spectra, which would have given information on the charge distribution of the excited states of $TOTA^+$.

The resonance Raman spectra are shown in figures II.2. to II.5.

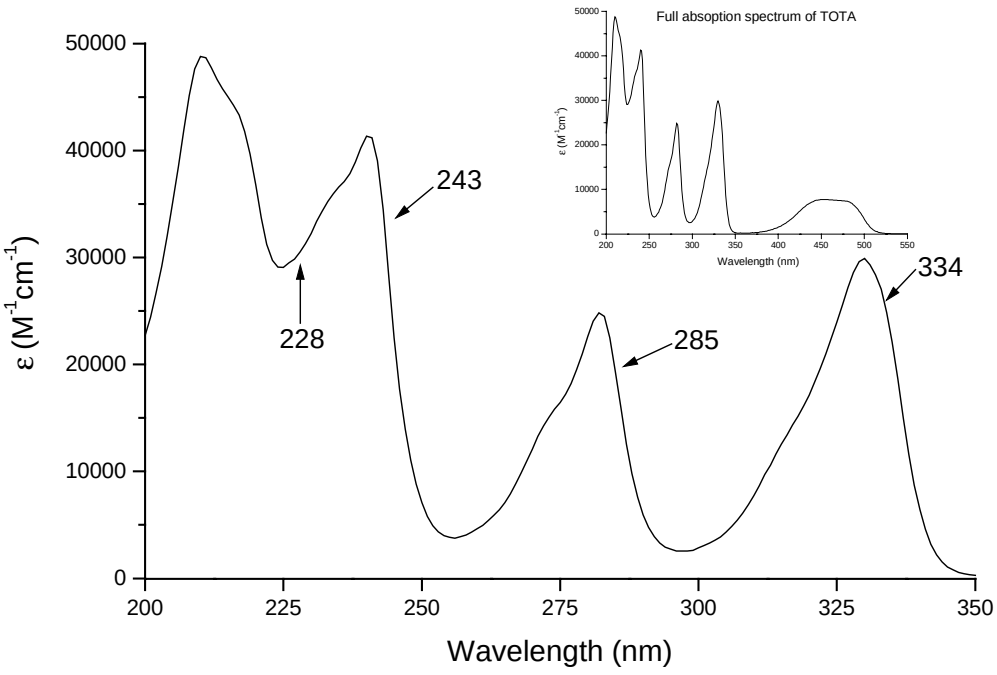

Figure II.1. The excitation wavelengths used for Raman scattering. The inset depicts the complete absorption spectrum of $TOTA^+$ in water.

II.2 Experimental

Resonance Raman spectra from a concentrated solution of $TOTA^+$ in water (triply distilled) (~1 mM) were recorded with pulsed excitation from an optical parametric oscillator (Continuum, Sunlite, OPO), 1.5 mJ at 228 nm, 5 mJ at 243 nm, 2mJ at 285 nm and 3 mJ at 334 nm. The OPO was pumped with a Nd-YAG laser at 355 nm (Continuum, Powerlite, PL9010). The detector employed was a liquid nitrogen cooled CCD (Charged Coupled Device) (Princeton Instruments, Inc. LN/CCD-1100-PB/VISAR/1). Triple monochromators with a grating of 1200 grooves/mm, Jobin Yvon T64000) were utilized to analyze the scattered light. Spinning optical cells made out of quartz were employed. Cyclohexane was used to calibrate the monochromators. The dimensions of the cells were 3.0 cm in diameter and 1.3 cm in height.

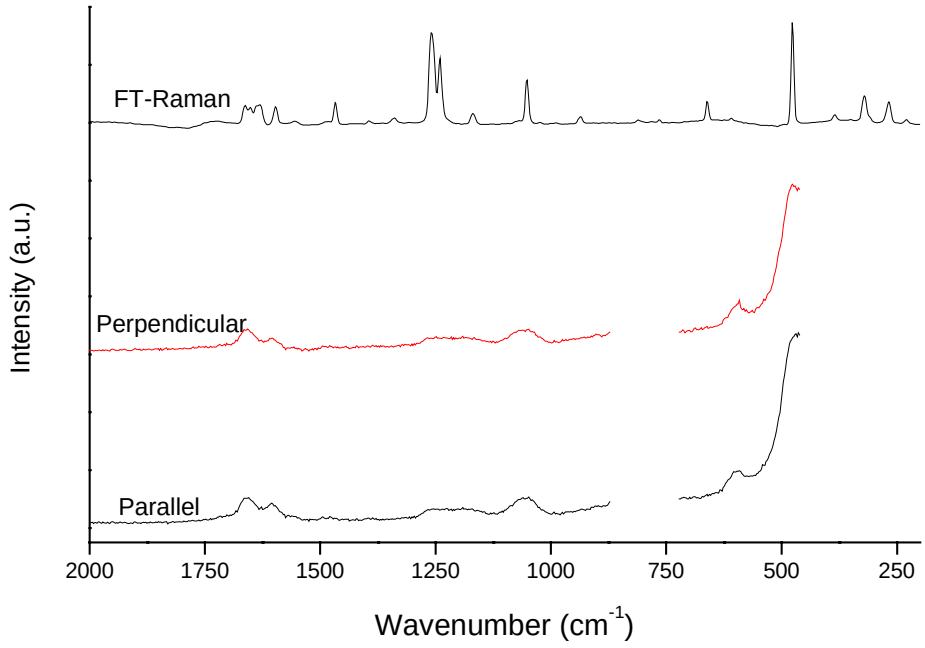

Figure II.2. Resonance Raman spectrum of $TOTA^+$ acquired at λ_{exc} = 228 nm.

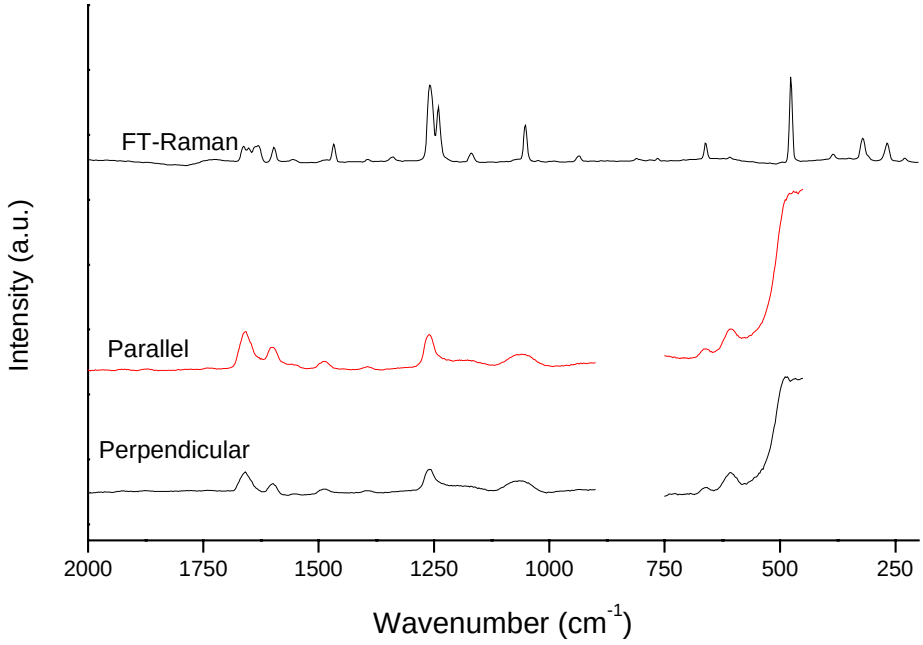

Figure II.3. Resonance Raman spectrum of $TOTA^+$ acquired at λ_{exc} = 243 nm.

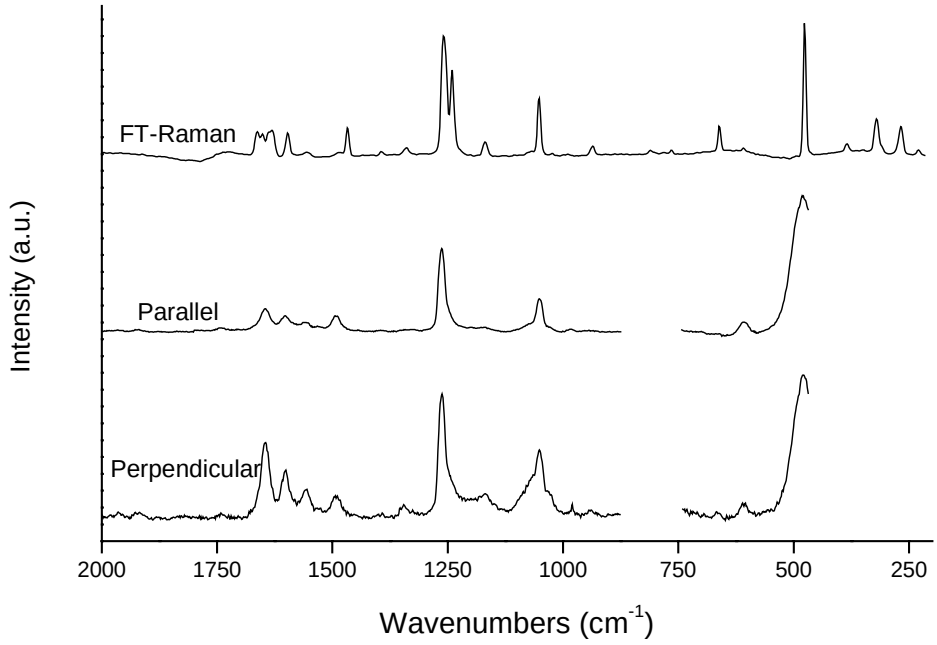

Figure II.4. Resonance Raman spectrum of $TOTA^+$ acquired at λ_{exc} = 285 nm.

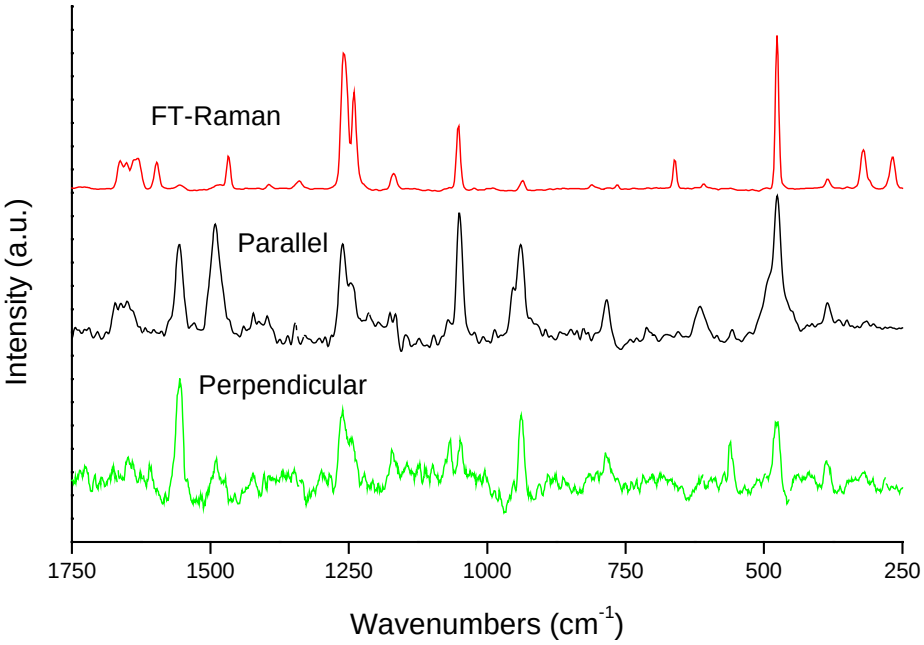

Figure II.5. Resonance Raman spectrum of $TOTA^{+}$ acquired at λ_{exc} = 334 nm.